

**Modeling and Design Optimization of Electromechanical Brake Actuator Using
Eddy Currents**

by

Kerem Karakoc

MASc, University of Victoria, 2007

BSc, Bogazici University, 2005

A Dissertation Submitted in Partial Fulfillment
of the Requirements for the Degree of

DOCTOR OF PHILOSOPHY

in the Department of Mechanical Engineering.

©Kerem Karakoc, 2012

University of Victoria

All rights reserved. This dissertation may not be reproduced in whole or in part, by
photocopy or other means, without the permission of the author.

**Modeling and Design Optimization of Electromechanical Brake Actuator Using
Eddy Currents**

by

Kerem Karakoc
MAsc, University of Victoria, 2007
BSc, Bogazici University, 2005

Supervisory Committee

Dr. Afzal Suleman, Dept. of Mechanical Engineering, University of Victoria
Co-Supervisor

Dr. Edward Park, Dept. of Mechanical Engineering, University of Victoria
Co-Supervisor

Dr. Ned Djilali, Dept. of Mechanical Engineering, University of Victoria
Departmental Member

Dr. Issa Traore, Dept. of Electrical and Computer Engineering, University of Victoria
Outside Member

Supervisory Committee

Dr. Afzal Suleman, Dept. of Mechanical Engineering, University of Victoria

Co-Supervisor

Dr. Edward Park, Dept. of Mechanical Engineering, University of Victoria

Co-Supervisor

Dr. Ned Djilali, Dept. of Mechanical Engineering, University of Victoria

Departmental Member

Dr. Issa Traore, Dept. of Electrical and Computer Engineering, University of Victoria

Outside Member

Abstract

A novel electromechanical brake (EMB) based on the eddy current principle is proposed for application in electrical vehicles. The proposed solution is a feasible replacement for the current conventional hydraulic brake (CHB) systems. Unlike CHBs, eddy current brakes (ECBs) use eddy currents and their interaction with an externally applied magnetic field to generate braking torque. Due to their pure electrically controllable and contact free nature, ECBs have multiple advantages over the current CHB systems, such as faster response, reduced weight and number of components, ease of implementing various controllers (e.g., anti-lock braking), and reduced noise levels. However, the torque generated by a typical ECB at low speeds is insufficient to effectively and completely stop a moving vehicle. Therefore, an ECB is commonly used as an assistive brake to the CHB system in heavy vehicles, i.e. trains and trucks.

In order to overcome this shortcoming, the use of AC magnetic fields is proposed to realize a stand-alone ECB system in which sufficient braking torque can be generated at low speeds. To this end, eddy currents are modeled analytically using the governing Maxwell's equations with the consideration of time varying field application. The analytical model was validated using finite element analysis. Results show that the braking torque increases with the application of a time varying field.

Various forms of time varying fields have been studied. It was found that the frequency-modulated applied field in triangular waveform results in the highest braking torque. Next, the design was optimized to maximize the braking torque and an optimum configuration was obtained using multiple pole projection areas (PPAs). Optimization results show that the braking torque significantly increases with the introduction of

additional PPAs to the configuration, and the braking torque generation for an optimum four-PPA ECB configuration exceeds the braking requirements for current passenger vehicles.

For control purposes, a dynamic model for a novel stand-alone ECB system using AC fields for automotive applications has been successfully designed and evaluated. Also, a model-based predictive controller has been developed for the optimum ECB configuration. Finally an experimental test-bed has been designed for experimentation of both DC and AC field application on ECB.

Keywords:

- *Brake-by-wire*
- *Eddy Current Brake*
- *Time-varying Magnetic Fields*
- *Analytical Modeling*
- *Helmholtz Equations*
- *Method of Images*
- *Finite Element Modeling*
- *Genetic Algorithm*
- *Vibration Response of Human Body*
- *Automotive Applications*
- *Model Based Predictive Control*

Table of Contents

Supervisory Committee	ii
Abstract	iii
Table of Contents	v
List of Tables	vii
List of Figures	viii
Nomenclature	x
Acknowledgments	xiii
Dedication	xiv
1. INTRODUCTION	1
1.1 Overview	1
1.2 Objectives and contributions	9
1.2.1 Contributions	10
1.3 Thesis Outline	11
2. ANALYTICAL MODELING OF EDDY CURRENT BRAKES WITH THE APPLICATION OF TIME VARYING MAGNETIC FIELDS	13
2.1 Introduction	13
2.2 Analytical modeling of eddy currents	14
2.3 Validation and preliminary results	27
2.4 Discussion	32
2.5 Conclusion	35
Appendix.2A. Analytical Model: DC field application	35
3. IMPROVED BRAKING TORQUE GENERATION CAPACITY OF EDDY CURRENT BRAKE WITH TIME VARYING FIELDS: A NUMERICAL STUDY	44
3.1 Introduction	44
3.2 Eddy current brake model	45
3.3 Simulation results	50
3.3.1 Validation of the FEM	51
3.3.2 Time varying field application with induction effects	54
3.3.3 ECB configuration for automotive application	57
3.3.4 Time varying field application and optimization without induction effects ..	58
3.3.5 Effects of frequency modulation on braking torque generation	60
3.4 Discussion	62
3.5 Conclusion	67
Appendix.3A. Analytical Model: DC field application	67
4. OPTIMIZATION OF BRAKING TORQUE GENERATION CAPACITY OF EDDY CURRENT BRAKES WITH THE APPLICATION OF TIME VARYING MAGNETIC FIELDS	69
4.1 Introduction	69
4.2 Eddy current brake model	70
4.3 Optimization	74
4.4.1 Definition of the problem	74
4.4.2 Optimization Results	80

4.4	Discussions	82
4.5	Conclusion	86
5.	CONTROL.....	87
5.1	Introduction.....	87
5.2	Dynamic ECB Model.....	89
5.3	Dynamic model of the vehicle	93
5.4	Design of a model based nonlinear predictive controller	94
5.3.1	<i>Nonlinear model predictive control algorithm</i>	94
5.3.2	<i>NMPC applied to ECB problem</i>	98
5.5	Simulation results.....	101
5.6	Conclusion	105
6.	EXPERIMENTAL STUDIES	106
6.1	Introduction.....	106
6.2	Experimental setup.....	107
6.3	DC field application.....	109
6.4	AC field application.....	113
6.5	Summary.....	116
7.	CONCLUSIONS AND FUTURE WORK.....	118
7.1	Conclusions.....	118
7.1.1	<i>Summary of Chapter 2</i>	119
7.1.2	<i>Summary of Chapter 3</i>	119
7.1.3	<i>Summary of Chapter 4</i>	120
7.1.4	<i>Summary of Chapter 5</i>	120
7.1.5	<i>Summary of Chapter 6</i>	121
7.2	Future works	121
7.3	Recommendations.....	124
	Bibliography	125
	Appendix.....	132
	Appendix A. Vehicle dynamics	132
	Appendix B. Braking torque requirements	136
	Appendix C. Ferrite material properties and core specs for AC field experiments [74]	138

List of Tables

Table 1-1. Advantages and disadvantages of a CHB and an EMB	4
Table 2-1. Specifications of the ECB configuration	29
Table 3-1. Specifications of the configuration adapted from [29].....	51
Table 3-2. Selected ECB configuration for automotive applications	58
Table 4-1. Design Variables and Constants for the ECB optimization problem	75
Table 4-2. Optimum ECB Configurations	80
Table 4-3. Optimum braking torque values for cases studied	81
Table 5-1. Specifications of the vehicle and road conditions	100
Table 6-1. Experimental setup specifications	110
Table 6-2. Specifications of the optimum one PPA configuration from Table 4-3	115
Table A-1. Parameters for the quarter vehicle model	136
Table A-2. Required braking torque values for several vehicles.....	137

List of Figures

Figure 1-1. Schematic of a CHB on a passenger vehicle [1]	1
Figure 1-2. Comparison of a CHB system and an electromechanical brake (EMB) system on a passenger type vehicle [2]	3
Figure 1-3. Eddy current brake (ECB) concept	6
Figure 2-1. Basic ECB domain considered for simulating the eddy current generation ..	16
Figure 2-2. PPA moving in externally applied field.	22
Figure 2-3. Method of images, a) electric charge, b) magnetic dipole	25
Figure 2-4. Flowchart of the FEM implementation	28
Figure 2-5. Convergence plot	30
Figure 2-6. Variation in braking torque with frequency of the externally applied magnetic flux density.....	31
Figure 2-7. Variation in braking torque with angular velocity of the rotating brake disk	32
Figure 2-8. Comparison between braking torques generated with AC and DC field applications	34
Figure 3-1. Basic ECB domain considered for simulating the eddy current generation ..	46
Figure 3-2. Flowchart of the proposed FEM implementation	50
Figure 3-3. Comparison between analytical and FEM results for DC field analysis	52
Figure 3-4. Braking torque versus frequency at 50 rpm	53
Figure 3-5. Braking torque versus rotational velocity at 10 Hz.....	54
Figure 3-6. Braking torque generation – (a) sinusoidal, (b) square wave, (c) sawtooth wave, and (d) triangular wave field applications.....	55
Figure 3-7. Braking torque variation with increasing frequency at 50 rpm with induction effects	56
Figure 3-8. Braking torque variation with increasing frequency at 50 rpm without induction effects.....	57
Figure 3-9. Braking torque generation at 10 Hz for triangular, sinusoidal and DC field applications	59
Figure 3-10. Optimum braking torque generation with frequency modulation.....	62
Figure 3-11. Conductor brake disk with an array of PPAs	66
Figure 4-1. Basic ECB domain considered for simulating the eddy current generation ..	71
Figure 4-2. Flowchart of the FEM implementation	73
Figure 4-3. Flowchart of the optimization procedure	79
Figure 4-4. Optimum 4-PPA configuration	81
Figure 4-5. Braking torque generation at various angular velocities.....	83
Figure 4-6. Deceleration curve	84
Figure 5-1. Comparison between the estimated model and the FEM results	93
Figure 5-2. Nonlinear model predictive control block diagram	95
Figure 5-3. NMPC Flowchart (MV - manipulated variables, DV - disturbance variables and CV - controlled variables).....	98
Figure 5-4. ECB performance with NMPC	103
Figure 6-1. Experimental setup.....	108
Figure 6-2. Eddy current brake (ECB) prototype with permanent magnets	110

Figure 6-3. Comparison between the FE simulation and experimental results for the prototyped configuration.....	111
Figure 6-4. Flux density distribution between two permanent magnets.....	112
Figure 6-5. AC electromagnet core configuration	114
Figure 6-6. Selected ECB configuration for experimentations.....	116
Figure 7-1. Quarter vehicle shaker for testing real world performance of ECB (equipment is available at SFU, BC).....	122
Figure A-1. Free body diagram of a wheel	133
Figure A-2. Friction coefficient versus slip ratio for several surfaces [76]	135

Nomenclature

a	Width of the PPA (m)
$A_x^{(i)}$	x component of imaginary magnetic potential term (V s / m)
$A_y^{(i)}$	y component of imaginary magnetic potential term (V s / m)
$A_x^{(p)}$	x component of primary magnetic potential term (V s / m)
$A_y^{(p)}$	y component of primary magnetic potential term (V s / m)
$A_{x,net}$	x component of net magnetic potential (V s / m)
$A_{y,net}$	y component of net magnetic potential (V s / m)
$\mathbf{A} (A_x, A_y)$	Magnetic vector potential (V s / m)
b	Height of the PPA (m)
\mathbf{B}	Magnetic flux density vector (T)
\mathbf{B}_0	Externally applied magnetic flux density (T)
\mathbf{B}_{in}	Induced magnetic flux density (T)
c, c_1, c_2	Coefficients that are used to estimate the dynamic ECB model
C	Coefficient function
d	Thickness of the conductive disk (m)
d_{skin}	Skin depth (m)
d_{eff}	Effective thickness of the conductive disk (m)
\mathbf{D}	Displacement flux density (C / m ²)
E_{xDC}	x component of electric field with DC field application (V / m)
E_{yDC}	y component of electric field with DC field application (V / m)
\mathbf{E}	Electric field (V / m)
f_l	Carrier frequency (Hz)
f_2	Modulation frequency (Hz)
Δf	Frequency deviation (Hz)
f_0	Basic coefficient
f_s	Spaced effect coefficient
\mathbf{F}	Coulomb's force (N)
G	Green's function to solve Helmholtz equation
G_f	Geometric Function
h_{cg}	Height of the center of gravity (kg)
H	Magnetic field intensity (A/m)
I_t	Total moment of inertia of the wheel and the engine (kgm ²)
$\mathbf{J} (J_x, J_y)$	Current density vector (A / m ²)
\mathbf{J}^s	Surface current density vector (A / m)
\mathbf{J}_{in}	Induced current density vector (A)

K_v	Scaling constant
l_{base}	Wheel base (m)
m_w	Wheel mass (kg)
m_v	Vehicle mass (kg)
p_n, q_m	Geometric identifiers for green's function ($n, m=1, 2, 3, \dots$)
q	Charge (C)
R	Radius of the conductive disk (m)
r	Distance between the center of conductive disk and the center of the PPA (m)
$\mathbf{r_p}$	Position vector from the center of the disk (m)
R_w	Wheel radius (m)
s_r	Slip ratio
dS	Infinitesimal surface (m^2)
t	Time (s)
T_b	Braking torque without induction fields (Nm)
T_{bin}	Braking torque with induction effects included (Nm)
T_{time}	Time dependent function
$T_{b,n}$	Braking torque generated at the nth PPA
$T_{b,total}$	Total braking torque generated
\mathbf{v}	Linear velocity vector (m / s)
w	Rotational velocity of the conductive disk (rad/s)
$x^{(i)}$	x coordinate of imaginary magnetic potential source (m)
$y^{(i)}$	y coordinate of imaginary magnetic potential source (m)
ϕ	Electric Scalar potential (V)
ϵ	Electric permittivity (F / m)
μ	Magnetic permeability (H / m)
ρ	Charge density (C / m^3)
ρ_{res}	Resistivity of the material (ohm m)
σ	Conductivity of the material (S / m)
λ	Wave term
$\Phi (\phi_x, \phi_y)$	Source term
Ω	Angular frequency of the applied field (rad / s)
β_n	Phase angles between applied fields at each PPA ($n=1, 2, 3, \dots$) (rad)
α_n	Angles between PPAs on a multi PPA config. ($n=1, 2, 3, \dots$) (rad)

Acronyms

CHB	Conventional Hydraulic Brake
ECB	Eddy Current Brake
EC	Eddy Currents

EMB	Electromechanical Brake
MRB	Magnetorheological Brake
MRF	Magnetorheological Fluid
SR	Switch Reluctance
ABS	Anti-lock Braking System
AC	Alternating Current
DC	Direct Current
PPA	Pole Projection Area
FE	Finite Element
FEM	Finite Element Method
PDE	Partial Differential Equation
UMFPACK	Unsymmetric MultiFront Method
MPC	Model Predictive Control
RMS	Root Mean Square
GA	Genetic Algorithm
S-FEM	Smoothed Finite Element Method
rpm	Rotation per Minute

Acknowledgments

I would like to thank to Dr. Edward J Park and Dr. Afzal Suleman for giving me the chance to work on this project and also for their support, guidance, encouragement and patience.

Special thanks to Sandra Makosinski who is the kindest person I have ever known. Thanks for everything you have done for me and for all of us. I cannot tell you how lucky we are to know you.

Special appreciation to Art Makosinski, Barry Kent, Rodney Katz, Patrick Chang, Dorothy Burrows and all faculty from Department of Mechanical Engineering in University of Victoria. It is great to be a part of such an incredible group.

I also would like to thank my friends and colleagues, Baris Ulutas, Casey Keulen, Bruno Rocha, Joana Rocha, Andre Carvalho, Ricardo Paiva, Adel Younis, Kel Sakaki, Dan Kerley, Jung Keun Lee and many more for their friendship, support and kindness. It is not only valuable experience and knowledge but I also gained life-long friends during my graduate studies.

I would like to thank my family. There is no word to describe how grateful I am to have you. My mother and father, Emine and Hasan Karakoc, although you were not here with me, thanks for helping me be who I am today. Thank to Dr. Emre Karakoc, my brother, for always watching my back. And I would like to thank to my best friend and wife, Asia Karakoc, for her endless support, encouragements, love and friendship. You made this easier for me by just being a part of my life.

To all of you, *thank you!*

Dedication

Dedicated to my best friend and wife, *Dr. Asia Karakoc*.

1. INTRODUCTION

1.1 Overview

Automotive industry is a dynamic and challenging field and considerable technological innovations are proposed every year. Considerable resources are invested in research and development for building safer, cheaper and better performing vehicles. In particular, technological innovations such as "x by wire" solutions used to improve the existing mechanical systems have contributed significantly to make automobile more environmentally sustainable. For example, "brake by wire" means that the mechanical systems in the vehicles can be replaced by electromechanical systems that are able to do the same task in a faster, more reliable and more accurate way when compared to the pure mechanical systems.

More specifically, conventional hydraulic brakes (CHB) are currently being used in order to provide the required braking torque to stop a vehicle. This system involves a pedal, hydraulic fluid, transfer pipes and the brake actuator. When the driver pushes the brake pedal, the hydraulic brake fluid provides the pressure that squeezes the pads onto the rotor. The basic block diagram of this type of brake is shown in Figure 1-1.

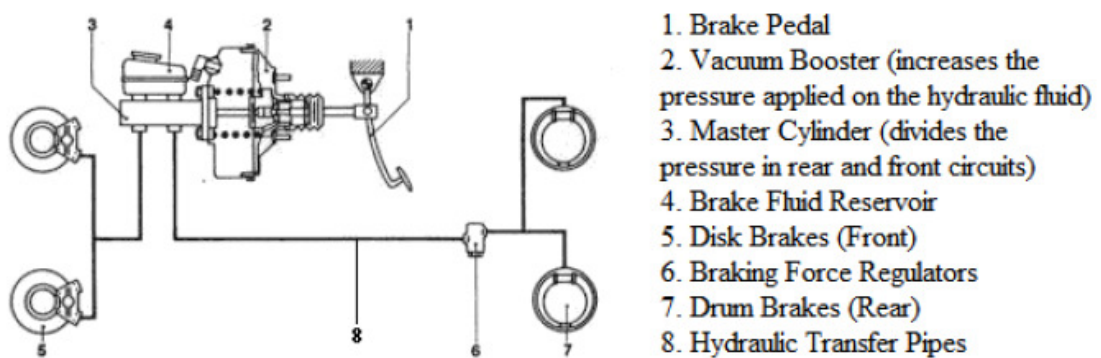


Figure 1-1. Schematic of a CHB on a passenger vehicle [1]

However, CHBs have a number of disadvantages. First of all, when the driver pushes the pedal, there is latency in building up the pressure necessary to actuate the brakes. Also, since CHBs employ a highly pressurized brake fluid, there may be leakage of the brake fluid that could cause fatal accidents. Furthermore, the fluid is harmful to the environment.

CHBs employ friction between brake pads and the brake disk. Therefore, brake pad material wear occurs. Due to both the material wear and the friction coefficient change in high speeds, the brake performs less optimally in high-speed regions as well as after a number of actuations. Thus, the brake pads must be changed periodically in order to get the optimum braking performance. Finally, ECB mechanisms are bulky in size, considering both auxiliary components and brake actuators.

In some applications such as trucks and heavy machinery that need more braking torque, in addition to the use of CHB, drum brakes actuated by pneumatic systems are being used instead of hydraulic systems. Similar to CHBs, these types of brakes employ friction generated between two contact surfaces.

In brake-by-wire, some of the pure mechanical components of the conventional hydraulic brakes (CHBs) are replaced by electromechanical components. Such an electromechanical system will result in a number of advantages, such as faster braking response time, easy implementation of various control systems and reduced number of components and wiring. Figure 1-2 (left) shows a typical EMB system with reduced number of components compared to the CHB system (on the right). In Table 1-1, the disadvantages of a CHB and the potential advantages of an electromechanical brake (EMB) are listed.

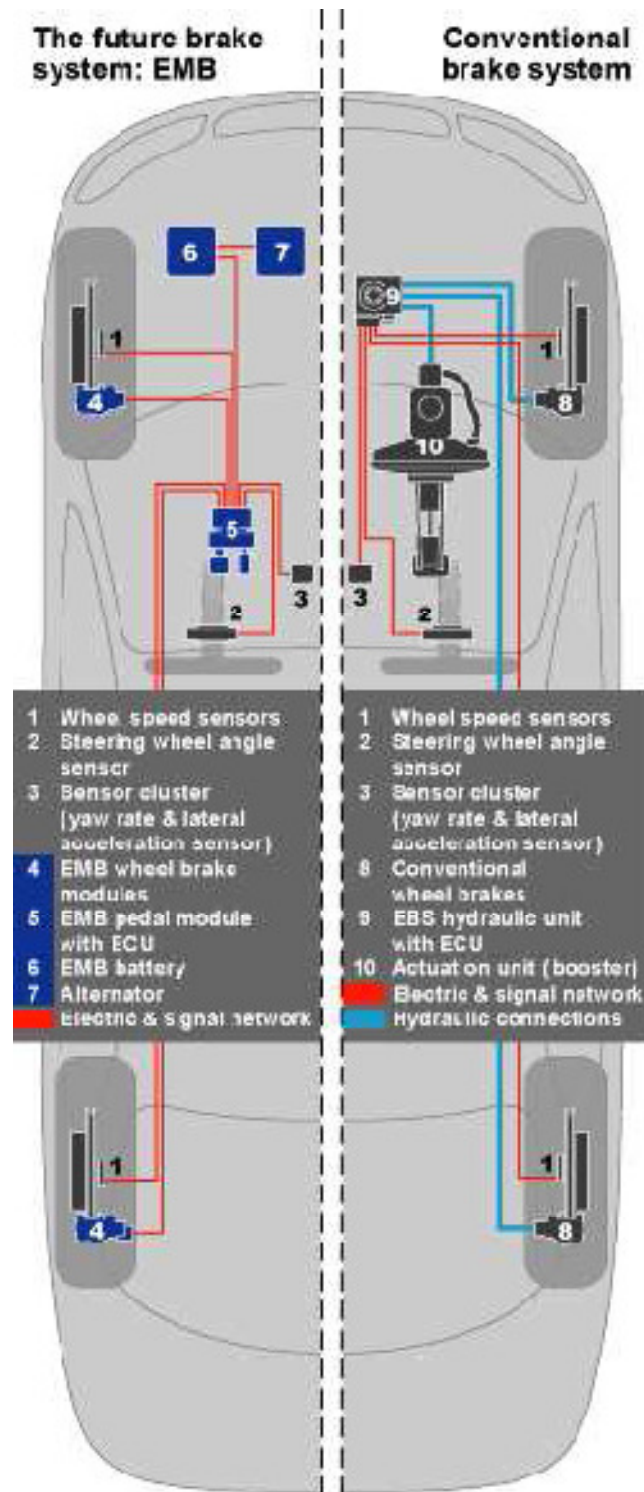


Figure 1-2. Comparison of a CHB system and an electromechanical brake (EMB) system on a passenger type vehicle [2]

Table 1-1. Advantages and disadvantages of a CHB and an EMB

CHBS	EMB
<p><u>Advantages:</u></p> <ul style="list-style-type: none"> • High braking torque generation • Available controllers • Accepted technology with significant background <p><u>Disadvantages:</u></p> <ul style="list-style-type: none"> • Slow response due to pressure build-up • Control requires additional electrical components • Significant weight of the overall system • Brake pad wear • Risk of environmentally hazardous fluid leakage 	<p><u>Advantages:</u></p> <ul style="list-style-type: none"> • Faster response time • Easy implementation of control systems • Reduced number of components and wiring • Less maintenance due to elimination of pads • Elimination of hazardous brake fluid • Simple software-based brake parameter adjustment depending on the driving conditions <p><u>Disadvantages:</u></p> <ul style="list-style-type: none"> • Complexity of the system • Additional load on the battery • Considerably new technology

A simple example of an EMB system is the drum brakes used in trailers where less braking torque is required. These brakes are actuated by an electromagnet installed in the drum brake instead of a hydraulic mechanism, attracting a magnetic rotating disk onto a stator. The friction generated between the stator and the rotor results in braking. Electric calipers developed by Delphi [2] and Continental [3] are examples of EMBs. In these systems, switched reluctance (SR) motors are used to squeeze the pads onto the rotating disk. Although permanent magnet DC motors are more efficient, easy to control and cost effective, SR motors are more attractive to braking applications due to their high temperature operation capability, robustness, dynamic bandwidth and fault tolerance [4-6]. The high cost of the SR motor and the requirement for a sophisticated control system are main drawbacks of using such motors in braking applications.

Another example of an EMB is the magnetorheological brake (MRB) [7-8]. These brakes employ magnetorheological fluids (MRFs), where the viscosity varies as a function of applied magnetic field. The MRF fills the gap between the stator and the rotor

in the brake, and active control of the fluid viscosity by controlling the external magnetic field results in a retarding force in the form of a varying shear stress [9-10].

Eddy current brakes (ECBs), which are the main focus of this thesis, are another type of EMBs. ECBs using DC fields are already being used in heavy vehicles such as trucks, busses, trains and garbage collectors. They provide assistive braking to the main CHBs in order to decrease the braking load at high travel speeds [11].

Eddy currents are swirl-like electric currents generated on the surface of materials by means of a varying magnetic field. These currents are formed as a reaction to the varying applied magnetic flux. The main principle behind an ECB is the conversion of the kinetic energy of a rotating disk into resistive heat, by generating eddy currents that oppose the varying magnetic field.

A 3-D schematic diagram of an ECB concept is shown in Figure 1-3. It is comprised of a highly conductive disk (2) connected to the wheel shaft (4) and a stationary electromagnet(s) (1) mounted to the vehicle's chassis. When current is applied to the windings of the electromagnet (3), a magnetic field is generated between its poles and eddy currents are formed on the surface of the rotating disk under the pole projection areas of the electromagnet.

In addition to the advantages listed in Table 1-1, there are a number of additional characteristics that make ECBs a natural solution in electrical vehicles. The main motivation of the thesis is to improve the braking performance of ECBs coupled with the following properties: contactless braking, silent operation, no friction, natural capacity to imitate an automated brake system (ABS), which can be achieved with the replacement of the existing brake systems with ECBs. However, the current issue of the existing ECB's limiting braking torque at low vehicle speeds needs to be addressed before realizing a wide range of practical applications as a stand-alone ECB. Note that ECBs can readily be found in the following applications by means of assistive braking: to slow down a high inertia actuator, to help braking of heavy vehicles such as trains and heavy trailers, to adjust the stiffness of exercise equipment (e.g., exercise bikes), etc. Especially, slowing high-speed trains down to speeds where conventional brakes would be more effective is one of the key applications of ECBs [12-16].

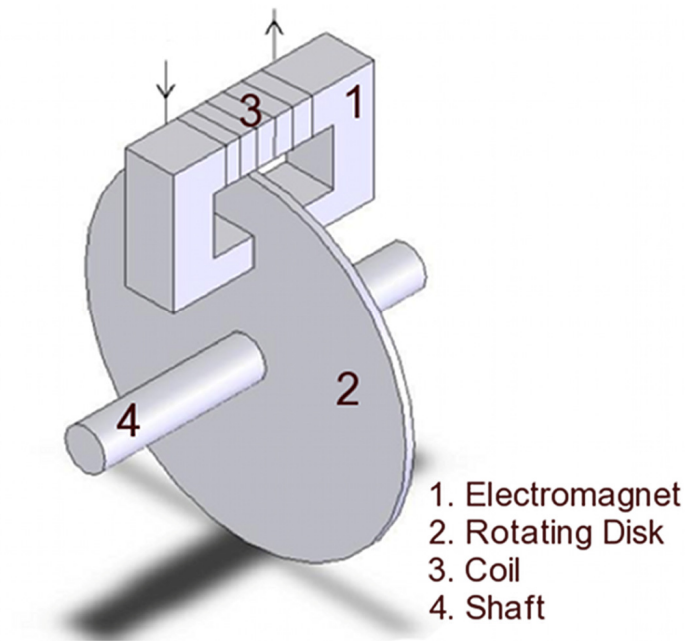


Figure 1-3. Eddy current brake (ECB) concept

Eddy currents generated on a rotating disk were first modeled by Smythe [17]. He used Maxwell-Ampere law in order to relate the current flow on the surface of the conductor to the applied magnetic field. Then by using Faraday's law and Gauss' law, he obtained the induced magnetic field generated due to the eddy currents in terms of the external field. An important conclusion he drew was that eddy currents cause demagnetizing fields on electromagnets that oppose the applied field and this results in a variation in the eddy current distribution.

Similar to Smythe's studies, Scheiber [18,19] studied the effects of a magnetic field on a moving conductor with low magnetic Reynolds number, which means that the thickness and the speed of the conductor is considerably small so that the skin effects (i.e. eddy currents) and the induced field effects can be neglected. In [19], using the magnetic potential of the generated eddy currents, Scheiber calculated the total eddy current power input to a rotating conductor. Then by using the correlation between the power and the torque, he obtained the braking torque by dividing the power by the angular velocity.

Unlike the previous works by Smythe and Scheiber, Wiederick [20] used another method to model the eddy currents on a moving sheet. According to this model, with the

help of experimental data, one can get the electrical resistance of the pole projection area (PPA). By applying Lorentz's Force law, he described the eddy currents in terms of the resistance and the induced voltage due to the applied magnetic field. His model was then revised by Heald [21], who used Coulomb's law to obtain the surface charges in the PPA and the electric field generated due to these charges.

Note that the above studies were limited to slow moving speeds of conductors. Wouterse [22] carried out a theoretical study on the effects of high rotational speeds in terms of the eddy current generation. His results for the low speeds matched the results of Scheiber and Smythe, while providing an understanding into the underlying physics of eddy currents in the high speed region. Subsequently, Wouterse's model was used by Simeu and Georges [23] and Barnes et al. [24] for the purpose of designing ECBs.

In addition, there has been a number of works that used finite element method (FEM) for studying ECBs. Burais et al. [25] looked into the eddy current generation on a moving conductor. Peterson [26] investigated the effects of having a conducting ferromagnetic body exposed to external magnetic field, while Conraths [27] investigated not only the eddy current generation but also the temperature change within the moving conductor. More recently, Lee and Park [28-31] studied the eddy current distribution on the ECB when DC field is applied, and their model was considerably more accurate than the previous models. This model was adapted in this work in order to validate our finite element model (FEM) of the ECB. Thus, the model is described in detail in Chapter 2.

Apart from the above works, eddy current based braking has mostly been researched for railroad vehicles. Unlike the circular disk type ECB configuration described in this work, trains commonly employ an array of linear ECBs [12-16]. Due to the fundamental difference in the configuration, these works are not discussed here in detail.

While a common assumption made in the above previous studies has been that the external magnetic field is time invariant (i.e. DC), Lee and Park [28] proposed the use of sinusoidal field application (i.e. AC) to improve the braking torque generation of ECB at low velocities. In [28], the braking torque generation was studied using numerical techniques on a configuration with 3 PPAs and the frequency of the applied field was optimized for better braking torque generation. For the study in [28], the induction effects were eliminated with the use of laminated magnetic core. While Lee and Park's study

[28] is the first work that proposed an AC based magnetic field application to increase the capacity for the eddy current generation. The explicit use of such a field for resolving an ECB's braking torque limitation at low speeds has been performed in this thesis and published in 2012 [32]. Here, an accurate finite element model (FEM) that accounts for the time varying field application was created and with the help of this model of ECB, the use of AC magnetic fields with fixed and variable frequencies in different waveforms was investigated at both low and high speeds. Results showed that the braking torque significantly increases with the application of frequency-modulated time varying fields.

In order to effectively deal with the problem of reduced braking torque at low speeds, the use of the time varying (i.e. AC) magnetic field is studied in this thesis. Although there is no in-depth study on the use of AC fields for improving the ECB braking torque, eddy currents are modeled on various surfaces that are stationary in order to study the power loss in electronic components and to find defects on conducting sheets.

Yannopoulos et al. [33] modeled the eddy currents generated in a stationary cylindrical shell of infinite length when there is alternating magnetic field is present. They used the Maxwell's equations and appropriate boundary conditions to solve for the flux and the associated loss as well. He also obtained numerical solution to the problem using Gauss-Laguerre method and this model was used to validate the analytical model along with experimental data.

A similar work was published by Sathuvalli et al. [34]. In his work, they calculated the Lorentz forces on a conductive sphere placed in alternating (sinusoidal) magnetic field. The study expressed the eddy currents generated in terms of the source functions and it also accounted for the skin effects. In addition to the analytical model, a numerical model was also obtained and a procedure was presented to determine the magnetic pressure distribution on the surface of a liquid metal droplet.

Unlike others, in [35] Siakavellas studied the eddy current generation on the surface of conductive plates with different shapes using shape dependent factors such as equivalent resistance of the plate and the total circulation current. Using their model, it is possible to estimate the eddy currents generated on the surface of the conductor plate using the shape dependent parameters he defined, however the accuracy strongly depends on the shape of the plate. Finally, he suggested improvements with the consideration of the principle of

minimum energy dissipation and he validated his analytical model with numerical analysis.

Similar to Sathuvalli's work, Lohofer [36] studied the eddy current generation as well as the vector and scalar potentials on a conducting sphere exposed to time-varying magnetic field. His study showed that there is no radial component of the eddy current density in the sphere. This model can be used as a contactless inductive measurement of electrical conductivity of metallic melts, since the impedance and the power absorption of the sphere can be obtained using his model.

In one recent study [37], Sinha et al. investigated the eddy current generation on conductive plates. They investigated the eddy current generation on the vacuum chambers of an accelerator. Their analytical model uses a potential term that is used to define the field terms and using this model, they calculated the power losses at different frequencies as well as the magnetic force acting on the plate due to the interaction between applied and induced fields.

In the studies mentioned above, the eddy currents are modeled on various types of surfaces that are stationary with the consideration of time varying field application. In this study, to be able to realize an ECB problem, in addition to the effects of time varying field application, the eddy currents are modeled on a rotating circular plate.

1.2 Objectives and contributions

The main objectives of this study are as follows:

- To perform a literature review to gain an understanding of the eddy current phenomenon and to gather knowledge on the state-of-the-art on eddy current braking technologies.
- To develop an analytic model of the eddy current generation under DC and AC magnetic field applications to a rotating conductor (brake disk) for theoretical analysis, optimization and control design purposes.
- To develop accurate electromagnetic FE models for the eddy current density generation under AC and DC field application to validate the analytical model (and vice versa), and for design and optimization purposes.

- To design an optimum ECB for higher eddy current density generation with AC field application with consideration of the following parameters: geometric dimensions, shape (e.g., sinusoidal or square wave), frequency, and magnitude of the AC field to realize a stand-alone ECB for automotive applications.
- To develop of a nonlinear model predictive controller for ECB that provides improved braking performance with AC field applications.
- To design and setup an experimental control test bed to validate theoretical and numerical results in current and future studies.

1.2.1 Contributions

The main contributions of the thesis research are as follows:

- In order to improve the performance of the ECB, the application of the AC magnetic fields is proposed. Preliminary results showed that this effectively increases the eddy current density generation capacity over the surface of the ECB's rotating/conducting disk, and hence provides an increased braking torque capacity.
- From a theoretical contribution point of view, there is no previous work on modeling of the physics behind the eddy current generation on a rotating conductor due to an AC magnetic field. An accurate AC model was created and studied for analysis and control design purposes.
- An accurate FEM was created to study the eddy current generation over the surface of the rotating disk. This model was then used to validate the analytical ECB model with the consideration of the AC field application.
- With the help of the numerical and analytical models, the braking torque generation is studied for various fields that are applied in different waveforms with consideration of frequency modulation to improve the results and then an optimum configuration is found using a stochastic optimization algorithm. Results show that the braking torque significantly increases with the use of multiple PPAs and even exceeds the required torque generation of CHBs in passenger vehicles.

- A nonlinear controller is designed and the braking performance is further improved with the use of this controller.

1.3 Thesis Outline

In Chapter 2, an analytical model is created for the existing ECB problem. The braking torque is calculated using the scalar and vector potential terms. By rearranging Maxwell's equations, a generic potential equation can be obtained for the electromagnetic problem and then, with the proper assumptions; the governing equations are converted into a Helmholtz form. Next, with the help of Green functions and adequate boundary conditions, the magnetic vector potential term, which is used to solve for the braking torque generation, is described. In order to validate the analytical model, a FEM was created and the results show good agreement between the analytical and numerical results. In addition, the results also show increase in the braking torque with the AC field application compared to DC field application onto the rotating disk of the ECB.

In Chapter 3, an accurate FEM was created to study effects of various types of AC fields applied. This model was also used to validate the analytical model introduced in Chapter 2. The model accounts for electromagnetic phenomena such as skin effects as well as the displacement currents although they are considerably small in value compared to conductive current terms at low frequencies. Braking torque generation using AC fields with sinusoidal, triangular, square and sawtooth waveforms are studied as well as the effects of frequency modulation on the braking torque generation are explored. Results show significant improvements with specific waveforms with frequency modulation.

In Chapter 4, using the outcomes of the previous section, an ECB is optimized using stochastic optimization algorithms. More specifically, a genetic algorithm is selected. The optimization problem is defined using geometric design variables, e.g., diameter and thickness of the disk, as well as field dependent variables, e.g., frequencies and phase differences, and number of PPAs. In addition, comfort levels are quantified and added as a constraint to the existing optimization problem for comfortable braking performance. The results show that the braking torque significantly increases with the introduction of an additional PPA and also with an optimum four-PPA configuration, the braking torque exceeds the requirements for slowing down a passenger vehicle.

In Chapter 5, a model based predictive controller for the optimum four-PPA configuration is designed. In order to do so, a dynamical model is created with the help of the analytical model presented in Chapter 2 and the numerical FEM of the ECB from Chapter 3. Using this dynamic model, a model predictive controller is also developed. The results show significant performance improvements during a number of braking scenarios presented here.

In Chapter 6, the experimental studies that have been carried out for DC field application are summarized and the results are given. This chapter mainly focuses on the design and development of a test bed for ECB and it is proposed that the effects of AC field application will be studied using the existing setup with necessary modifications.

Finally in Chapter 7, conclusions summarizing contributions of each chapter are presented. This chapter also has the future work planned for the ECB research. Initially, a prototype for studying the braking torque generation under AC field application should be built and the braking torque generation under AC field application needs to be studied. And then the controller should be implemented and the braking performance should be studied in real time. As a further step, after the experimental studies are concluded, the regeneration of energy lost during braking by means of eddy currents need to be investigated. In addition, a number of recommendations are listed in this chapter for the study presented in this thesis.

2. ANALYTICAL MODELING OF EDDY CURRENT BRAKES WITH THE APPLICATION OF TIME VARYING MAGNETIC FIELDS

2.1 Introduction

As was mentioned earlier in the previous chapter, the main motivation behind this study on ECB is the potential performance improvements, such as contactless braking, silent operation, no friction, natural capacity to imitate an ABS for automotive applications, etc., that can be achieved with the replacement of the existing brake systems with ECBs. However, the braking torque generation of the ECB is directly related with the rotational speeds of the conductive disk, therefore the main problem of the existing ECB's limited braking torque at low rotational speeds needs to be addressed before realizing a wide range of practical applications as a stand-alone ECB.

In terms of the ECB literature, Smythe [17] was the first one to investigate the eddy current generation on a rotating disk using governing Maxwell's equations and following his studies; there has been a number of analytical (e.g., Scheiber [18,19], Wouterse [22], Lee et al. [28-31]), numerical (e.g, Burais et al. [25], Peterson [26], Conraths [27]) and empirical (e.g., Wiederick [20], Heald [21]) studies that were published.

While a common assumption made in the above previous studies has been that the external magnetic field is time invariant (i.e. DC), Lee and Park [28] proposed the use of sinusoidal field application (i.e. AC) to improve the braking torque generation of ECB at low velocities. In [28], the braking torque generation was studied using numerical techniques on a configuration with 3 PPAs and the frequency of the applied field was optimized for better braking torque generation. For the study in [28], the induction effects were eliminated with the use of laminated magnetic core. While Lee and Park [28] is the first work that proposed that an AC based magnetic field application could increase the capacity for the eddy current generation, the explicit use of such a field for resolving an ECB's braking torque limitation at low speeds has been studied and presented previously in [32]. In [32], an accurate finite element model (FEM) that accounts for the time varying field application was created and with the help of this FEM of ECB, the use of AC magnetic fields with fixed and variable frequencies in different waveforms was

investigated at both low and high speeds. Results showed that the braking torque significantly increases with the application of frequency-modulated time varying fields.

In this chapter, the eddy current generated over the surface of the rotating conductor is modeled using analytical equations in order to calculate the braking torque generation of an ECB configuration. Eddy currents are modeled on various surfaces, such as cylindrical shells (Yannopoulos et al. [33]), spheres (Sathuvalli et al. [34], Lohofer [36]) and conductive plates (Siakavellas [35], Sinha et al. [37]) that are stationary.

In these studies, the common assumption made was that the surfaces where the eddy currents are generated are stationary. However, in terms of the ECB problem, in addition to the effects of time varying field application, the eddy currents are modeled on a rotating circular plate, thus the rotational terms will be included in the ECB model to solve for the eddy current distribution over the surface of the conductive disk.

In this chapter, the main objectives are to study and investigate the physics behind the eddy current generation on a rotating conductor when there is AC field is present and to create an analytical model to be used later for control design purposes. The analytical model is developed using the governing Maxwell's equations. The governing equations are reorganized and the field variables are redefined using the potential terms in this equation. With the proper boundary conditions and assumptions for the ECB problem, a well-known PDE form, Helmholtz equation, is obtained and it was solved using green functions. Then for validation purposes a FEM is created. The analytical and numerical results show good agreement and the reasoning behind the difference observed between these results is addressed in the discussion section of this chapter. In addition, the results prove that the AC field application improves the braking torque generation not only at low speeds but also high speeds as well for the configuration selected in this chapter.

2.2 Analytical modeling of eddy currents

In this section, the eddy currents generated on the surface of a rotating conductor is modeled using the vector and scalar potential terms. Along with the constitutive relations (Eqs. (2.6) and (2.7)) and Lorentz force law (Eq. (2.5)), Maxwell's equations (Eqs. (2.1)-(2.4)) are used to describe the field terms in terms of sources as follows:

$$\nabla \times \mathbf{H} = \mathbf{J} + \frac{\partial \mathbf{D}}{\partial t} \quad (2.1)$$

$$\nabla \times \mathbf{E} = -\frac{\partial \mathbf{B}}{\partial t} \quad (2.2)$$

$$\nabla \cdot \mathbf{D} = \rho \quad (2.3)$$

$$\nabla \cdot \mathbf{B} = 0 \quad (2.4)$$

$$\mathbf{F} = q(\mathbf{E} + \mathbf{v} \times \mathbf{B}) \quad (2.5)$$

$$\mathbf{D} = \varepsilon \mathbf{E} \quad (2.6)$$

$$\mathbf{B} = \mu \mathbf{H} \quad (2.7)$$

where \mathbf{B} is the magnetic flux density, \mathbf{H} is the magnetic field intensity, \mathbf{E} is the electric field, \mathbf{D} is the displacement flux density, \mathbf{J} is the current density, \mathbf{F} is the Lorentz force, \mathbf{v} is the linear velocity of a point on the conductor surface, q is the electric charge particle, ρ is the charge density, μ is the magnetic permeability and ε is the electric permittivity of the medium.

When the disk rotates, eddy currents are generated on its surface according to the Faraday's law (see Eq. (2.2)) due to the applied external magnetic field. Electric field will be generated when there is a change in the magnetic flux due to motional effects (rotation of the conductor) and/or transformer effects (alternating field application). For the basic ECB problem, a domain shown in Figure 2-1 was selected. The outer circular shape represents the conductor disk and the inner rectangular region is the PPA, i.e. the area that the external magnetic field is applied onto.

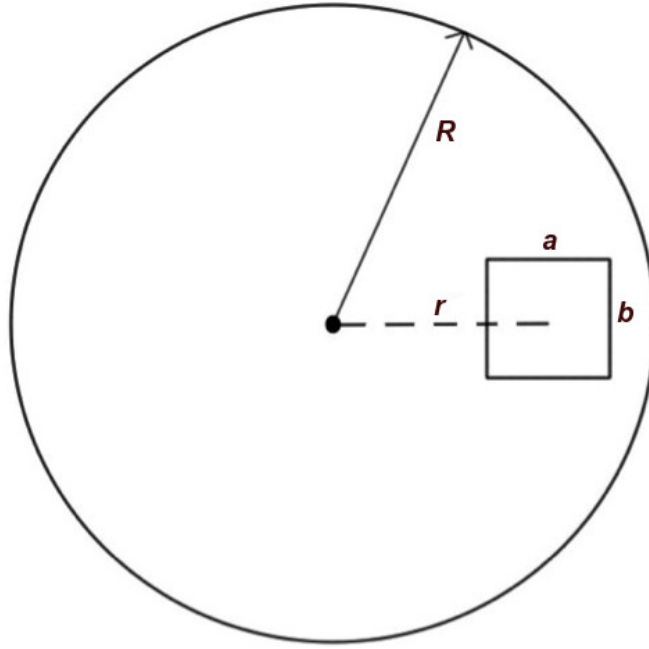


Figure 2-1. Basic ECB domain considered for simulating the eddy current generation

Eq. (2.5) is used to solve for the Lorentz force when there is a particle moving in external magnetic field and electric field. Using this relation, the eddy currents generated due to external electric fields and magnetic fields can be defined as:

$$\mathbf{J} = \sigma(\mathbf{E} + \mathbf{v} \times \mathbf{B}) \quad (2.8)$$

where σ is the conductivity of the rotating disk. As the next step, using its divergence free nature (see Eq. (2.4)), magnetic field is expressed in terms of the curl of a vector that is known as magnetic potential vector, \mathbf{A} , i.e.

$$\mathbf{B} = \nabla \times \mathbf{A} \quad (2.9)$$

Also the electric field term can be written in terms of a scalar potential (i.e. φ) as follows:

$$\mathbf{E} = -\nabla\varphi - \frac{\partial\mathbf{A}}{\partial t} \quad (2.10)$$

After the magnetic terms are defined, Eqs. (2.1) and (2.3) are rewritten using Eq. (2.8) as well by defining the following potential terms, which are the potential representation of the Maxwell's equations:

$$\nabla \times (\nabla \times \mathbf{A}) = \mu\sigma \left(-\nabla\varphi - \frac{\partial \mathbf{A}}{\partial t} + \mathbf{v} \times (\nabla \times \mathbf{A}) \right) + \mu \frac{\partial \mathbf{D}}{\partial t} \quad (2.11)$$

$$\nabla^2 \varphi + \frac{\partial \nabla \cdot \mathbf{A}}{\partial t} = -\frac{\rho}{\epsilon} \quad (2.12)$$

After obtaining the above potential equations, it is necessary to make a number of assumptions to be able to solve these equations to find the vector and scalar potentials. The assumptions that are used for simplifying Eqs. (2.11) and (2.12) are as follows

- It is assumed that the conductive disk is made of aluminum, thus the electric permittivity (ϵ) and the magnetic permeability (μ) is assumed to be equal to the vacuum's.
- As the external magnetic flux density, a uniformly distributed sinusoidal field with a magnitude B_0 is applied in perpendicular to the surface of the conductor disk:

$$\mathbf{B} = B_0 \sin(\Omega t) \mathbf{k} \quad (2.13)$$

where Ω is the angular frequency of the applied external field.

- Since magnetic flux density follows a sine curve, the electric field (see Eq. (2.2)) will follow a cosine curve and the magnetic potential (see Eq. (2.9)) will follow a sine curve:

$$\mathbf{E} = E_x \cos(\Omega t) \mathbf{i} + E_y \cos(\Omega t) \mathbf{j} \quad (2.14)$$

$$\mathbf{A} = A_x \sin(\Omega t) \mathbf{i} + A_y \sin(\Omega t) \mathbf{j} \quad (2.15)$$

where E_x and E_y are the x and y component of the electric field and A_x and A_y are the x and y component of the magnetic vector potential.

- It is assumed that the current penetrates through the whole thickness of the conductor and it is uniformly distributed across the cross section, i.e. no skin

effects on the conductor. Note that this assumption makes it possible to eliminate the variation of field variables along the thickness and the problem can be simplified to a 2-D problem. As a result of this assumption, Eq. (2.8) can be revised as follows:

$$\mathbf{J}^s = \sigma d(\mathbf{E} + \mathbf{v} \times \mathbf{B}) \quad (2.16)$$

where \mathbf{J}^s is the surface current density (A/m), d is the thickness of the conductive disk.

- Displacement currents are assumed to be negligible at low frequencies.
- Coulomb gauge condition ($\nabla \cdot \mathbf{A} = 0$) is adopted so that unique potentials as the solution to the above equations can be obtained. With the inclusion of Coulomb's gauge, it is assumed that the instantaneous source terms can be used to calculate the potentials that are then used to calculate the field terms through differentiation.
- Since the external field is dominant over any residual or induced fields at low frequencies over the surface of the conductive disk, the effects of such fields are ignored. In order to realize a model with no induction fields, a laminated electromagnet core is utilized instead of a soft ferromagnetic core. According to this assumption, the external flux density is the only source of the magnetic vector potential, i.e.

$$\nabla \times \mathbf{A} = B_0 \sin(\Omega t) \mathbf{k} \quad (2.17)$$

Eqs. (2.11) and (2.12), then, can be simplified using the above assumptions and the resulting potential equations are:

$$\nabla^2 \mathbf{A} = \mu \sigma d (\nabla \varphi + \frac{\partial \mathbf{A}}{\partial t} - \mathbf{v} \times \mathbf{B}) \quad (2.18)$$

$$\nabla^2 \varphi = -\frac{\rho}{\epsilon} \quad (2.19)$$

Note that Eq. (2.19) does not have any time-based operation (i.e. differentiation or integration). The same equation is also used to define the scalar potential when there is a static (DC) magnetic field applied instead of a time varying one. Thus, the solution of the scalar potential that is found for the DC application is also the solution to the AC application, as long as the charge density defined for both cases are equal. In order to check this condition, the total charge density is compared with the magnitude of the charge density that exists when there is time varying field.

Since the displacement currents are set to be zero at low frequencies, steady current conditions are satisfied, i.e. the divergence of the current density is equal to zero. Also, the divergence of the current density can be obtained using Eqs. (2.10) and (2.16) as follows:

$$\nabla \cdot \mathbf{J}^S = \nabla \cdot \left[\sigma d \left(-\nabla \varphi - \frac{\partial \mathbf{A}}{\partial t} + \mathbf{v} \times \mathbf{B} \right) \right] \quad (2.20)$$

Since the steady current assumption is valid, the term on the right hand side of Eq. (2.20) can be equated to zero and the Laplacian of the scalar potential can be obtained using the Coulomb's gauge and the final assumption in the above list, i.e.

$$\nabla^2 \varphi = \nabla \cdot (\mathbf{v} \times \mathbf{B}) \quad (2.21)$$

$$\rho = \nabla \cdot (\mathbf{v} \times \mathbf{B}) \quad (2.22)$$

Note that the Laplacian of the scalar potential is equal to the charge density.

Similar to Eq. (2.19), Eq. (2.22) also does not have any time-based operations. Thus, it is clear that the charge density does not change in the presence of DC or AC magnetic fields. Since the magnitudes of charge densities are the same for both cases, it is concluded that the scalar potential that is solved for DC magnetic field application is also the solution to the AC magnetic field application under the listed assumptions. Thus, in this paper, in order to solve for the magnetic vector potential, the scalar potential derived when DC magnetic field is applied is used.

$$\nabla^2 \mathbf{A} - \mu\sigma d \frac{\partial \mathbf{A}}{\partial t} = \mu\sigma d (\nabla\varphi - \mathbf{v} \times \mathbf{B}) \quad (2.23)$$

Since the time dependence is known for the magnetic potential vector (see Eq. (2.15)), time derivative of this term can easily be calculated, which can be expressed in terms of the magnetic potential itself as shown below:

$$\frac{\partial \mathbf{A}}{\partial t} = \frac{\Omega \mathbf{A} \cos(\Omega t)}{\sin(\Omega t)} \quad (2.24)$$

Being able to present the derivative term in terms of the potential itself makes it possible to rewrite Eq. (2.23) in a known form that is called the inhomogeneous Helmholtz equation:

$$\nabla^2 \mathbf{A} + \lambda \mathbf{A} = -\boldsymbol{\Phi} \quad (2.25)$$

where λ is the square of a constant called wave number that is positive and $\boldsymbol{\Phi}$ is a given vector field that is a function of the field terms and the material constants. For the ECB problem, these terms can be described as follows.

$$\lambda = -\mu\sigma d \frac{\Omega \cos(\Omega t)}{\sin(\Omega t)} \quad (2.26)$$

$$\boldsymbol{\Phi} = \mu\sigma d (-\nabla\varphi + \mathbf{v} \times \mathbf{B}) \quad (2.27)$$

Note that the inhomogeneous Helmholtz equation represented in Eq. (2.25) is in a vector form. This equation then can be separated into two parts: one for the x component and the other for the y component of the magnetic vector potential, i.e.

$$\nabla^2 A_x + \lambda A_x = -\phi_x \quad (2.28)$$

$$\nabla^2 A_y + \lambda A_y = -\phi_y \quad (2.29)$$

where ϕ_x and ϕ_y are the first and the second (x and y respectively) components of the vector $\boldsymbol{\Phi}$.

In order to be able to solve these two Helmholtz equations, λ , ϕ_x and ϕ_y have to be known and in addition to the values of these variables, proper boundary conditions have to be defined. From Eq. (2.26), it is clear that λ is a known time function and ϕ is a function of the scalar potential, velocity of the rotation and the externally applied field. The only unknown in this equation is the scalar vector potential; however it was previously shown that the solution for the electric potential in the presence of a DC field is also the solution to the time varying field application. Thus, the results obtained in [29] are adopted here to solve the time varying magnetic vector potential. Note that the negative divergence of the scalar potential needs to be calculated in order to solve the Helmholtz equation. From Eq. (2.10), it is clear that when there is no time variation, the electric field is equal to the negative divergence of the scalar potential.

In [29], the electric fields due to the charges accumulated at the borders of the PPA due to the Lorentz force that separates the charged particles are derived using an analogous method to calculate the magnetic pole density at the surface of a permanent magnet. Below in Figure 2-2, the PPA, moving in an externally applied magnetic field, is shown. As PPA moves in the externally applied field, Lorentz force causes separation, which will result in the accumulation of charge densities at the edges. Using these charge densities, the electric field can then be calculated. Eqs. (2.30) and (2.31) show the x and y components of the electric field distribution within the PPA with respect to a frame that is located at the left bottom corner (point O) of the PPA.

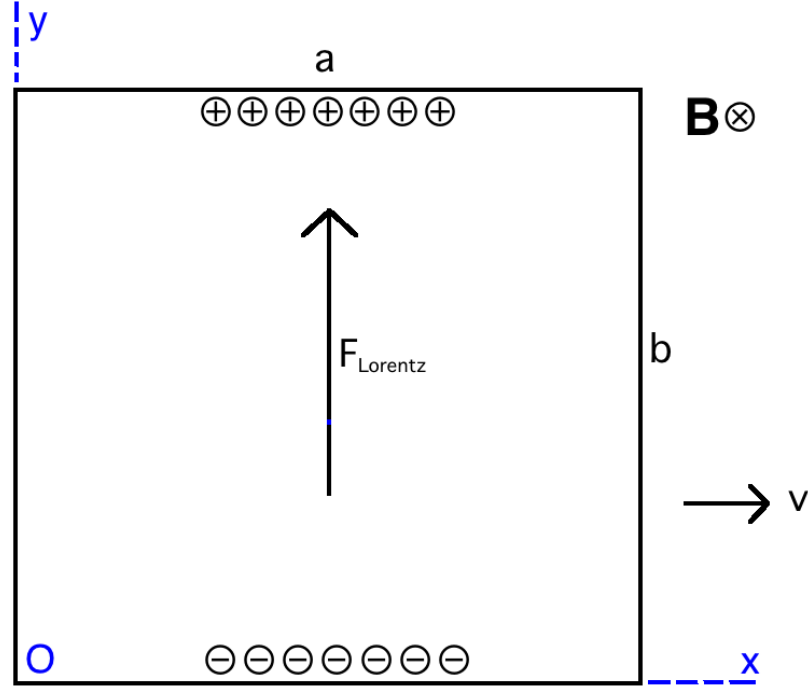


Figure 2-2. PPA moving in externally applied field.

$$\begin{aligned}
 E_{xDC} = \frac{wB_0}{4\pi} & \left[-(2r+b)\tan^{-1}\frac{y-a}{x-b} + (2r-b)\tan^{-1}\frac{y-a}{x} \right. \\
 & + (2r+b)\tan^{-1}\frac{y}{x-b} - (2r-b)\tan^{-1}\frac{y}{x} \\
 & \left. + \frac{a}{2} \ln \frac{\{4x^2 + 4y^2\} \{4a^2 + 4x^2 - 8ay + 4y^2\}}{\{(2b-2x)^2 + 4y^2\} \{(2a-2y)^2 + (2b-2x)^2\}} \right]
 \end{aligned} \tag{2.30}$$

$$\begin{aligned}
 E_{yDC} = -\frac{wB_0}{8\pi} & \left[-2a \left(\tan^{-1}\frac{b-x}{a-y} + \tan^{-1}\frac{x}{a-y} - \tan^{-1}\frac{x}{y} - \tan^{-1}\frac{x-b}{y} \right) \right. \\
 & + b \ln \frac{\{(a-y)^2 + x^2\} \{(a-y)^2 + (b-x)^2\}}{\{(b-x)^2 + y^2\} \{x^2 + y^2\}} \\
 & \left. + 2r \ln \frac{\{x^2 + y^2\} \{(a-y)^2 + (b-x)^2\}}{\{(b-x)^2 + y^2\} \{(a-y)^2 + x^2\}} \right]
 \end{aligned} \tag{2.31}$$

where r is the distance between the center of the conductive disk and the center of the PPA (see Figure 2-1), a and b are the width and the height of the PPA, respectively, and w

is the angular velocity of the rotating disk. For the rotating conductor, the velocity at any point can be written as follows:

$$\mathbf{v} = -w \left(y - \frac{b}{2} \right) \mathbf{i} + w \left(x + r - \frac{a}{2} \right) \mathbf{j} \quad (2.32)$$

The electric field terms, E_{xDC} and E_{yDC} in Eqs. (2.30) and (2.31), respectively, cannot be used directly as they represent the instantaneous field terms and do not vary with time. Faraday's Law can be used in order to identify the variation of these field terms with time. According to Faraday's Law, if the external magnetic flux density is expressed using a sine function as in Eq. (2.13), then the electric field term has to be expressed using a cosine function as shown in Eq. (2.14). Thus, for the current analysis, the electric field terms are used as shown below.

$$\mathbf{E} = E_{xDC} \cos(\Omega t) \mathbf{i} + E_{yDC} \cos(\Omega t) \mathbf{j} \quad (2.33)$$

Then, using Eq. (2.13), Eq. (2.32) and Eq. (2.33), Φ term can be expressed as follows:

$$\Phi = \mu \sigma d \left[\begin{matrix} E_{xDC} \cos(\Omega t) \\ E_{yDC} \cos(\Omega t) \end{matrix} + \begin{matrix} w B_0 (x + r - a/2) \sin(\Omega t) \\ w B_0 (y - b/2) \sin(\Omega t) \end{matrix} \right] \quad (2.34)$$

As the next step, the Helmholtz equation is solved using Green's theorem by defining boundary conditions [38]. The borders of the PPA that defines and limits where the externally applied flux density is are the primary boundaries to the AC problem. Since it is assumed that the externally applied flux density is applied only within the PPA, we can assume that the magnetic vector potential term is zero at the boundaries. This ensures that the flux term is zero outside the PPA. Then, the corresponding solution to the Helmholtz equation is as follows

$$\begin{aligned}
A_{x(y)} = & \int_0^a \int_0^b \phi_{x(y)}(\zeta, \eta) G(x, y, \zeta, \eta) d\eta d\zeta \\
& + \int_0^a \{A_{x(y)}(0, y)\}_{BC} \left[\frac{\partial}{\partial \zeta} G(x, y, \zeta, \eta) \right]_{\zeta=0} d\eta \\
& - \int_0^a \{A_{x(y)}(b, y)\}_{BC} \left[\frac{\partial}{\partial \zeta} G(x, y, \zeta, \eta) \right]_{\zeta=b} d\eta \\
& + \int_0^b \{A_{x(y)}(x, a)\}_{BC} \left[\frac{\partial}{\partial \eta} G(x, y, \zeta, \eta) \right]_{\eta=a} d\zeta \\
& - \int_0^b \{A_{x(y)}(x, 0)\}_{BC} \left[\frac{\partial}{\partial \eta} G(x, y, \zeta, \eta) \right]_{\eta=0} d\zeta
\end{aligned} \tag{2.35}$$

where η and ζ are the integration variables and $\{\dots\}_{BC}$ represents the boundary conditions at the corresponding edges of the PPA. Also, note that Eq. (2.35) is solved twice to obtain the x and y components of the magnetic vector potential separately with the corresponding values defined for ϕ and λ . In addition, the green function G that is selected to solve the above problem is given below.

$$G = \frac{1}{ab} \sum_m^\infty \sum_n^\infty \frac{\sin(p_n x) \sin(q_m y) \sin(p_n \zeta) \sin(q_m \eta)}{p_n^2 + q_m^2 - \lambda} \tag{2.36}$$

where

$$p_n = \frac{\pi n}{b} \tag{2.37}$$

$$q_m = \frac{\pi m}{a} \tag{2.38}$$

Note that once the boundary conditions are implemented in Eq. (2.35), the magnetic vector potential solution can be derived as follows:

$$A_{x(y)} = \int_0^a \int_0^b \phi_{x(y)}(\zeta, \eta) G(x, y, \zeta, \eta) d\eta d\zeta \tag{2.39}$$

Before deriving the final solution and carrying out braking torque calculations, the boundary of the conductive disk has to be accounted for. So far, the analytical model

solves for the magnetic vector potential in a PPA on an infinitely long conductive disk and in order to account for the actual boundary at the edge of the conductive disk, the method of images is used. This method is used to replace a boundary in front of a source with an imaginary source located on the other side of the boundary, as shown in Figure 2-3.

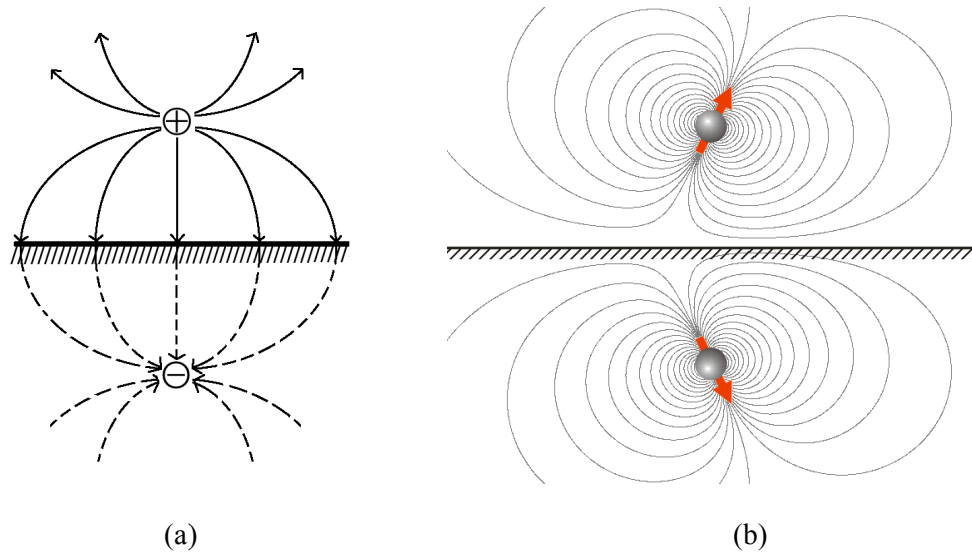


Figure 2-3. Method of images, a) electric charge, b) magnetic dipole

In Figures 4(a) and 4(b), the image sources for an electric charge and a magnetic dipole are presented, respectively. Assuming that these sources are placed in front of conductive surfaces, the field components can be calculated by replacing the surface with the image of the source as shown in the figure. Note that the magnitudes of the primary source and the imaginary source and the distances between the conductor surface and the sources are the same for both sources. Although they look similar, the major difference between the electric and magnetic sources in terms of the application of this method is that the normal component of the field to the surface of the conductor is reversed for the magnetic source.

In order to use the method of images, the cylindrical coordinates of the rotating disk needs to be transformed into a linear space using conformal mapping techniques. In [29], the same method was used to implement the boundary conditions at the edge of the conducting disk. Unlike [29], where the image of the electrical charges is obtained to find

the electric field distribution, the magnetic potential term (similar to magnetic dipoles) is the primary source in our problem and the image that is defined to implement the conductive disk's boundary condition is realized according to Figure 2-3 (b). A similar procedure to the one presented in [29] was carried out to find the imaginary sources herein. After carrying out the conformal mapping, the location of the imaginary sources outside the conductive disk can be found and the net magnetic vector potential is calculated using the following relations:

$$A_{x,net} = A_x^{(p)}(x, y) - A_x^{(i)}(x, y) \quad (2.40)$$

$$A_{y,net} = A_y^{(p)}(x, y) - A_y^{(i)}(x, y) \quad (2.41)$$

where

$$A_x^{(i)}(x, y) = -A_x^{(p)}(x^{(i)}, y^{(i)}) \quad (2.42)$$

$$A_y^{(i)}(x, y) = -A_y^{(p)}(x^{(i)}, y^{(i)}) \quad (2.43)$$

and

$$x^{(i)} = \left(\frac{a}{2} - r\right) + \left(\frac{R^2(-b/2+r+x)}{(-b/2+r+x)^2+(y-a/2)^2}\right) \quad (2.44)$$

$$y^{(i)} = \left(\frac{b}{2}\right) + \left(\frac{R^2(-a/2+y)}{(-b/2+r+x)^2+(y-a/2)^2}\right) \quad (2.45)$$

and R is the radius of the conductive disk. Note that the negative sign in Eqs. (2.42) and (2.43) results from the fact that the primary source is a magnetic term and the normal component of the image is in the opposite direction to the normal component of the primary source.

Once the magnetic vector potential is obtained using the equations presented above, the braking torque is calculated using the following formula:

$$T_b = \iint_S \mathbf{r}_P \times (\mathbf{J}^S \times \mathbf{B}) dS \quad (2.46)$$

where T_b is the braking torque and \mathbf{r}_p is the position vector and the magnitude of the position vector is r . In this equation, the magnetic flux density is known and the only unknown is the eddy current density. In order to find the eddy current density, Maxwell-Ampere Law is used. We can replace the field term in Eq. (2.1) with the magnetic vector potential as follows:

$$\frac{1}{\mu} (\nabla \times (\nabla \times \mathbf{A}_{net})) = \mathbf{J}^s \quad (2.47)$$

Also note that the displacement current term is zero due to low frequency application assumption. Using the above relation for the eddy current generated over the surface of the conductive disk, Eq. (2.46) can be rewritten and the braking torque can be calculated for the specific externally applied magnetic flux density (i.e. \mathbf{B}).

$$T_b = \frac{1}{\mu} \iint_S \mathbf{r}_p \times ((\nabla \times \nabla \times \mathbf{A}_{net}) \times \mathbf{B}) dS \quad (2.48)$$

2.3 Validation and preliminary results

In this section, the proposed analytical model is validated with our FEM presented in [32]. A commercial finite element method (FEM) software package, COMSOL Multiphysics[®], is used to simulate the eddy current distribution within the ECB. A partial differential equation (PDE) is obtained by reorganizing the Maxwell's equations for the ECB problem. This PDE is then solved using proper boundary conditions to obtain the eddy current distribution over the rotating disk. The flowchart of the FEM is shown in Figure 3-2. FEM contains two solvers, one is the PDE solver that solves the eddy current distribution and the other is an electromagnetic solver that introduces the effects of induction fields. For the validation purposes, since the analytical model neglects the induction effects by assuming a laminated electromagnet core, the induction field terms are removed from the numerical model as well.

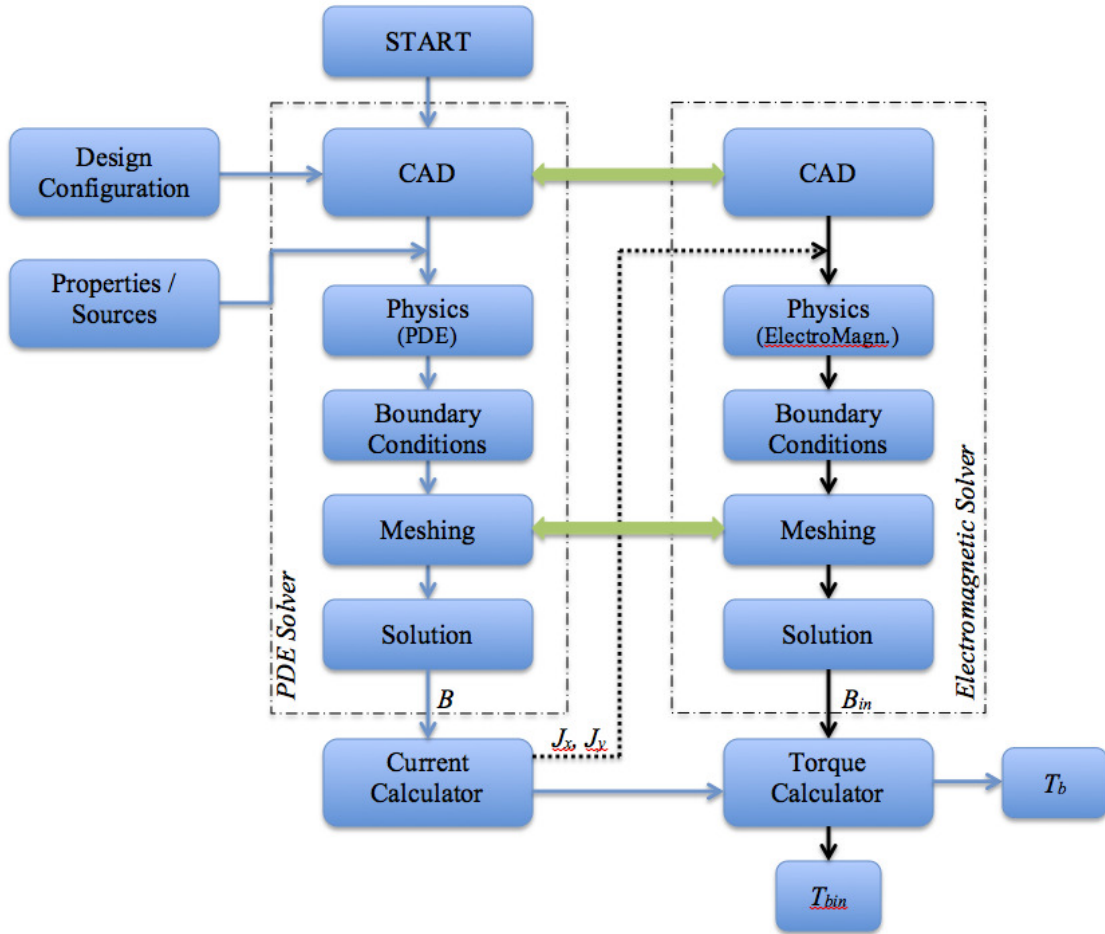


Figure 2-4. Flowchart of the FEM implementation

The domain selected for the problem is presented in Figure 2-1 and the configuration that is adapted here is taken from Lee and Park [29]. The configuration used for validation purposes is given in Table 2-1. Note that for the time varying field application, an externally sinusoidal field is applied with a root mean square (RMS) magnitude of 0.3 T. Herein, this RMS magnitude of 0.3 T is specifically selected in order to make the AC field application results comparable with the DC field application results presented in [29], which used a DC magnetic field of the same magnitude. This ensures that the same external energy input is supplied in both cases.

Table 2-1. Specifications of the ECB configuration

Radius of the disk, R (m)	0.05
Width of PPA, a (m)	0.02
Height of PPA, b (m)	0.02
Pole location distance, r (m)	0.0323
Thickness, d (m)	0.003
Material	Aluminum
Conductivity, σ (S/m)	5.79E+07
Externally applied magnetic flux density, B_0 (T RMS)	0.3

Before starting with the validation, there is an important step that needs to be carried out. In order to solve the Helmholtz equation defined in Eq. (2.25) for the AC field application in Sec. 2, a green's function is selected (see Eq. (2.36)). It is clear that the selected green's function is an infinite sum of sinusoidal function in space dependent coordinates, x and y , as well as the integration variables, ζ and η . Therefore, it is necessary to identify the convergence of this series to a solution as the parameters, m and n , increase. In order to verify the convergence, a simple pilot study is carried out where the braking torque is calculated for cases in which the parameters gradually increased. Note that for simplicity, the values assigned to the parameters, m and n , are kept equal (i.e. $m = n$). For this convergence study, the configuration in Table 2-1 is used and the frequency of the externally applied field and the angular rotation of the conductive braking disk were kept constant at 10 Hz and 100 rpm, respectively.

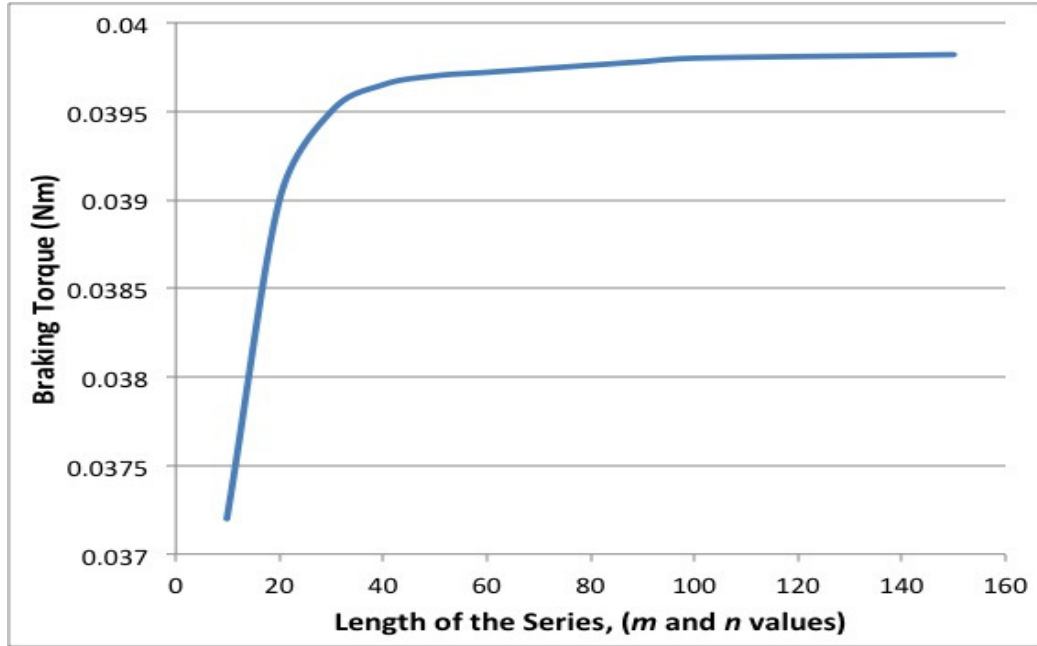


Figure 2-5. Convergence plot

In Figure 2-5, the variation of the braking torque with increasing m and n values is shown. From the figure, it is obvious that converge is achieved as the values increase. Note that the variation between the calculated braking torques when m and n are set to 40 versus 30 is 0.4%; however, when they are set to 50, as compared to 40, this variation goes down to 0.1%. Also, note from computational point of view, as the length of the series increases, the time required to obtain a solution increases quadratically. Therefore, for the subsequent simulations carried out in this section, the length of the series is set to 50.

For the main validation study, two different time varying field simulations are carried out. In the first case, the RMS braking torque generation is calculated using both the FEM and the analytical model at a constant rotational speed and the effect of the frequency variation in braking torque generation is investigated. For the second case, while the frequency of the applied magnetic flux density is kept constant, the variation of the RMS value of the braking torque generation is plotted with respect to varying angular speeds of the rotating disc in order to study their effect on the braking torque generation.

In Figure 2-6, the variation in the braking torque generation with increasing frequencies is shown using both the analytical and FE models. It can be concluded that

under the assumptions mentioned in the previous sections, for the relatively low frequency range shown in the figure, the braking torque does not depend on the frequency as the models do not account for the induction terms. In addition, at any given frequency, the difference between the analytical and FE models is around 10%. Note that the braking torque results presented in this section are given in terms of the RMS values.

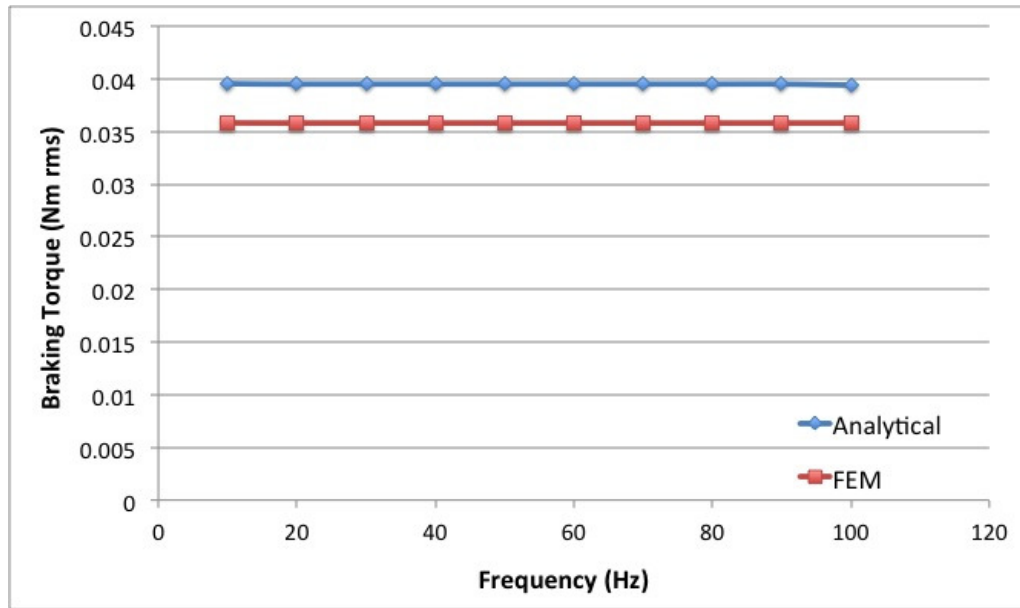


Figure 2-6. Variation in braking torque with frequency of the externally applied magnetic flux density

Next, the variation of braking torque with increasing angular velocities of the rotating brake disk is presented in Figure 2-7. Under the assumptions made previously to create the models, the braking torque increases linearly with increasing angular velocities. From the figure, the difference between the analytical model results and FEM results is found to be around 10% across all velocities as well.

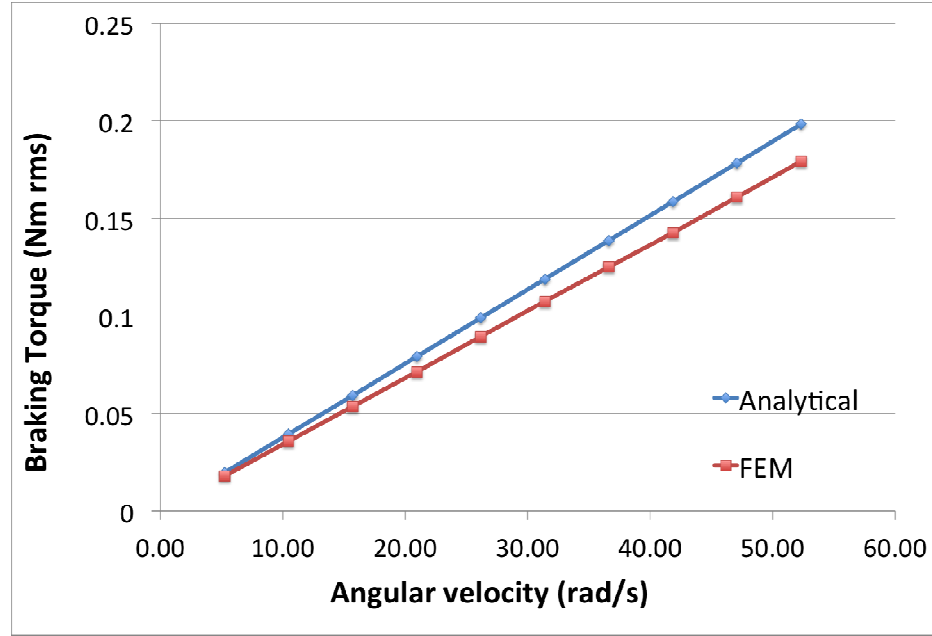


Figure 2-7. Variation in braking torque with angular velocity of the rotating brake disk

For both figures, it can be concluded that the trend of the variation in results with increasing frequencies and increasing angular velocities are the same for both the analytical and FE model simulations. In addition, the difference between these curves is about 10% at any given frequencies or angular velocities; and, thus, it can be concluded that the results of analytical model and FEM are in good agreement. Note that the reasoning behind the 10% difference and the nature of the variations in Figure 2-6 and Figure 2-7 are discussed in detail in the following section.

2.4 Discussion

The results of the analytical model and the FEM simulations were given in the previous section when there is variation in frequency and angular velocity. These results presented in Figure 2-6 and Figure 2-7 show that the models are generally in good agreement in terms of the variation of the braking torque with respect to the AC field frequency and rotating disc velocity. The difference is calculated to be around 10% in the braking torque generation across the frequency and velocity ranges of angular velocities and various frequencies at the range investigated in this paper. Below, a number of reasons that cause this difference are discussed in detail.

In order to understand the source of this difference, the analytical and FE modeling procedures must be considered again. The analytical model was created using a number of assumptions that made the problem vary slightly from the one solved using the FEM. Although the effects of the displacement currents are minimal at the low frequency region, the field equation used for FEM accounts for the displacement currents, whereas the analytical model assumes that they are negligible. For instance, analytical model does not account for skin effects and the current is assumed to be distributed uniformly along the thickness. However, at high frequency AC field application, analytical model results in higher current densities due to this assumption and the braking torque calculated will be higher than the real braking torque generation.

Apart from this, the major source of the difference is the last assumption made in the analytical modeling procedure. This assumption states that the externally applied flux density is the only field term that exists on the surface of the conductor, thus any field term over the surface of the conductive disk due to the applied flux density is not included in the solution. Although the magnitude is significantly lower than the externally applied field, the residual field opposes the external flux density and therefore reduces the amount of the braking torque generation. On the other hand, FEM accounts for the residual magnetic flux term that is generated due to the application of the externally applied flux density. Use of this assumption explains the main reason behind the higher braking torque results calculated using the analytical model.

One last source of the difference is the numerical integration carried out to solve Eq. (2.48) for the braking torque using the analytical model. Since the equation is heavily dependent on the space coordinates, x and y , numerical integration methods are used to calculate the surface integral. The numerical method uses a solver that calculates the regional integrations over surfaces. However, when there is a circular area involved, it is harder for the solver to converge due to the curved nature of the edges of the domain and, therefore, the solver assigns an uncertainty value depending on the tolerances defined to identify the accuracy of the solution. Also, note that since this is a numerical integration, the computational effort increases with tighter tolerances. Herein, for the braking torque calculations of the ECB, the tolerances were adjusted so that the uncertainty is no more than 1% of the result obtained.

As the last step, the effect of the time varying field application is studied in this paper. The calculated braking torque that is generated when there is time varying field using the analytical model introduced here and the calculated torque generated when DC field is applied using the analytical model in [28] are compared at various rotational speeds in Figure 2-8. It is clear from the figure that the braking torque increases with the application of AC field and from the results, the change corresponds to over 40% increase for the given configuration assuming that the electromagnet core is laminated (thus there is no induction fields generated to oppose the external field on the core). Therefore, it can be concluded that the application of the time varying field results in increased braking torque in both low and high speed regions and it can also be concluded that there is a potential for the ECB to be used as a stand-alone brake actuator for certain applications.

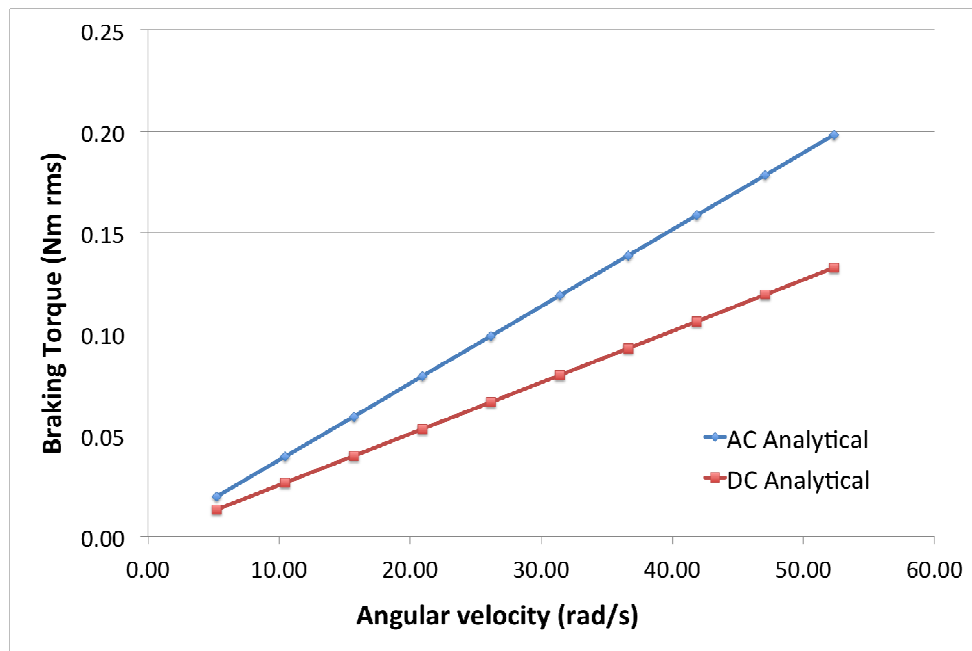


Figure 2-8. Comparison between braking torques generated with AC and DC field applications

Although the above results show its potential, in order to realize the stand-alone ECB, the generated braking torque has to be enough to stop a vehicle. Considering the torque amount presented in Figure 2-8, it can be concluded that the brake configuration has to be improved significantly in order to generate more braking torque. This can be achieved by optimizing the applied field characteristics (i.e. frequency, magnitude), geometric

variables (i.e. diameter, thickness, width and height of the PPA), material properties and number of PPAs.

As a follow up to the current work, the braking torque will be maximized with optimization techniques and using the presented analytical model, a controller will be designed and implemented for the ECB.

2.5 Conclusion

In this chapter, the effects of time varying (i.e. AC) field application on the braking torque generation of an ECB are studied. In order to calculate the braking torque, an analytical model is derived, which was then validated using an accurate FEM. The results of this study show both models are in good agreement, within about 10% error. In addition, the reasoning behind this error along with the physical nature of the variations of the braking torque with respect to the AC frequency and the angular velocity of the rotating disc was discussed in detail. Finally, our analytical results showed the application of the time varying field indeed increase the braking torque generation capacity of an ECB.

Appendix.2A. Analytical Model: DC field application

This model is valid for determining the torque value for the whole range of angular velocities under DC field application. Initially, a simple case, where eddy currents are generated on a moving conductive plate, was studied. Figure 2A.1 shows the schematic of the moving plate with a velocity, \mathbf{v} , in x direction. While the plate is moving, a constant magnetic field, \mathbf{B} , is applied perpendicular to the plate surface. Since the plate contains charged particles (q), they will feel a force, which is equal to $q\mathbf{v} \times \mathbf{B}$ according to Lorentz Law, due to the applied magnetic field. This force causes the charged particles to separate. As a result of this separation, an electric field, \mathbf{E} , between the upper and lower ends of the plate is formed.

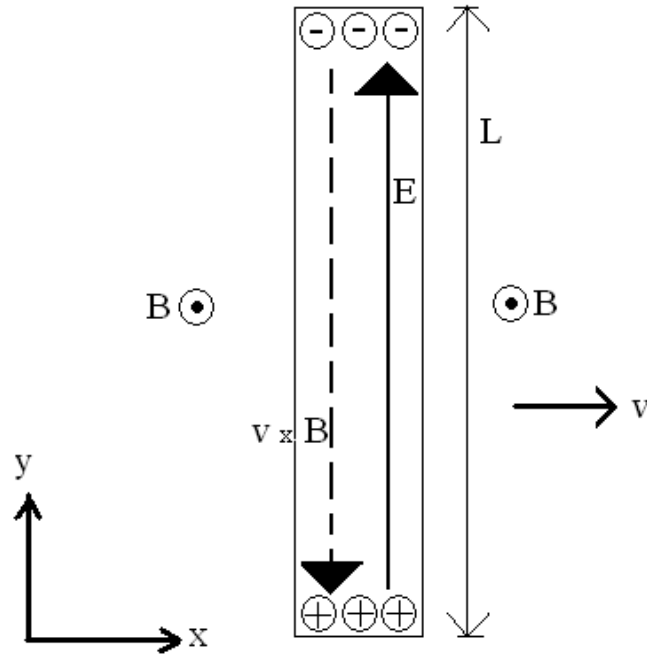


Figure 2A.1. Conductive plate moving with a velocity (adapted from [29])

$$\mathbf{E}_{\text{tot}} = \mathbf{E} + \mathbf{v} \times \mathbf{B} \quad (\text{A2.1})$$

$$\mathbf{J} = \sigma \cdot \mathbf{E}_{\text{tot}} \quad (\text{A2.2})$$

Eq. (A2.1) shows the total electric field generated (\mathbf{E}_{tot}) on a moving conductive plate. Due to the presence of electric field, eddy currents are formed on the conductive plate. As Eq. (A2.2) states, eddy current density, \mathbf{J} , is a function of the total electric field, \mathbf{E}_{tot} and the conductivity of the plate, σ .

In ECB, the conductor is circular and it rotates with an angular velocity, ω . In this orientation, eddy current generation is limited to the PPA. The simple schematic of the actual case is shown in Figure 2A.2. The arrows swirling in PPA represent the eddy currents generated.

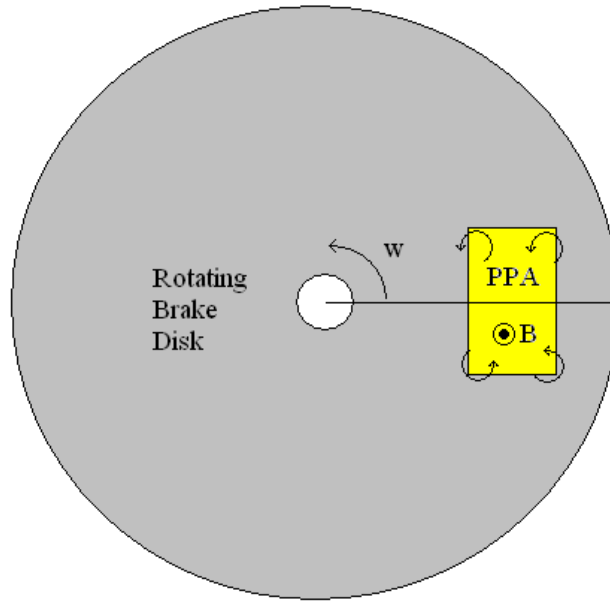


Figure 2A.2. Eddy currents formed on brake disk

Initially, the disk is assumed to have infinite radius and the velocity of an arbitrary point P in the PPA is defined in terms of the angular velocity of the disk and the position of the selected point. Figure 2A.3 shows the position and velocity of point P with respect to two different coordinate frames. One is the $x'y'z'$ frame which is positioned at the center of the brake disk, O' , and the other frame is $x y z$ which is placed at the center of PPA, O . The distance between O and point 'P' is denoted by r_d and the angle is ϕ'' and the distance between O' and point 'P' is denoted by r' and the angle is ϕ' . In addition to these, the relative distance between both frames is r .

The horizontal and vertical components of the velocity are defined in Eq. (A2.3).

$$v_x = v \sin \phi' = w r' \sin \phi' = w y \quad (\text{A2.3})$$

$$v_y = v \cos \phi' = w r' \cos \phi' = w (r + x) \quad (\text{A2.4})$$

where v_x and v_y are the scalar values of velocities in horizontal and vertical directions with respect to the $x y z$ frame.

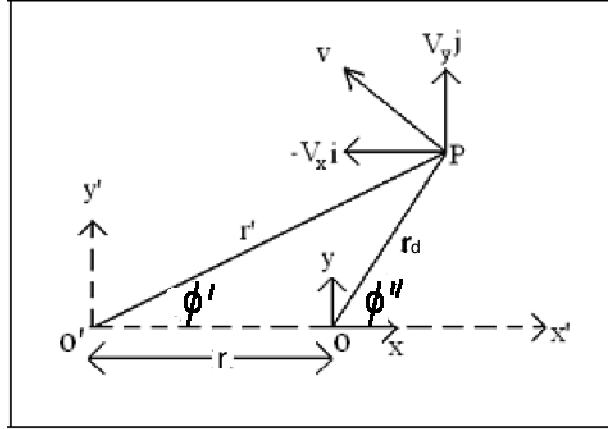


Figure 2A.3. Position and Velocity Representation of point 'P' (adapted from [29])

Due to the rotation, according to the Lorentz Law, a force is felt by the charged particles and this force causes separation. In Figure 2A.4, the separations between charged particles in vertical and horizontal directions are shown individually. The figure on the left depicts the separation due to velocity in vertical direction and the other one presents the separation in horizontal direction. $2a$ and $2b$ are the height and width of PPA respectively. Surface charge densities on the edges of the PPA are defined in Eq. (A2.5), by applying a method used to calculate the surface charge density of a permanent magnet [39].

$$\rho_{sx+} = \epsilon w(r+a)B_0 \quad (\text{A2.5})$$

$$\rho_{sx-} = -\epsilon w(r-a)B_0 \quad (\text{A2.6})$$

$$\rho_{sy+} = \epsilon wbB_0 \quad (\text{A2.7})$$

$$\rho_{sy-} = -\epsilon wbB_0 \quad (\text{A2.8})$$

where $\rho_{si+,-}$ is the surface charge density on the edge perpendicular to i axis (i.e. x or y) in the positive (+) or negative (-) quadrant with respect to axis i and ϵ is the permittivity of vacuum. Since field \mathbf{B} is assumed to be perpendicular to the surface of the disk, scalar value of the field, B_0 is used to define the applied field.

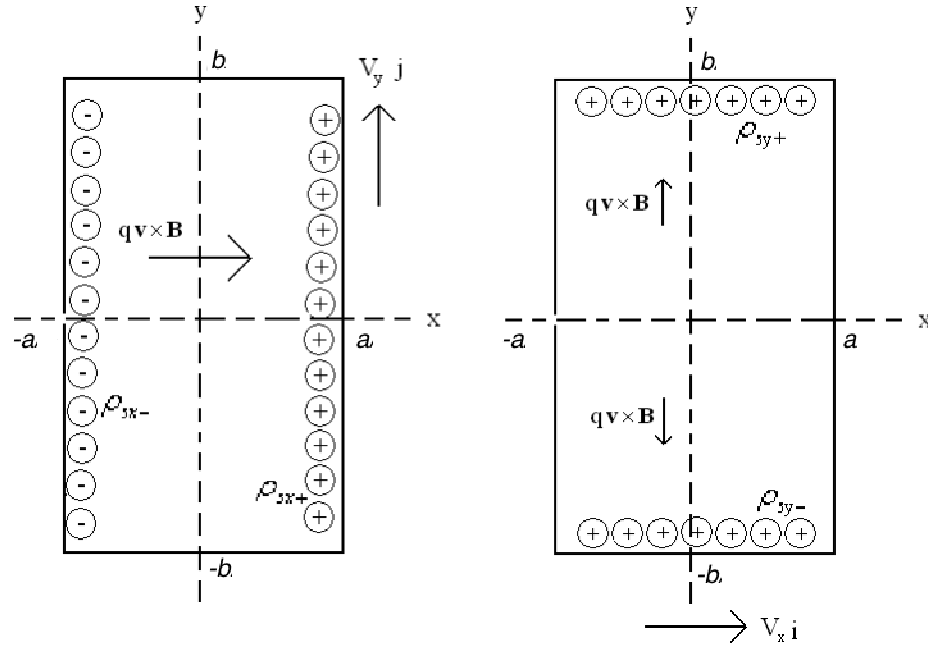


Figure 2A.4. Surface charge density distribution due to the velocity in y direction (adapted from [29])

From the surface charge densities, the electric field between positive and negative charges is calculated using line charge densities, which are the integrals of the surface charge densities over the corresponding edge. Equations (A2.9) and (A2.10) show the horizontal and vertical components of the electric field, i.e. E_{xDC} and E_{yDC} , at an arbitrary point P located at (x, y) .

$$\begin{aligned}
 E_{xDC} = \frac{wB_0}{4\pi} & \left[-(2r+2a)\tan^{-1}\frac{y-b}{x-a} + (2r-2a)\tan^{-1}\frac{y-b}{x+a} \right. \\
 & + (2r+2a)\tan^{-1}\frac{y+b}{x-a} - (2r-2a)\tan^{-1}\frac{y+b}{x+a} \\
 & \left. + b \ln \frac{\{(2x+2a)^2 + (2y-2b)^2\} \{(2x+2a)^2 + (2y+2b)^2\}}{\{(2x-2a)^2 + (2y-2b)^2\} \{(2x-2a)^2 + (2y+2b)^2\}} \right]
 \end{aligned} \tag{A2.9}$$

$$\begin{aligned}
E_{yDC} = -\frac{wB_0}{4\pi} & \left[-4b \left(\tan^{-1} \frac{x+a}{y-b} + \tan^{-1} \frac{x+a}{y+b} - \tan^{-1} \frac{x-a}{y-b} - \tan^{-1} \frac{x-a}{y+b} \right) \right. \\
& + 2a \ln \frac{\{(2x-2a)^2 + (2y-2b)^2\} \{(2x+2a)^2 + (2y-2b)^2\}}{\{(2x-2a)^2 + (2y+2b)^2\} \{(2x+2a)^2 + (2y+2b)^2\}} \\
& \left. + 2r \ln \frac{\{(2x-2a)^2 + (2y-2b)^2\} \{(2x+2a)^2 + (2y+2b)^2\}}{\{(2x+2a)^2 + (2y-2b)^2\} \{(2x-2a)^2 + (2y+2b)^2\}} \right] \quad (A2.10)
\end{aligned}$$

After defining the electric field, the eddy current density can be calculated from Eq. (A2.2). Eddy current densities in horizontal, J_x and vertical, J_y , are defined as:

$$J_x = \sigma(E_{xDC} + w(r+x)B_0) \quad (A2.11)$$

$$J_y = \sigma(E_{yDC} + wyB_0) \quad (A2.12)$$

Up to now, it is assumed that the disk has no boundaries. In order to account for the finite radius, a fictitious current density is introduced outside the disk that cancels the radial component of the charge density on the boundary. Figure 2A.5 shows the boundary and the current densities; induced and the fictitious.

Induced current density is defined as the primary densities, denoted as $J_x^{(I)}$, $J_y^{(I)}$, which are defined in Eqs. (A2.11) and (A2.12). The fictitious eddy current density is denoted as $J_r^{(2)}$.

Due to the cylindrical geometry, the primary eddy current density is converted into cylindrical coordinates in Eq. (A2.13). Equation (A2.14) shows the boundary condition on the perimeter of the disk.

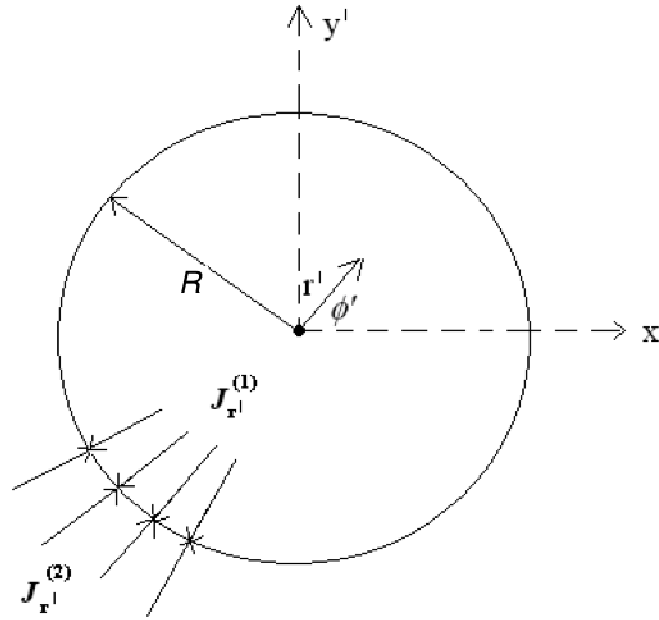


Figure 2A.5. Boundary conditions represented in spherical coordinates

$$J_{r'}^{(1)}(r', \phi') = J_{x'}^{(1)} \cos \phi' + J_{y'}^{(1)} \sin \phi' \quad (\text{A2.13})$$

$$J_r(R, \phi') = J_{r'}^{(1)}(R, \phi') - J_{r'}^{(2)}(R, \phi') = 0 \quad (\text{A2.14})$$

where R is the radius of the rotating disk.

Eddy current density on the surface of the disk at an arbitrary point P is calculated using mapping and method of images [29]. Equation (A2.15) shows the eddy current density as a function of primary and fictitious current densities.

$$J_r(r', \phi') = J_{r'}^{(1)}(r', \phi') - J_{r'}^{(2)}\left(\frac{R^2}{r'}, \phi'\right) \quad (\text{A2.15})$$

In order to account for the opposing magnetic field due to the eddy current density, a lumped way was adapted. Induced field is calculated using the Ampere's Law. According to Ampere's Law, the line integral of the magnetic field intensity around a closed loop gives the current flow through the area encircled by the closed loop. The closed loop chosen is shown in Figure 2A.6. The line integral of the intensity is equal to the current

enclosed in the loop. It is assumed that the permeability of the magnet core is infinite and there is no reluctance load due to the electromagnet core. In addition, the air gap between the magnet core and the disk assumed to be negligible.

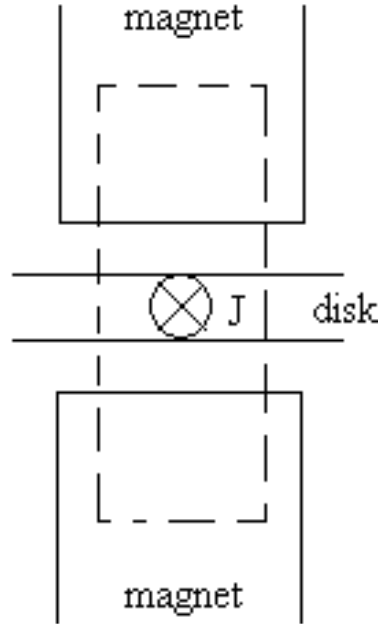


Figure 2A.6. Chosen closed loop

$$2l_g H_i = I_{r'} \quad (\text{A2.16})$$

where l_g is the distance between the electromagnet yokes, $I_{r'}$ is the net eddy current, calculated by integrating the eddy current densities generated in PPA numerically (i.e. by integrating Eq. (A2.15)).

Therefore the induced magnetic flux, B_i , was found to be:

$$B_{in} = \frac{\mu I_{r'}}{2l_g} \quad (\text{A2.17})$$

where μ is the permeability of the vacuum.

Magnetic Reynolds number is used to relate the induced and the applied fields:

$$R_m = \frac{B_{in}}{B_0} = \frac{\mu I_{r'}}{2l_g} \frac{1}{B_0} \quad (\text{A2.18})$$

where R_m is the magnetic Reynolds number.

When the angular velocity of the disk increases, magnetic Reynolds number increases and the net magnetic flux density in the air gap, B_z , decreases. The net magnetic flux density is written for the two extreme cases, when the angular velocity is zero, magnetic flux density is equal to the applied value and when the angular velocity is infinite, the net flux density is zero. With these two extreme cases, the net eddy current density is defined as:

$$B_z = B_0 e^{-R_m} \quad (\text{A2.19})$$

Finally the braking torque is calculated using Lorentz's law.

$$T_{bin} = -dB_z \int_S r' J_{r'} dS \quad (\text{A2.20})$$

where S denotes the surface area of PPA.

3. IMPROVED BRAKING TORQUE GENERATION CAPACITY OF EDDY CURRENT BRAKE WITH TIME VARYING FIELDS: A NUMERICAL STUDY

3.1 Introduction

As was previously mentioned in previous chapters, potential advantages such as the contactless braking, silent operation, no friction and natural capacity to imitate ABS, make ECB an attractive substitute to conventional friction brakes. However, ECB has a significant drawback, which is the reduction in the braking torque with decreasing velocities. This thesis proposes and extensively studies the effect of AC field application on the braking torque generation of ECB.

In the previous chapter, an accurate analytical model showed that the braking torque significantly increases with AC field application (specifically sinusoidal field with constant frequency) for the configuration selected. In this chapter, in order to effectively deal with the problem of reduced braking torque at low speeds, the effects of various types of AC field applications on a selected ECB configuration are studied.

Therefore, the main objective of this work is the development of an accurate electromagnetic FEM that can be used to simulate and analyze the exposing of the conductor disk to the various types of time varying fields for the purpose of improving the braking torque generation of the ECB at low speeds. Unlike the previous FEM, in this chapter, a model that accounts for magnetic phenomena like induction effects and displacement currents is developed.

Herein, a commercial finite element software package, COMSOL Multiphysics[®], is used to carry out the simulations due to the simplicity of the 2-D ECB domain. The created model utilizes quadratic triangular elements and Lagrange interpolation functions, along with the boundary conditions and material properties. The resulting problem is solved using unsymmetric multifrontal method, which is an efficient direct solver for non-symmetric geometries. The braking torque is calculated using the solution of this FEM. In addition, using this model, the optimum braking torque capacity by application of time varying fields of various forms with constant and variable frequencies is determined.

The chapter includes the modeling of an electromagnetic FEM of the proposed ECB with AC field application. An analytical model is then used to validate our FEM for DC field application and then using the analytical model above, FEM is validated for AC field application. The validation results and the braking torque generation with fixed- and variable-frequency time varying field applications in various waveforms are also presented in this chapter along with a discussion section where other means of further improving the braking torque generation are recommended.

3.2 Eddy current brake model

In this section, an accurate electromagnetic FEM of the ECB, which solves for the magnetic flux density when there is an external field (i.e. constant (DC) or time variant (AC)) present, is developed. The FEM is then used to solve for the braking torque under both DC and AC field applications. In terms of AC field analysis for ECBs, no analytical model currently exists in the literature. Thus in order to validate our FEM, the analytical model presented by Lee et al. [29] for the DC field application was used instead. This analytical model [29] is summarized in Appendix 2A.

As mentioned earlier, a commercial FEM software package, COMSOL Multiphysics[®], was used to simulate the eddy current distribution within the ECB. For the problem that is being considered, the governing linear Maxwell's equations are as follows:

$$\mathbf{E} + \mathbf{v} \times \mathbf{B} = \frac{1}{\sigma d} \mathbf{J} \quad (3.1)$$

$$\nabla \times \mathbf{E} = -\frac{\partial \mathbf{B}}{\partial t} \quad (3.2)$$

$$\nabla \times \mathbf{B} = \mu \mathbf{J} + \frac{\partial \mathbf{D}}{\partial t} \quad (3.3)$$

$$\mathbf{D} = \epsilon \mathbf{E} \quad (3.4)$$

where \mathbf{E} is the electric field, \mathbf{D} is the displacement flux density, μ is the magnetic permeability of vacuum, ϵ is the electric permittivity of vacuum, and d is the thickness of the conductive disk.

When the disk rotates, eddy currents are generated on its surface according to the Faraday's law due to the applied external magnetic field. Eq. (3.1) describes the

relationship (i.e. Lorentz law) between the angular velocity of the rotating disk and the eddy currents generated over the surface that is under the magnetic field application. For the basic ECB problem, a 2-D domain shown in Figure 3-1 was selected. The outer circular shape represents the conductor disk and the inner rectangular region is the PPA, the area under the poles of the electromagnet (i.e. the area that the external magnetic field is applied onto). Note that for the given problem, it is assumed that the electromagnetic variables are uniformly distributed over the thickness, i.e. there are no skin effects on the conductor.

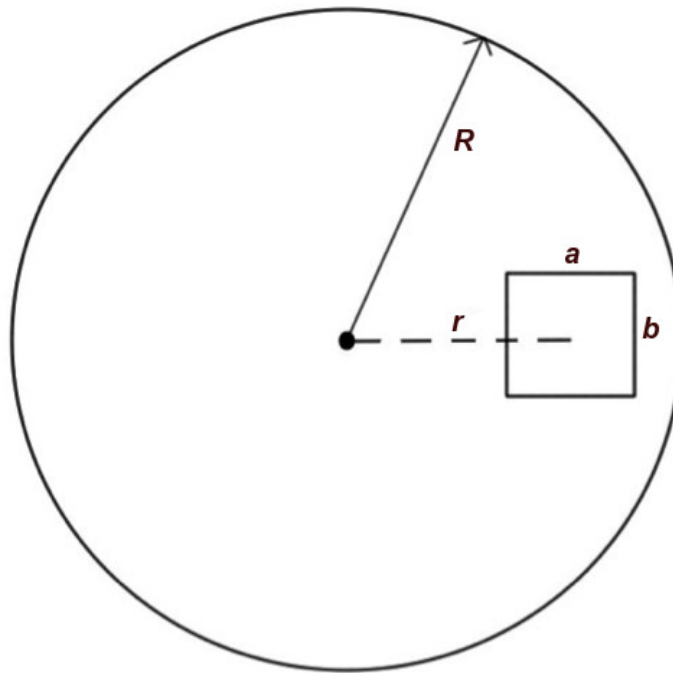


Figure 3-1. Basic ECB domain considered for simulating the eddy current generation

In order to solve for the eddy currents, the governing equations were then transformed into a partial differential equation (PDE). Eq. (3.1) can be rewritten as:

$$\mathbf{E} + \mathbf{v} \times \mathbf{B} = \frac{1}{\mu \sigma d} (\nabla \times \mathbf{B} - \mu \frac{\partial \mathbf{D}}{\partial t}) \quad (3.5)$$

where the current density is defined in terms of the magnetic flux density and the displacement current density using Eq. (3.3). For simplicity, in this equation, the

displacement current density is replaced with the electric field according to Eq. (3.4). Next, the circulation of the vectors on both sides of Eq. (3.5) are taken, i.e.

$$\nabla \times (\mathbf{E} + \mathbf{v} \times \mathbf{B}) = \frac{1}{\mu\sigma d} \nabla \times (\nabla \times \mathbf{B} - \varepsilon\mu \frac{\partial \mathbf{E}}{\partial t}) \quad (3.6)$$

Eq. (3.6) can be simplified using the Faraday's Law, Eq. (3.2) as:

$$-\frac{\partial \mathbf{B}}{\partial t} + \nabla \times (\mathbf{v} \times \mathbf{B}) = \frac{1}{\mu\sigma d} \nabla \times (\nabla \times \mathbf{B}) + \frac{\varepsilon}{\sigma d} \frac{\partial^2 \mathbf{B}}{\partial t^2} \quad (3.7)$$

Above equation is called “the field equation”, since it is only dependent on the magnetic flux density present in the medium. As the driving force of the magnetic flux density, \mathbf{B}_0 is the externally applied flux density.

For the ECB problem, it is assumed that the externally applied field, \mathbf{B}_0 , is uniformly distributed over the PPA, so that the field has no spatial dependence. Therefore, the magnetic flux term that represents the total flux density in Eq. (3.7) is replaced with $\mathbf{B} + \mathbf{B}_0$. Since the curl operator is distributive, Eq. (3.7) can be written as:

$$\begin{aligned} -\frac{\partial(\mathbf{B} + \mathbf{B}_0)}{\partial t} + \nabla \times (\mathbf{v} \times \mathbf{B}) + \nabla \times (\mathbf{v} \times \mathbf{B}_0) &= \frac{1}{\mu\sigma d} \nabla \times (\nabla \times \mathbf{B}) \\ &+ \frac{1}{\mu\sigma d} \nabla \times (\nabla \times \mathbf{B}_0) + \frac{\varepsilon}{\sigma d} \frac{\partial^2(\mathbf{B} + \mathbf{B}_0)}{\partial t^2} \end{aligned} \quad (3.8)$$

The second term on the right hand side of the equation and the last term on the left hand side of the equation are zero since it is assumed that \mathbf{B}_0 is not a function of the spatial coordinates and it is uniformly distributed over the PPA. Note that the applied and induced magnetic fluxes, $\mathbf{B} + \mathbf{B}_0$ and \mathbf{B}_{in} , have only the z components (perpendicular to the surface), while the current density and electric field, \mathbf{J} and \mathbf{E} , have the x and y components. In addition, in the above equation, the first term on the left hand side and the last term on the right hand side of the equation are equal to zero, if no time varying field (i.e. AC) is present.

Under these conditions/assumptions, by rearranging the terms and replacing the vector terms with their magnitudes, Eq. (3.8) can be converted into a PDE in a coefficient form, i.e.

$$-K \frac{\partial B}{\partial t} - k \frac{\partial^2 B}{\partial t^2} + \nabla \cdot \left(\nabla B - \begin{pmatrix} K v_x \\ K v_y \end{pmatrix} B - \begin{pmatrix} K v_x \\ K v_y \end{pmatrix} B_0 \right) = K \frac{\partial B_0}{\partial t} + k \frac{\partial^2 B_0}{\partial t^2} \quad (3.9)$$

where $K = \mu \sigma d$ is the constant mass coefficient, $k = \varepsilon \mu$ is the damping coefficient, and v_x and v_y are the velocities of a point on the rotating conductor disk in the x and y directions, respectively. In the above equation, B and B_0 are the magnitudes of the magnetic flux density and the constant magnetic flux density in the PPA, respectively.

COMSOL Multiphysics[®] was then used to solve the above ECB problem. As the first step, the 2-D domain in Figure 3-1 was created using the geometric ECB design parameters shown in Table 3-1, followed by the assignment of the electrical and magnetic properties of the media in the domain. The domain was then discretized using quadratic triangular elements (6 nodes/element) and Lagrange interpolation functions. After the mesh was created, boundary conditions were defined. For the given problem, the boundary between the conductor disk and the outside environment was described using homogenous *Dirichlet Boundary Condition*. As the final step, considering the non-symmetric and nonlinear nature of the problem, the time-dependent *unsymmetric MultiFrontal method* (UMFPACK), which is a highly efficient direct solver for nonlinear systems, was selected and employed. Finally, the absolute and relative tolerances were set as 0.1 % and 0.001 % for the problem.

Next, the FEM was carried out in order to calculate the magnetic flux density distribution over the defined 2-D ECB domain. Once the flux density distribution is obtained, the corresponding eddy current densities can be calculated in the x and y directions using Eq. (3.3), i.e.

$$\frac{\partial B}{\partial y} = \mu J_x \quad (3.10)$$

$$\frac{\partial B}{\partial x} = \mu J_y \quad (3.11)$$

Note that in order to obtain Eqs. (3.10) and (3.11), it is assumed that the displacement current density is equal to zero. However, this model does not account for the field induced by the eddy currents. When an electromagnet with a permeable ferromagnetic core is used to apply the magnetic field onto the rotating disk, the induced magnetic field cannot be ignored if an accurate analysis required. Due to the induced field, an opposing magnetic flux will be generated within the core, and this flux causes the net magnetic field to decrease. Such a decrease results in less eddy current generation over the surface of the conductor, thus reducing the braking torque.

In order to model the eddy currents more accurately with the consideration of induction effects, an additional (secondary) electromagnetic model was defined and coupled to the primary model in the FEM. The flowchart of our FEM is shown in Figure 3-2. The primary model, the PDE solver, is shown on the left side and the secondary model, the electromagnetic solver, is shown on the right side of the figure. The secondary model uses the same CAD model, mesh and material properties as the primary model; however, the underlying physics, inputs and boundary conditions are all different between the two models. For example, electric insulation (e.g., the normal component of the electric field in the boundary is set to be zero) is used as the boundary condition for the secondary model. In addition, it takes the results of the primary model, i.e. the current density distribution on the disk, as its input and solves for the induced magnetic flux density, i.e. \mathbf{B}_{in} , and the induced current density, i.e. \mathbf{J}_{in} , using the same solution method (UMFPACK). Then, they are subtracted from the applied field and current densities to simulate braking torque (T_{bin}) more accurately, i.e.

$$T_{bin} = \int_S \mathbf{r}_P \times ((\mathbf{J} - \mathbf{J}_{in}) \times (\mathbf{B} + \mathbf{B}_0 - \mathbf{B}_{in})) dx dy \quad (3.12)$$

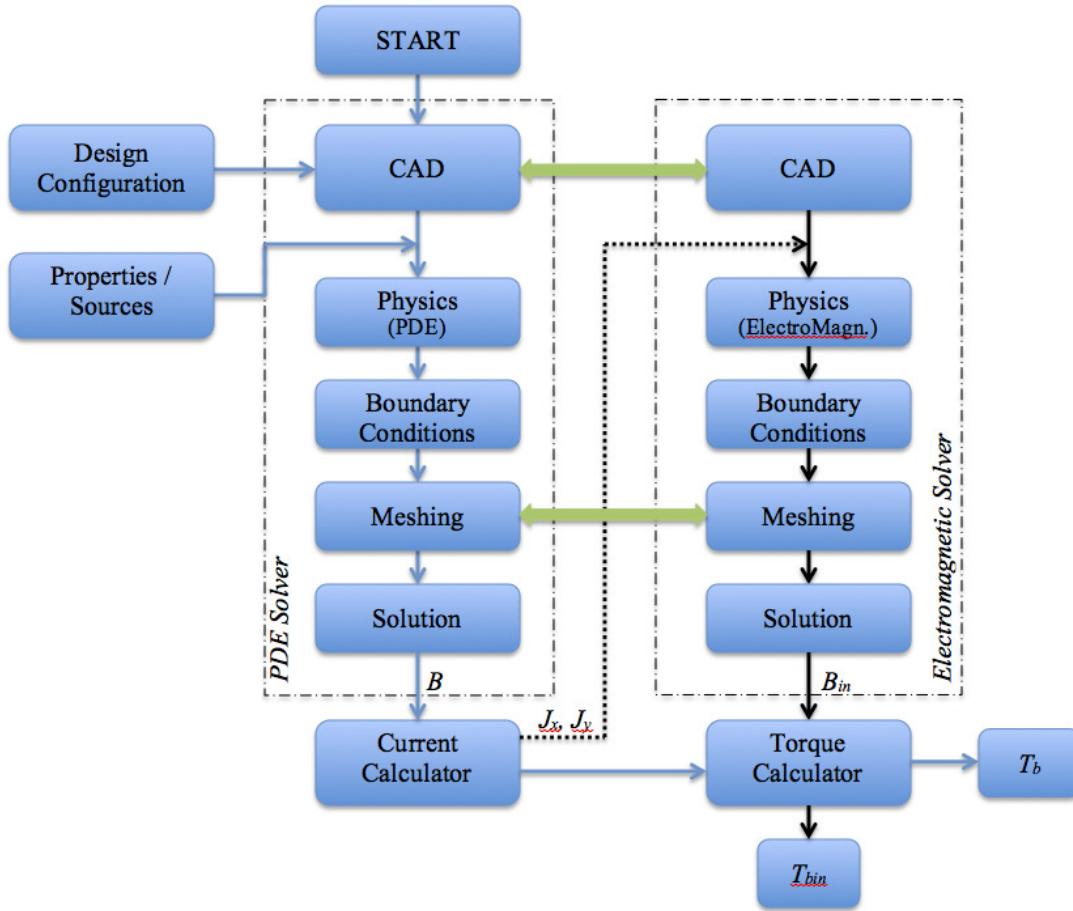


Figure 3-2. Flowchart of the proposed FEM implementation

Note that in Figure 3-2, the blue arrows depict the solution process that is used to solve for the flux distribution without the induction fields. The results then can be used to calculate the braking torque, i.e. T_b , which does not include the induction terms. In order to obtain the braking torque generation with the induction effects, i.e. T_{bin} , the results of the primary model is run through the secondary model and the process is shown using the black arrows.

3.3 Simulation results

In this section, the results obtained using both analytical and FE models are presented. For benchmarking and verification of the proposed FEM, ECB configuration that was studied analytically and experimentally in [29] with DC field application was adapted,

and Table 2-1 shows the specifications of this configuration (note that for simplicity, the specifications of the adapted configuration is also given in Table 3-1). The analytical model of [29] is summarized in Appendix 2A.

Table 3-1. Specifications of the configuration adapted from [29]

Radius of the disk, R (m)	0.05
Width of PPA, a (m)	0.02
Height of PPA, b (m)	0.02
Pole location distance, r (m)	0.0323
Thickness, d (m)	0.003
Material	Aluminum
Conductivity, σ (S/m)	5.79E+07
Externally applied magnetic flux density, B_0 (T)	0.3

First, the analytical model was used to validate the proposed FE model of the ECB for DC field application. Then, using the FEM, the braking torque generation capacity of various time-varying field applications were studied and the frequency specifications of the applied time varying field were optimized on a configuration introduced specifically for automotive applications. Finally, for further improvement in the braking torque generation, the effects of variable frequency field application were studied and the frequency specifications of such fields were optimized on the configuration considered, in order to achieve the maximum braking torque. The results are presented in the corresponding subsections.

3.3.1 Validation of the FEM

In order to validate the FE model, an external magnetic flux density with a magnitude of 0.3 T was applied over a wide range of rotational velocities, 0~1000 rpm. In Figure 3-3, the results obtained for the DC field application from the analytical model and FEM are compared. The curve with the '×' data points shows the results of the FEM and the curve with the diamond data points shows the results of the analytical model. These two curves, which are in good agreement with each other, clearly show the saturation of the braking torque at higher speeds due to the induced field effects. In [29], the analytical results and the corresponding experimental results were in good agreement as well, and thus we can conclude that our FEM is also validated.

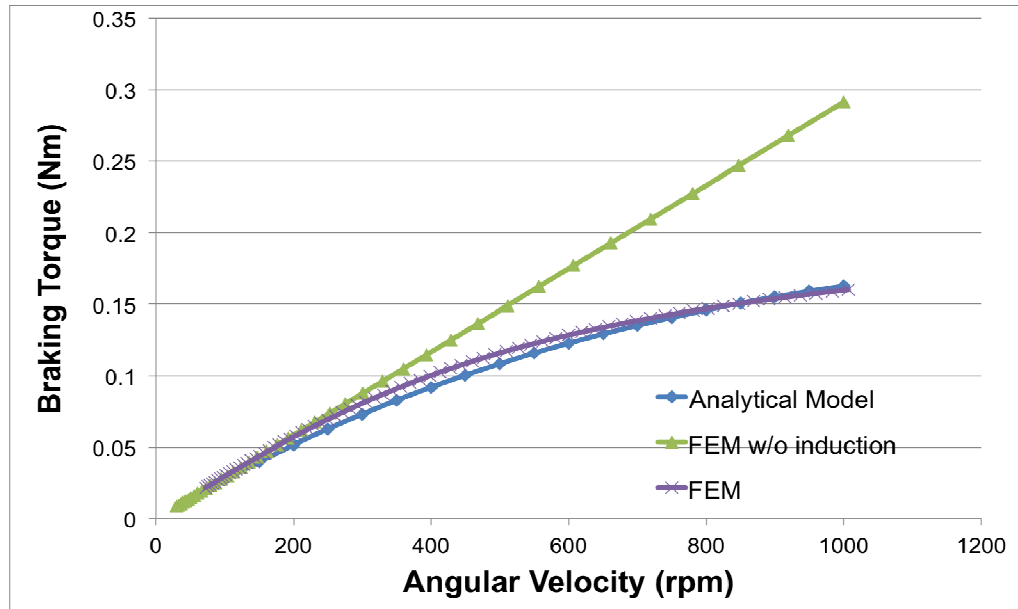


Figure 3-3. Comparison between analytical and FEM results for DC field analysis

In Figure 3-3, the curve with the triangular data points represents the case where the induction effects are assumed negligible. Note that, if permanent magnets or laminated electromagnet core were used as the source of the external applied field, there would be no induction effects due to the electrical properties of the magnets. Due to the flexibility and the structure of the proposed FEM, once the solution is carried out, the results with and without the induction effects can easily be calculated using the results of the secondary and preliminary models shown in Figure 3-2.

The no-induction case results in higher braking torque in the high-speed region. However, if an electromagnet with a soft magnetic core is used instead, there will be a field induced in the core of the electromagnet. This opposing field reduces the capacity of eddy current and braking torque generation in the ECB, resulting in a nonlinear torque-speed relationship similar to the other two curves in Figure 3-3. Note that, in the low speed region, the braking torque capacity of the no-induction case matches that of the induction case – this is due to the fact that the rotational effects are dominant over the induction effects in this low-speed region.

In terms of the validation with AC field application, the model created and described in detail in the previous chapter is used. The details of the model and the assumptions

made to solve the problem were mentioned in the previous chapter. Note that the induction effects are ignored for the AC field validation and a sinusoidal AC field is applied. Two different simulations are carried out. In the first case, the RMS braking torque generation is calculated using the FEM and the analytical model at a constant rotational speed (50 rpm) and the effect of the frequency variation is investigated. For the second case, the frequency of the applied magnetic flux density is kept constant at 10 Hz and the variation of the RMS value of the braking torque generation is plotted with varying angular speeds.

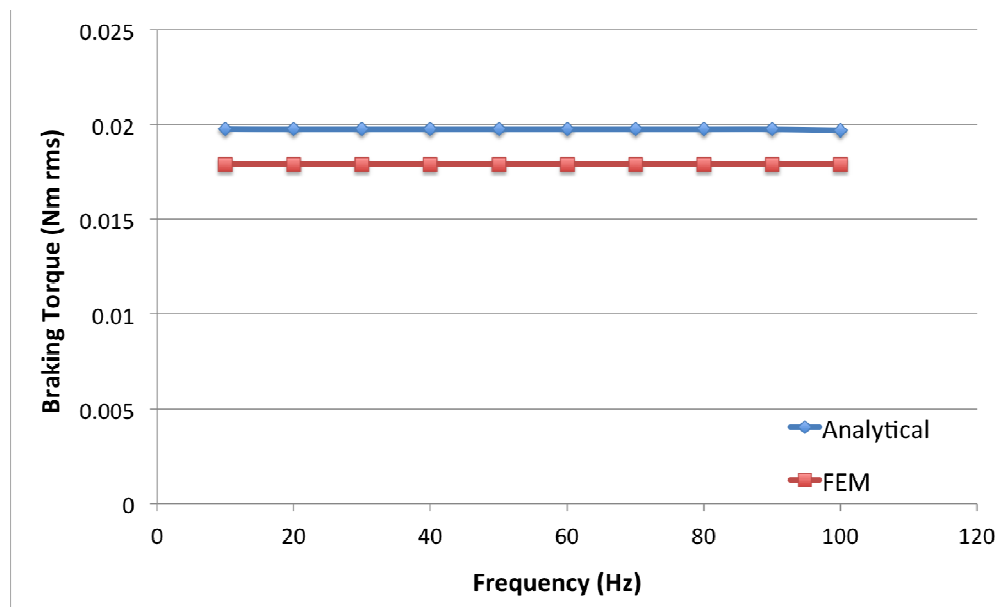


Figure 3-4. Braking torque versus frequency at 50 rpm

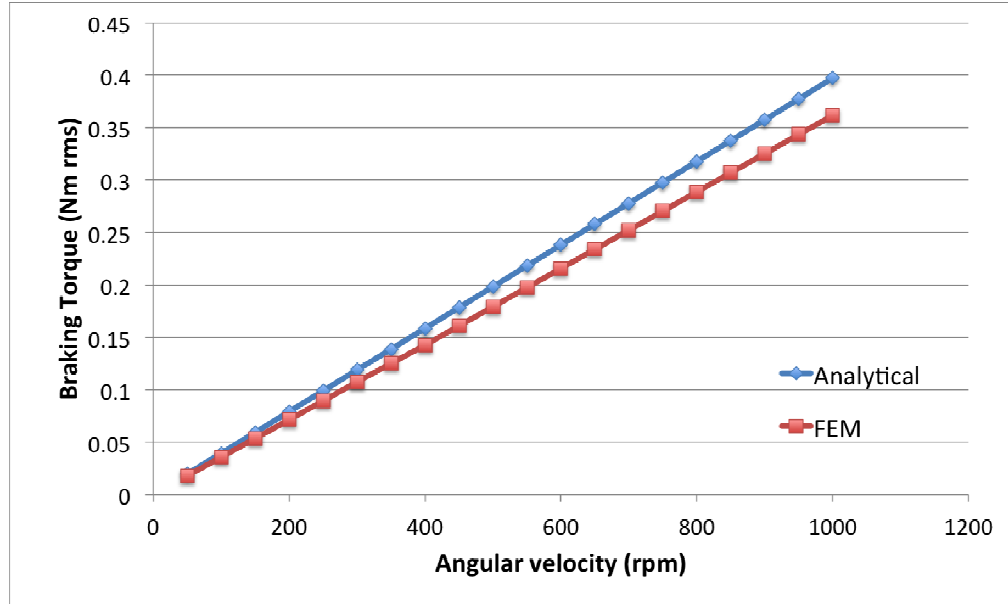


Figure 3-5. Braking torque versus rotational velocity at 10 Hz

For both figures, it can be concluded that the trend of the variation in results with increasing frequencies and increasing angular velocities are same for both analytical and FE model simulations. In addition, the error between these curves is less than 10% at any frequency or any angular velocity and thus it can be concluded that the results of analytical model and FEM are in good agreement. Note that the reasoning behind the difference and the nature of the variations in Figure 3-4 and Figure 3-5 are discussed in detail in the discussion section of the previous chapter.

3.3.2 Time varying field application with induction effects

In this section, braking torque generation of ECB under time varying field applications with various waveforms, i.e. sinusoidal, sawtooth, triangular and square, was studied. Note that for proper comparison, the root mean square (RMS) value of the magnitudes of applied flux density is kept at 0.3 T. Setting a constant magnitude ensures a steady energy input for the application of various waveforms, which makes it possible to compare the results of the time varying field applications with those of the DC field application. Also note that the maximum field frequency was set at 100 Hz to keep the computational cost affordable. In addition, since ECB performs poor at low rotational

velocities, the simulations are carried out for rotational velocities ranging from 0 to 100 rpm.

A sinusoidal flux density with a magnitude of 0.4243 T, a square wave with 50% duty cycle and a magnitude of 0.3 T, a sawtooth wave flux density with a magnitude of 0.52 T, and a triangular wave flux density with a magnitude of 0.52 T were applied to the FEM, keeping their RMS value at 0.3 T. In order to model the periodic waveforms, first 10 harmonic frequencies of Fourier expansion for each waveform are used. The simulations results for a range of velocities as well as for different frequencies are shown in Figure 3-6.

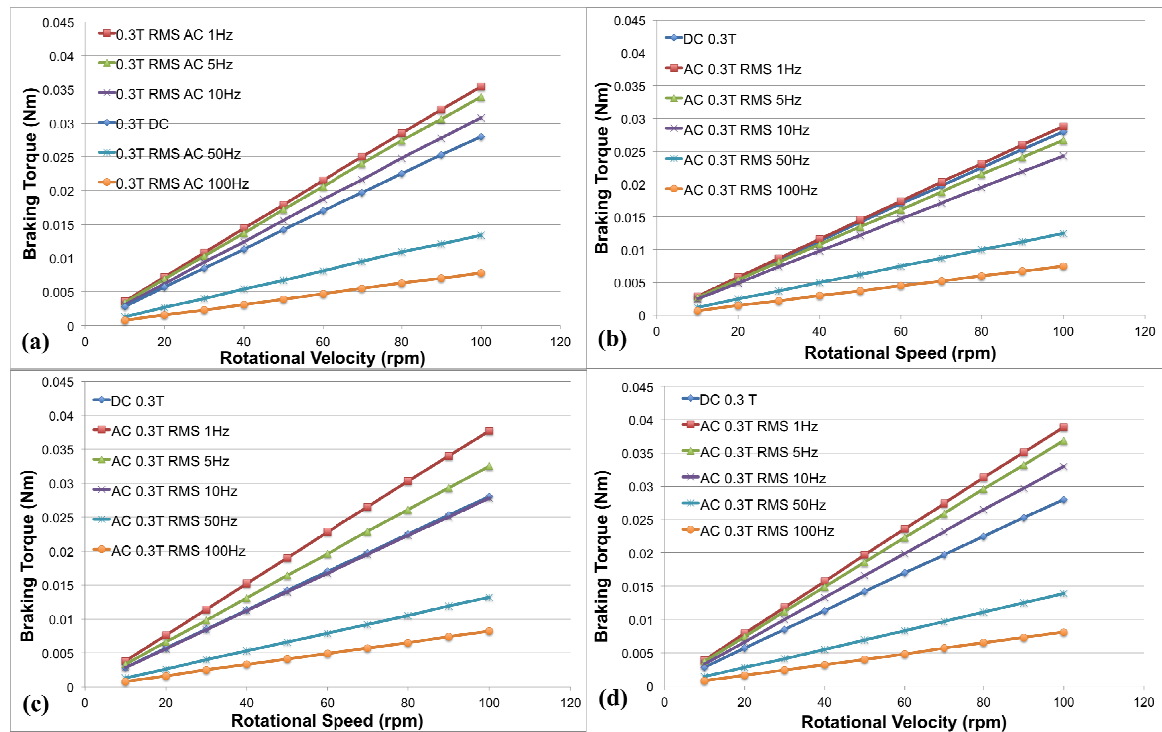


Figure 3-6. Braking torque generation – (a) sinusoidal, (b) square wave, (c) sawtooth wave, and (d) triangular wave field applications

The above results show that the AC braking torque is higher than the DC braking torque at the low frequencies of all four waveforms. However, all four waveforms show a decrease in the braking torque with increasing frequencies. At 100 Hz, for example, the AC braking torque is actually lower than that of the DC counterpart across all velocities and waveforms. At 1 Hz, on the other hand, the break torque increased by 24% with the

sinusoidal field, 3% with the square wave field, 34% with the sawtooth wave field, and 39% with the triangular field application. The relationship between the braking torque and frequency is shown in Figure 3-7. Note that the black dashed line in the figure represents the DC braking torque.

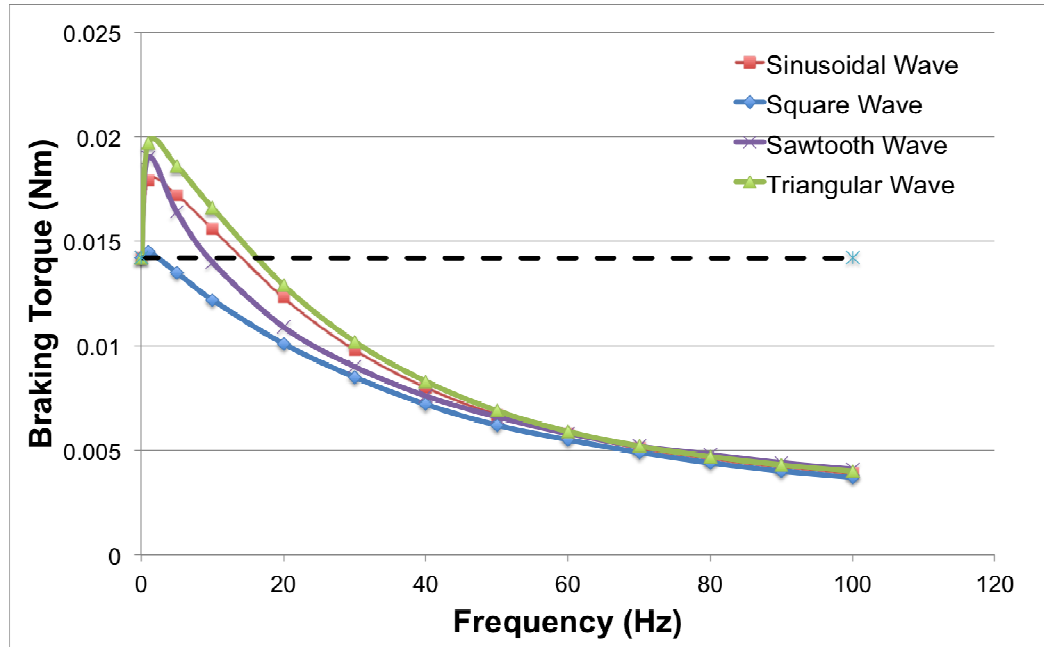


Figure 3-7. Braking torque variation with increasing frequency at 50 rpm with induction effects

Such behaviour of ECB under time varying (AC) field application can be explained by the physics of the eddy currents. They are generated by means of variation in the applied field, either spatial or time dependent. In the cases that we have considered above, the eddy currents were generated by means of the rotation of the conductor as well as the variation in the externally applied field with respect to time. While the rotational velocity of the conductor is kept constant, increasing frequencies will result in higher eddy current generation on the surface of the conductor and induction currents will be generated on the core of the electromagnet. Due to these currents, an induction field is generated in the core opposing the externally applied field. In this specific ECB problem, induction effects will increase with increasing frequencies, causing significant reduction in the braking torque, as described by Eq. (3.12).

In order to improve the braking torque of the ECB with a time varying field, the induction effects must be removed from the system by physically replacing the soft ferromagnetic core with a laminated magnetic core. Note that the simulations in the subsequent sections were carried out without the induction effects. For comparison purposes, the braking torque generation without induction effects was studied for various types of field applications at 50 rpm over a range of frequencies and the results are plotted in Figure 3-8. It is clear from the figure that the braking torque increases with the time varying field application over the frequency range studied, compared to the DC field braking torque presented using the black dashed line in Figure 3-8.

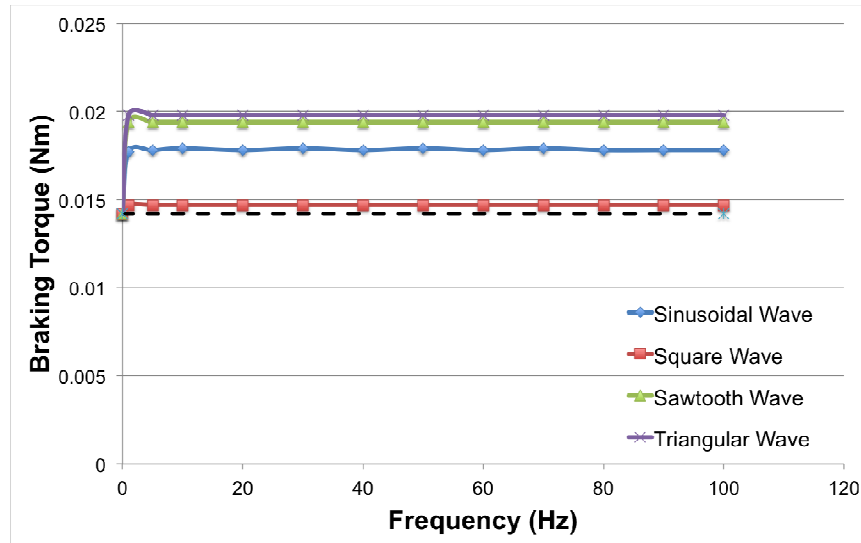


Figure 3-8. Braking torque variation with increasing frequency at 50 rpm without induction effects

3.3.3 ECB configuration for automotive application

The previous results show that the braking torque generation is significantly improved with the application of the time varying field, especially with the triangular wave field application. Herein, an ECB configuration is introduced specifically for automotive applications. The specifications of the selected configuration are given below in Table 3-2. This configuration is applied to all simulations that follow.

Table 3-2. Selected ECB configuration for automotive applications

Radius of the disk, R (mm)	120
Width of the pole, a (mm)	30
Height of the pole, b (mm)	30
Pole location distance, r (mm)	95
Thickness, d (mm)	10

The CAD model of the FEM was updated accordingly for the new configuration, and the sinusoidal and triangular waveforms are used as the input sources individually.

3.3.4 Time varying field application and optimization without induction effects

As the next step, the braking torque generation in the automotive ECB configuration in Table 3-2 is optimized. For the application of a periodic waveform such as sinusoidal or triangular, the frequency is set to be the only design variable and the resulting braking torque was plotted for various frequencies. The optimum frequency that results in the maximum braking torque was then obtained from the plot. Note that the geometry, properties, physics and mesh of the FEM are not changed for the optimization. The solution is obtained by modifying the input source term, which is a function of the frequency, and is updated at each iteration. The FEM does not require significant computational effort to obtain a result for a selected input source waveform at a particular frequency.

The resulting ECB optimization problem does not have any constraints. However, the solution has to account for the skin effects due to the application of alternating flux densities. When an AC is applied to the surface of a conductor, the generated eddy current has a tendency to accumulate in the vicinity of the surface. Thus, the current density decreases with increasing depth into the material, and it diminishes after a certain depth, which is known as the skin depth. The skin depth (d_{skin}) can be expressed in terms of the material properties and the frequency of the time varying current applied, i.e.

$$d_{skin} = \sqrt{\frac{\rho_{res}}{\pi f \mu}} \quad (3.13)$$

where ρ_{res} is the resistivity and μ is the absolute magnetic permeability of the conductor, and f is the frequency of the current applied on the conductor surface. As the proposed

FEM does not account for the skin effects, the thickness value given in Table 3-2 is corrected, if the skin depth is less than half of the thickness. In such a case, the corrected thickness value (i.e. d_{corr}) is set to be twice the skin depth and the simulations are carried out using this updated value.

From previous results in Sec. 3.3.2, triangular wave field application gives the highest braking torque values among various waveforms. Thus, here the frequencies of the triangular field and the sinusoidal field, which the latter is served as a reference, are optimized for higher braking torque generation. For the optimization problem, the design space for the frequency of the applied field is defined between 1 Hz and 100 Hz.

Solving the optimization problem, it is found that the optimum frequency for both triangular and sinusoidal field application is around 10 Hz. The braking torque generations of the ECB configuration at 10 Hz are shown in Figure 3-9 for both field applications.

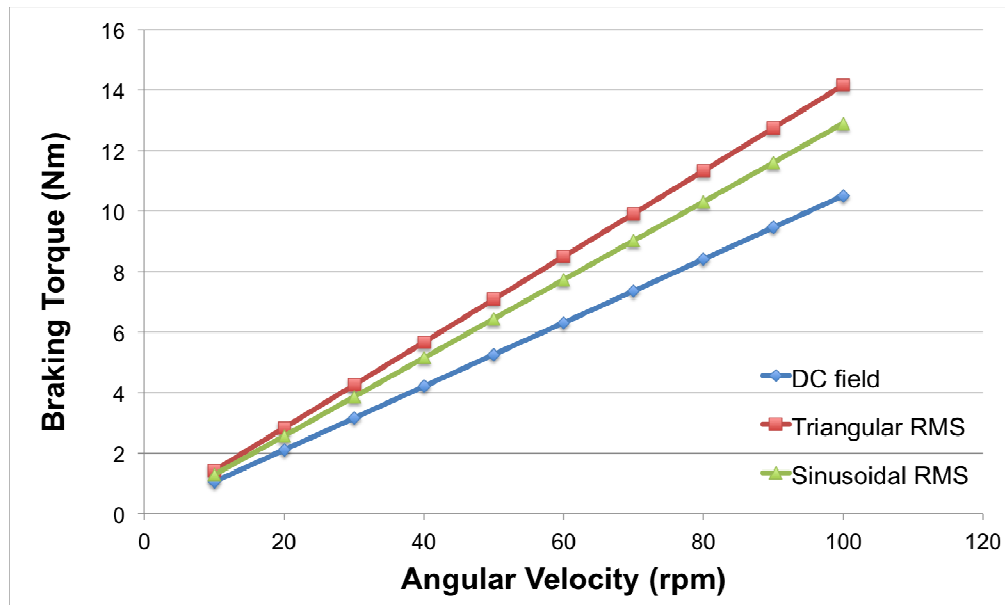


Figure 3-9. Braking torque generation at 10 Hz for triangular, sinusoidal and DC field applications

According to the results, with the DC field application, the ECB configuration of Table 3-2 can generate 10.51 Nm at 100 rpm. However, the braking torque is increased by

22.5% with the application of the sinusoidal field at 10 Hz and 34.5% with the application of the triangular wave field at 10 Hz.

3.3.5 Effects of frequency modulation on braking torque generation

In this section, it is proposed that the braking torque can be increased further with the application of a field with variable frequency onto the conductor disk. The variation of frequency of the time varying field can be defined using the frequency modulation (FM). FM is commonly used in telecommunication and signal processing to convey information over a carrier wave by varying the instantaneous frequency of the signal. Here, the same theory is used to define a sinusoidal field that has varying instantaneous frequencies. The FM can be implemented as:

$$f_1 = \Delta f \sin(2\pi f_2 t) \quad (3.14)$$

$$B = B_0 \sin(2\pi f_1 t) \quad (3.15)$$

where t is time, f_1 is the carrier frequency, i.e. the frequency of the applied time varying field, B_0 is the peak magnitude of the applied field, f_2 is the modulation frequency and Δf is the frequency deviation. Once the above equations are rearranged, the modulated sinusoidal field equation becomes:

$$B = B_0 \sin\left(2\pi f_1 t - \frac{\Delta f}{f_2} \cos(2\pi f_2 t)\right) \quad (3.16)$$

Note that in order to obtain Eq. (3.16), the frequency variation has to be transformed into angular variation; since in reality the modulation occurs through the angular variation, not frequency.

In terms of ECB braking performance, a sinusoidal wave and a triangular wave are applied individually with variable frequencies to study the improvements via FM. For comparison purposes, it is assumed that the RMS magnitude of the applied flux densities is equal to 0.707 T (peak magnitude of 1 T for sinusoidal and 1.225 for triangular wave). The carrier frequency, frequency deviation and the modulation frequency are then optimized for higher braking torque using a gradient free genetic algorithm (GA). For the

given problem, a tolerance value is defined in order to terminate the optimization. Although stochastic methods such as GA are powerful optimization algorithms, they are not guaranteed to converge to the global optimum. However, by running the algorithm multiple times for the same ECB problem, an improved accuracy is obtained in terms of the optimum frequency. The proposed optimization problem is given as follows:

$$\text{Maximize: } T_b = \int_S \mathbf{r}_M \times (\mathbf{J} \times (\mathbf{B} + \mathbf{B}_0)) dx dy \quad (3.17)$$

$$\text{Correction: } d_{eff} = \min \{2d_{skin}, d\} \quad (3.18)$$

where d_{eff} is the corrected thickness value by accounting for the skin effects. Similar to the periodical wave optimization mentioned earlier in Sec 3.4, the skin effects are accounted for using the relation given in Eq. (3.18).

The optimization results show that the sinusoidal field application results in the maximum braking torque when carrier frequency, modulation frequency and frequency deviation are equal to 52, 52 and 51 Hz, respectively. On the other hand, triangular wave application results in the maximum braking torque when the frequencies are 39, 39 and 38 Hz, respectively. These results are shown in Figure 3-10.

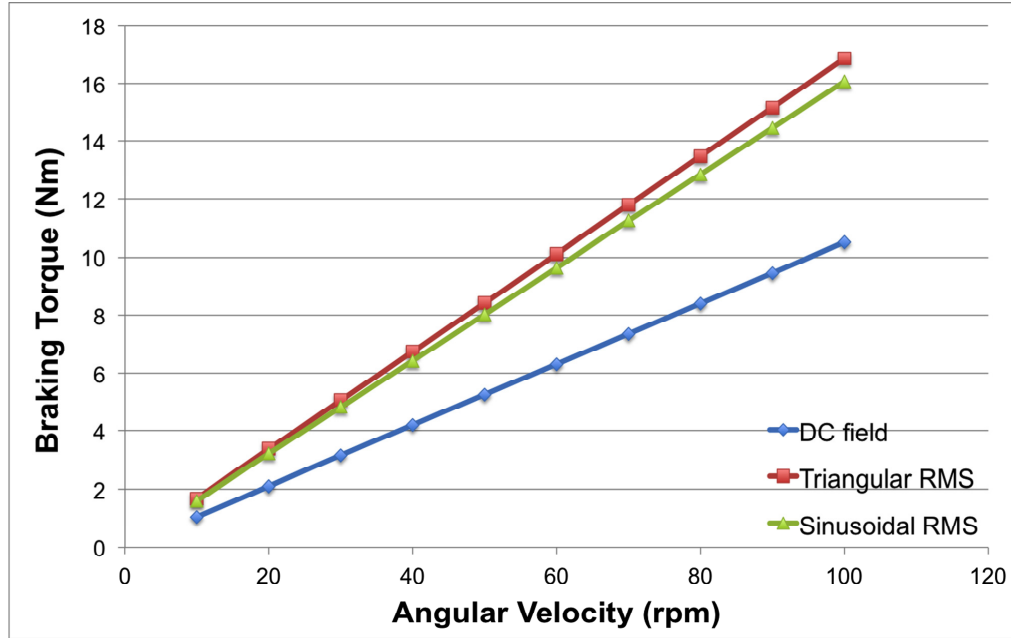


Figure 3-10. Optimum braking torque generation with frequency modulation

According to the results, the braking torque is increased by 52.8% with the application of sinusoidal field via FM and over 60% with the application of triangular field via FM, reaching a maximum value of 16.85 Nm at 100 rpm (in comparison to only 10.51 Nm with the application of the DC field).

3.4 Discussion

Although ECBs have a number of performance advantages over CHBs, braking torque generation at low speeds is considerably low. In this chapter, in order to improve the braking performance of the ECB, the potential of the time varying (AC) field application was studied. A FEM, which was verified with the analytical DC model and experimental results in the literature, was used to investigate the variation in the braking torque with time varied field application.

In addition to the mesh dependent analysis carried out here, there are various FE techniques that offer promising improvements in accuracy and computation time over the traditional mesh based algorithms for specific problems. Mesh free algorithms, e.g., smoothed finite element method (S-FEM) [40-47] and isogeometric FE analyses [48-50], are examples of such numerical methods. These algorithms may result in higher accuracy

and faster computation times for the ECB problem studied. However, due to the relatively simplistic geometric configuration of our ECB problem and readily available solution methods for traditional mesh dependent algorithms, a mesh based FEM was adopted and used to study the braking torque generation for the given ECB configuration.

The results of the numerical analysis for different waveform applications were presented in Sec. 3.3. Note that the braking torque generated with DC field application was used as the reference for the cases studied above. There are three main conclusions that can be drawn from the results obtained. First conclusion is that the braking performance of the ECB strongly depends on the nature of the externally applied flux density.

In this numerical study, the braking torque generation with sinusoidal, square, sawtooth and triangular wave applications was investigated. In all cases, a higher braking torque was obtained at very-low frequencies, in comparison to the DC field case. Faraday's law of induction explains this behaviour. It states that when there exists a time varying magnetic flux, an electric field that is proportional to the rate of change of the flux will be generated. Having this additional electric field term results in variation in eddy current generation on the surface of the conductor. Thus, the braking torque will also vary according to the rate of change of the applied field.

Among all applied waveforms, the triangular wave has the highest and steadiest rate of change and, as it was expected, the results in Figure 3-7 showed that the braking torque increased the most. Thus it is concluded that for various waveforms applied at the same frequency, the time rate of change of the wave defines the amount of the braking torque generation of ECB. In the case of the square wave application, the torque variation is not significant, mainly because of the similar shape of the square wave to the DC field. In the square wave, the variation occurs only at the instants when the magnitude changes the sign, from negative to positive or vice versa. Since the variation is significantly limited, the results are almost identical with the DC field braking torque generation.

Second conclusion that can be drawn is that the braking torque can be significantly increased with the application of time varying magnetic flux at low frequencies. Sinusoidal, sawtooth and triangular wave applications result in an average of 24%, 34% and 39% increase at 1 Hz over that of the DC application, respectively. The increase in

the braking torque can be explained with the generation of additional eddy currents on the surface. At 5 Hz, the braking torque increases by 21% with sinusoidal wave, 16% with sawtooth wave and 31% with triangular wave application.

Finally, from the results presented in the figures in Sec. 3.3, it can be concluded that with increasing frequencies, the braking torque decreases in all waveforms. This behaviour can be explained with the induction effects. As the frequency increases, the eddy currents generated due to the time variation increase dramatically, but with this increase, the induction currents generated on the surface of the electromagnet core also increase and they result in an opposing field that reduces the applied field. Therefore, the amount of the braking torque decreases as a result. The variation of the braking torque with respect to the frequency at a constant rotational speed of 50 rpm for all waveforms applied was shown in Figure 3-7.

In terms of the practicality, it is not ideal to have reduction in the braking torque with increasing frequencies. Hence, for further increase in the braking torque generation, the induction effects need to be removed by replacing the soft ferromagnetic core of the electromagnet with a laminated one. The same plots presented in Figure 3-7 were redrawn for the case without the induction effects in Figure 3-8. Comparing these two figures, at low frequencies, the induction effects are negligible and the max braking torque achieved with the induction effects are comparable to the braking torque generated without the induction effects at 1 Hz. Also, Figure 3-8 showed that the braking torque is almost constant within the frequency domain investigated. However, the detailed data shows that there exists an optimum frequency for each applied field where the braking torque is the maximum.

In order to find the optimum frequency, an optimization algorithm was run on an ECB configuration specific for automotive applications. Note that the optimization was only carried out for triangular and sinusoidal field applications, since the triangular field application resulted in the highest braking torque and the sinusoidal field serves as the reference waveform. When DC field is applied, this configuration generates 10.51 Nm. It was shown in Sec. 3.3.4 that the braking torque reaches a maximum of 12.9 Nm with the sinusoidal field application and a maximum of 14.2 Nm with the triangular field application at 10 Hz and 100 rpm.

Previously in [28], the braking torque generation of an ECB model with 3 PPAs was studied. Unlike current study, this work only focused on sinusoidal field application and the numerical results showed that the braking torque increased by 13.6% at an optimum frequency of 40 Hz. In this chapter, however, it is shown that even with 1 PPA, the braking torque can be increased 22.5% with sinusoidal field and 34.5% with triangular field application at an optimum frequency of 10 Hz.

Finally, it is proposed that the braking torque can be increased further by application of an AC field with varying frequency. This results in an increase in the eddy current generation and the braking torque increases accordingly due to the rise in the eddy current density. To model the varying frequency, FM (frequency modulation) is used and the braking torque is optimized on the considered ECB configuration for the sinusoidal and triangular field applications. The sinusoidal field application with FM reaches a maximum braking torque of 16 Nm when the carrier frequency, modulation frequency and frequency deviation are equal to 52 Hz, 52 Hz and 51 Hz, respectively. Compared to the DC field results, the braking torque increased by around 53%, and compared to the braking torque generated by the sinusoidal field application with a constant carrier frequency (i.e. no FM) of 10 Hz, the torque increased by 24.5%.

Triangular field application with FM reaches a maximum braking torque of 16.85 Nm when the carrier frequency, modulation frequency and frequency deviation are equal to 39 Hz, 39 Hz and 38 Hz, respectively. Compared to the DC field torque generation results, the increase was around 60% and compared to the braking torque generated by the triangular field application with a constant carrier frequency of 10 Hz, the increase was around 19%.

All in all, as it was originally proposed, the application of time varying field resulted in the increase in the braking torque capacity for ECBs and the braking torque increases significantly not only at low speeds but also at high speeds. Moreover, the braking torque of an ECB can significantly be increased with the application of a time varying field (the triangular field in particular) with a variable frequency component. According to the numerical results obtained, the ECB configuration considered can generate 60% more braking torque with the application of FM triangular wave field than the DC field application.

Further improvements can also be achieved in various ways. Note that the simulations were carried out based on the ECB configuration presented in Table 3-2, which was not optimized for a specific automotive application that may introduce other dimensional and material design variables. In addition to above design optimization, there is a combination of approaches that can be taken in order to improve the braking performance of the ECB: (i) increasing the magnitude of the applied field, (ii) increasing the number and area of PPAs on the conductor surface (e.g., see Figure 3-11 where yellow areas are the PPAs) and/or (iii) increasing the rotational speed of the conductive brake disk using gears. All these approaches result in increased eddy current generation over the surface of the conductive brake disk, which leads to a higher braking torque. In particular, having an array of PPAs on the surface can drastically improve the braking performance. For example, a smooth but effective braking can be obtained with the introduction of a phase difference between the applied flux density of each PPA. Moreover, the relative positions of the PPAs, the shape and polarity of the applied fields, and the frequency and phase angles between each field must be optimized to obtain the maximum braking in both low and high-speed regions.

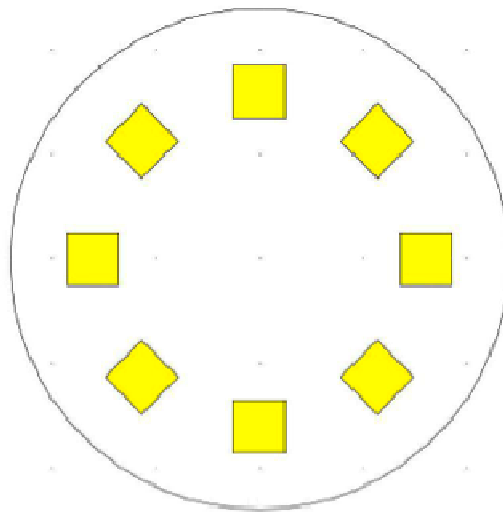


Figure 3-11. Conductor brake disk with an array of PPAs

With the proposed modifications, further improvement in the braking torque generation of the ECB can be achieved. Although ECB may be able generate enough braking torque to stop the vehicle with the proposed improvements, due to its nature of

consuming power to keep the vehicle parked after braking, ECB requires an assistive braking system for parking.

3.5 Conclusion

In this chapter, Eddy Current Brakes (ECBs) are proposed as possible substitutes for the conventional hydraulic brakes (CHBs) in automotive applications due to its unique potential for performance advantages (e.g., non-contact and fast response). As a potential solution for the limited braking torque of typical ECBs at low speeds, the application of time varying fields (i.e. AC) is proposed. A finite element model (FEM) that accounts for the effects of time varying fields on the performance of the ECB was developed, which was then validated using an existing analytical model for the DC field. It was shown that improved braking performance can be obtained when AC fields are used at both low and high velocities. Time varying fields in different waveforms (i.e. sinusoidal, square, sawtooth and triangular waves) were applied and triangular wave field application resulted in the highest braking torque. The numerical results also showed that the braking torque decreases with increasing braking torque due to induction effects when the time varying fields are applied. In order to increase the braking torque generation, the induction effects were eliminated and braking torque generation was maximized for sinusoidal and triangular field applications on a generic ECB configuration for automotive applications. A further improvement was subsequently proposed by application of frequency modulated (FM) AC fields. The results showed that a 60% increase in the braking torque can be achieved with the FM compared to the DC field braking. Further improvements in braking torque generation of the ECB can be achieved by means of increasing the magnitude of applied field, the number of PPAs and the rotational speed of the conductor disk using gears.

Appendix.3A. Analytical Model: DC field application

The DC model proposed by Lee et al. [29] uses the Lorentz force law in order to explain the eddy current generation under DC field application. When a moving charged particle enters a region in which a magnetic field is present, a force, whose magnitude and

direction depend on the magnitude and the direction of the particle velocity and the external magnetic field, is exerted on the particle. If a conductor disk rotates under applied magnetic field, charged particles, electrons and protons that are initially in balance over the surface of the conductor, will be separated from each other by the Lorentz force. This separation results in the generation of surface charge densities over the PPA. Using the surface charge densities, corresponding electric field and current densities in the PPA can be calculated.

Following the work of Lee and Park [29], it is initially assumed that the disk has infinite radius initially and the model is solved for the electric field and the eddy current density according to this assumption. Then, the radial component of the eddy current density within the conductor disk at the boundary was set to zero by introducing an imaginary current source outside the disk. By doing this, the model effectively represents a conductor disk of a finite radius. As the final step, this model utilizes the magnetic Reynolds number in order to solve for the induced magnetic field that is generated by the eddy currents on the conductor. The magnetic Reynolds number is the ratio between the induced field and the applied field. With the induced field computed, the torque that opposes the rotation of the disk can be calculated using the following relationship:

$$T_b = \int_S \mathbf{r}_P \times (\mathbf{J} \times (\mathbf{B} - \mathbf{B}_{in})) dx dy \quad (\text{A3.1})$$

4. OPTIMIZATION OF BRAKING TORQUE GENERATION CAPACITY OF EDDY CURRENT BRAKES WITH THE APPLICATION OF TIME VARYING MAGNETIC FIELDS

4.1 Introduction

ECBs can readily be found in the following applications by means of assistive braking: to slow down a high inertia actuator, to help braking of heavy vehicles such as trains and heavy trailers, to adjust the stiffness of exercise equipment (e.g., exercise bikes), etc. Especially, slowing high-speed trains down to speeds where conventional brakes would be more efficient is one of the key applications of ECBs [12-16].

Potential performance improvements, e.g., contactless braking, silent operation, no friction, natural capacity to imitate an ABS, etc., make ECB a very attractive alternative for CHBs. However, the main problem of the existing ECB is the limited braking torque generation at low vehicle speeds and in order to be able to realize a stand-alone ECB, this problem needs to be addressed.

In this thesis, use of AC fields is proposed to improve the braking torque generation. In Chapter 2, an analytical model was created and preliminary results obtained showed that the braking torque generation increases with the application of AC fields not only at low velocities but also high speeds. In Chapter 3, an accurate FEM, which was validated using 2 analytical methods for both AC and DC field applications, was created. Using this FEM, various forms of time varying fields applied with and without frequency modulation were applied and the results showed that the braking torque significantly increases with the application of AC field in the form of triangular waves with frequency modulation.

In order to effectively deal with the problem of reduced braking torque at low speeds, all the factors (geometric, material, field dependent and position dependent variables) that affect the braking torque generation are identified. In this chapter, the main objective of is to optimize the braking torque generation of ECBs for configurations that consist of up to 4 PPAs with the help of an accurate electromagnetic FEM that analyzes and simulates the eddy current generation under various forms of time varying field applications with

variable frequencies. The optimization procedure is carried out to validate a stand-alone ECB configuration that can generate sufficient amount of braking torque to stop a vehicle.

Due to the nature of the nonlinearity of the problem, a stochastic optimization algorithm, Genetic Algorithm (GA), is used. Stochastic algorithms do not require gradient information and this makes such algorithms very attractive for solving the highly nonlinear ECB optimization problem. GA searches a vast design space very fast and efficiently with the help of evolution algorithm it employs. The previous successful design configurations are used to create the next design configuration. Thus, it can be said that the evolution algorithm used is the biggest advantage of such a technique. However at the same time, same evolution algorithm is the biggest disadvantage, since evolution does not guarantee the best answer, GA; similar to any other stochastic algorithm, is not guaranteed to find the global optimum.

In this chapter, the FEM created and described in the previous chapter is briefly described and the braking torque generation results obtained for various waveforms are briefly presented in this chapter since they are going to give the reasoning behind the configuration selected to be optimized. Then, the optimization problem is defined for the ECB problem along with the geometric constraints and comfort constraint. Since the braking torque is alternating due to the application of the alternating fields, the comfort levels become important in the process of braking. The variation in deceleration is converted in a quantitative comfort value and these values are kept smaller than a threshold value. Once the optimization is carried out, the results show that the braking torque significantly increases with the additional PPAs and braking torque generation of an optimum configuration with 4 PPA can exceed the braking torques generated by a conventional hydraulic brake.

4.2 Eddy current brake model

In previous work [32], an accurate electromagnetic FEM of the ECB, which solves for the magnetic flux density when there is a time varying external field is present, was presented. Using the governing Maxwell's equations, the partial differential equation (PDE) shown in Eq. (4.1) was obtained. Also, note that the PDE is only magnetic flux dependent.

$$\begin{aligned}
& -\frac{\partial(\mathbf{B} + \mathbf{B}_0)}{\partial t} + \nabla \times (\mathbf{v} \times \mathbf{B}) + \nabla \times (\mathbf{v} \times \mathbf{B}_0) \\
& = \frac{1}{\mu_0 \sigma d} \nabla \times (\nabla \times \mathbf{B}) + \frac{1}{\mu_0 \sigma d} \nabla \times (\nabla \times \mathbf{B}_0) + \frac{\varepsilon_0}{\sigma d} \frac{\partial^2 (\mathbf{B} + \mathbf{B}_0)}{\partial t^2}
\end{aligned} \tag{4.1}$$

where \mathbf{J} is the net eddy current density, \mathbf{B} is the external magnetic field applied, \mathbf{B}_0 is the externally applied flux density, \mathbf{E} is the electric field, \mathbf{D} is the displacement flux density, μ_0 is the magnetic permeability of vacuum, ε_0 is the electric permittivity of vacuum, d is the thickness of the conductive disk and t is time.

For the basic ECB problem, a 2-D domain shown in Figure 4-1 was selected. The outer circular shape represents the conductor disk and the inner rectangular region is the PPA, the area under the poles of the electromagnet, i.e. the area that the external magnetic field is applied onto. Note that for the specific problem, it is assumed that the electromagnetic variables are uniformly distributed over the thickness, i.e. no skin effects on the conductor.

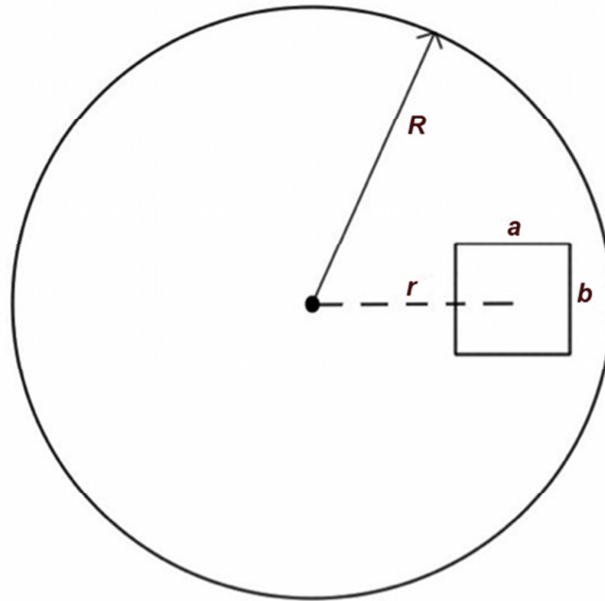


Figure 4-1. Basic ECB domain considered for simulating the eddy current generation

By using the PDE solver module of the COMSOL Multiphysics[®], the magnetic flux density distribution can then be solved over the rotating conductive disk surface with the

help of proper boundary conditions; and by using the magnetic flux density distribution, the eddy current densities can be calculated. In order to account for the secondary field induced by the eddy currents, an additional (secondary) model was defined and coupled to the primary model. The secondary model takes the results of the primary model, i.e. the current density distribution on the disk, as its input and solves for the induced magnetic flux density, \mathbf{B}_{in} . Then, the braking torque, T_b , is calculated as follows:

$$T_{bin} = \int_S \mathbf{r}_P \times ((\mathbf{J} - \mathbf{J}_{in}) \times (\mathbf{B} + \mathbf{B}_0 - \mathbf{B}_{in})) dx dy \quad (4.2)$$

where \mathbf{r}_P is the position vector that is a function of x and y coordinates, and \mathbf{J}_{in} is the induced current density. The flowchart of the FEM is shown in Figure 4-2. FEM contains two solvers, one is the PDE solver that solves the eddy current distribution and the other is an electromagnetic solver that introduces the effects of induction fields.

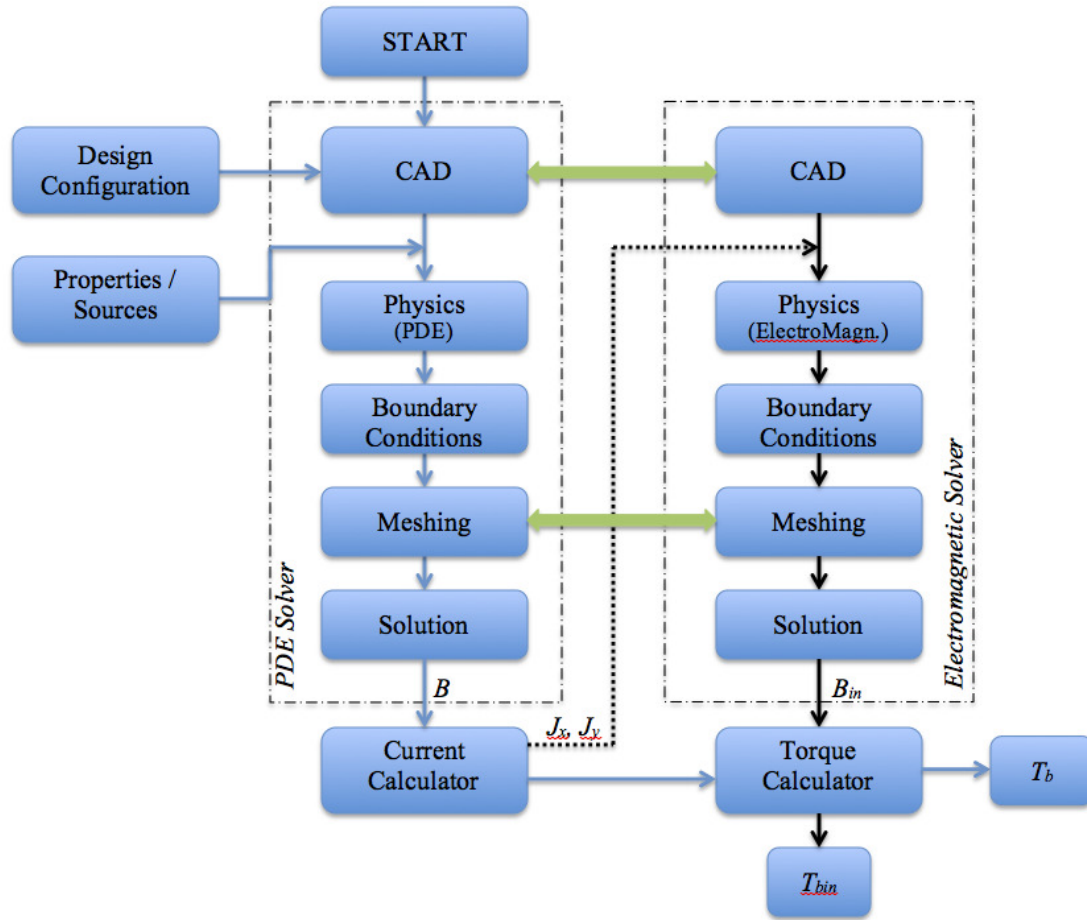


Figure 4-2. Flowchart of the FEM implementation

In the same work published previously [32], braking torque generation of ECB under time varying field applications with various waveforms (i.e. sinusoidal, sawtooth, triangular and square) was studied. The results showed that the induction has a significant effect as the frequencies increase. Therefore, it was recommended that laminated cores be used to remove the induction fields. Among those studied waveforms, triangular field resulted in the highest braking torque generation. In addition, frequency modulated field application was proposed for further increase in the braking torque generation.

As a result of the preliminary analysis in [32], in the following sections, the braking torque was optimized for a configuration where the induction fields are removed by utilizing a laminated core electromagnet and where frequency modulated external magnetic field is applied. Thus, from the simulation point of view, the induction effects that are solved using the electromagnetic solver in Figure 4-2 are removed from the FEM

of ECB. Triangular waveforms are used to find the optimum ECB configuration since they result in highest braking torque when they are applied on the rotating conductive disk. In addition, sinusoidal fields are also studied and optimum ECB configurations are found, since they are the main building blocks of any waveforms.

4.3 Optimization

4.4.1 Definition of the problem

In this section, the optimization problem for the ECB is defined and the above FEM is used to solve for the braking torque of the given configuration in Table 1 and applied flux density. In setting up the optimization problem, an objective function was defined with the braking torque as a function of both the geometry dependent and the applied field dependent design variables. The optimization problem of ECB is given in Eq. (4.3). The braking torque (T_b) is maximized and the problem is subject to a number of constraints mentioned in detail below.

$$\text{Maximize: } T_b = \int_S \mathbf{r}_M \times ((\mathbf{J}) \times (\mathbf{B} + \mathbf{B}_0)) dx dy \quad (4.3.a)$$

$$\text{Subject to: } d_{eff} = \min \left\{ 2 \sqrt{\frac{\rho}{\pi f_1 \mu}}, d \right\} \quad (4.3.b)$$

$$comfort \leq 0.5 \frac{m}{s^2} (RMS) \quad (4.3.c)$$

$$R \geq \sqrt{(r * \cos(\alpha) + \frac{a}{2})^2 + (r * \sin(\alpha) + \frac{b}{2})^2} \quad (4.3.d)$$

$$r \sin(\alpha) \geq b \quad (4.3.e)$$

$$f_1 \geq \Delta f - 1 \quad (4.3.f)$$

The design variables are defined and listed in Table 4-1 for the specific ECB optimization problem considered. Also note that the optimization was carried out at applied magnetic flux densities of 1 T and 1.225 T for the sinusoidal and triangular field application, respectively. These magnitudes satisfy a constant magnetic energy input into the system that makes the results of the two optimizations comparable, as the RMS values of these two input fields are both 0.707 T.

Table 4-1. Design Variables and Constants for the ECB optimization problem

<i>Design Variables (d)</i>	<i>Lower Boundary</i>	<i>Upper Boundary</i>
Radius of the disk, R (m)	0.05	0.12
Thickness of the disk, d (m)	0.003	0.01
PPA width, a (m)	0.02	0.05
PPA height, b (m)	0.02	0.05
Pole location distance, r (m)	0	0.11
Position of PPAs, α_n (rad)	0	π
Carrier Frequency, f_1 (Hz)	1	400
Modulation Frequency, f_2 (Hz)	1	400
Frequency Deviation, Δf (Hz)	0	399
Phase angle between fields at PPAs, β_n (rad)	0	2π
Tire Diameter (m)	0.62	
Loaded Vehicle Mass (kg)	1300	
Applied Flux Density – Peak Magnitude (T)	1 (Sinusoidal), 1.225 (Triangular)	
Rotational Velocity (rad/s (rpm))	10.472 (100)	

With the introduction of multiple PPAs, the relative position (i.e. the geometric angle) of the PPAs and the relative phase difference (i.e. the phase angle) between the flux densities applied to each individual PPA are taken into account by means of α_n and β_n (i.e. $n = 1, 2$ and 3), respectively. The subscript “ n ” represents a PPA’s coupling with a reference PPA. For example, in the case of the 2-PPA configuration, n is set to be 1. One of the PPAs is defined as the reference, thus only α_1 and β_1 are defined as the angle between the PPAs and phase angle between the applied flux densities to the PPAs. For the 4 PPA configuration, n is set to be 3 and 6 variables are defined in total, i.e. $\alpha_1, \alpha_2, \alpha_3, \beta_1, \beta_2$ and β_3 , to account for the relative angular position and the phase angle of the applied flux densities of each PPA with respect to the reference PPA.

The objective function in Eq. (4.3.a) then can be rewritten in terms of these design variables shown in Table 4-1. As the next step, the constraints are defined. There are two important constraining factors that need to be taken into consideration for improved accuracy and braking performance. The first factor is the skin effect. Since the model employs alternating flux density as the source, the eddy current generated on the surface of the conductor will also be time varying. When an alternating current (AC) is applied to

a conductor, the current has a tendency to accumulate in the vicinity of the surface of the conductor and, with increasing depth in the material; the current density decreases and diminishes after a certain depth, which is also known as the skin depth. Note that the FEM introduced in [32], which is needed by the optimization procedure, does not account for the skin effects. The skin depth (d_{skin}) can be expressed in terms of the material property of the conductor and the frequency of the applied time varying current as:

$$d_{skin} = \sqrt{\frac{\rho_{res}}{\pi f \mu}} \quad (4.4)$$

where ρ is the resistivity and μ is the absolute magnetic permeability of the conductor, and f is the frequency of the current applied on the conductor surface. Note that the depth is calculated for a sheet with infinite depth. Therefore, for a sheet with finite thickness, the total skin depth will be twice the depth calculated to account for both the top and the bottom surfaces of the sheet.

At low frequencies, the skin effects can be ignored for a thin conductor sheet. However, with increasing frequencies, the skin depth decreases according to Eq. (4.4). Thus, in order to account for this phenomenon in the optimization procedure, the skin depth is included as a constraint on the effective thickness (d_{eff}) of the rotating conductive disk, Eq. (3.b). In the optimization calculations, the effective thickness is used and its value is selected to be whichever the smallest of the thickness (d) the optimization algorithm selects or twice the skin depth (d_{skin}) at the corresponding frequency that the solution is carried out at. Note that the magnetic field applied to the ECB is frequency modulated and does not have a fixed frequency. Thus, for simplicity, it is assumed that the frequency of the carrier field (f_l) defines the skin depth in the braking torque calculations.

The second factor also stems from the alternating (i.e. AC) nature of the problem. With alternating field applications, the computed braking torque will also be alternating. Having such a braking torque for a vehicle will significantly affect the comfort level of the driver and passengers. Unlike the first factor, which is a magnetic phenomenon, the comfort level is a subjective term and the perception will vary from one person to another

and from one vehicle to another as well. In the literature, however, there are a number of studies that were conducted in order to quantify the comfort level of drivers and passengers [51-54]. In these studies, human perception to vibration was measured and quantified experimentally. Although the experiments are used to quantify comfort, one's perception of vibration also depends on cognitive elements such as the nature of the environment where vibration occurs, expectations, role of the vibration and motivation [52].

In these experiments, comfort curves were plotted for individuals. By normalizing these comfort curves, frequency-weighting curves are plotted for different parts of human body. Due to complex damping effects of the human body and the driver/passenger seat, some parts of the body are more sensitive to the vibration than others, such as the back and the buttocks. The vibration is defined using the acceleration values and the RMS of the acceleration is used for the quantifying the comfort level. The RMS acceleration is multiplied with the weighting factors and a range of perceived vibration values are obtained. The general guidelines were required to define the comfort level at corresponding weighted perceived accelerations and one such guideline was suggested by Griffin and his guidelines were incorporated in British Standard 6841 [52]. According to Griffin, the resulting vibration under weighted acceleration of 0.5 m/s^2 (RMS) or less is considered little or not uncomfortable. Between 0.5 and 1.25 m/s^2 (RMS), the vibration is defined as uncomfortable and above 1.25 m/s^2 (RMS), the vibration is considered as very uncomfortable.

In the current study, the comfort level is incorporated into the optimization problem as an additional constraint, Eq. (4.3.c), since it can be a significant problem due to the utilization of the time varying fields as the source of the eddy currents. Herein, it is assumed that in order to keep the vibrations in a tolerable/comfortable range, the weighted acceleration values are set to be lower or equal than 0.5 m/s^2 (RMS). This condition will satisfy a smooth braking curve in order to make it comfortable enough for the driver and the passengers. In order to calculate the deceleration during braking, a loaded vehicle that is 1300 kg is assumed to have four ECB actuators installed, and it is also assumed that all the kinetic energy is dissipated in the brakes.

In addition to the skin effect and comfort level constraints, three additional constraints are defined. The first one, Eq. (4.3.d), is that the surface defined as PPA has to be within the rotating conductor surface, since the eddy currents are specifically generated on the surface of the conductor. Secondly, the neighbouring PPAs cannot have intersections, considering that electromagnet cores that generate the external fields cannot be physically overlapping each other (see Eq. (4.3.e)). Finally, since the deviation frequency (Δf) cannot be higher than the carrier frequency (f_l), the value of the deviation frequency is capped by that of the carrier frequency (see Eq. (4.3.f)).

The optimization procedure was carried out for four different cases, involving sinusoidal and triangular field applications. In the first case, the simplest 1-PPA configuration was optimized and for the subsequent cases, the number of PPAs was increased up to four.

For the ECB optimization problem, a stochastic search optimization algorithm, Genetic Algorithm (GA), was used. Among all available stochastic algorithms, GA can locate good solutions in a short amount of time. However, similar to available stochastic algorithms, the result improves with time. For the specific ECB problem, a tolerance value is defined in order to terminate the optimization. Although stochastic methods are powerful optimization algorithms, they are not guaranteed to converge to the global optimum.

Figure 4-3 shows the flowchart of the optimization algorithm that is carried out for the specific ECB problem. Initially, GA creates the initial population within the user defined design space and then the thickness of the conductor disk is adjusted using the frequency values. After the thickness has been updated, the constraints are checked and if they are not satisfied, the algorithm returns a penalty function as the result for the given configuration. But if the constraints are satisfied then the configuration is studied using the FEM [32] and the resulting braking torque is calculated. Once the torque value is available, the comfort level values can be calculated. If the comfort value is higher than the set limit, i.e. 0.5 m/s^2 (RMS), then the algorithm returns a penalty function for the configuration. However, if the comfort level is less than the set limit, then the configuration is stored. Following the function evaluations, GA carries out mating, crossover and mutation between successful configurations. Once the new population is

created, GA checks whether the termination criterion (i.e. evolution stops when the best fitness value in the current population is less than the user defined fitness) is satisfied or not. If it is not satisfied, the algorithm repeats the whole process to find a new population. However, if the termination criterion is satisfied, then the algorithm ends and it returns the optimum configuration.

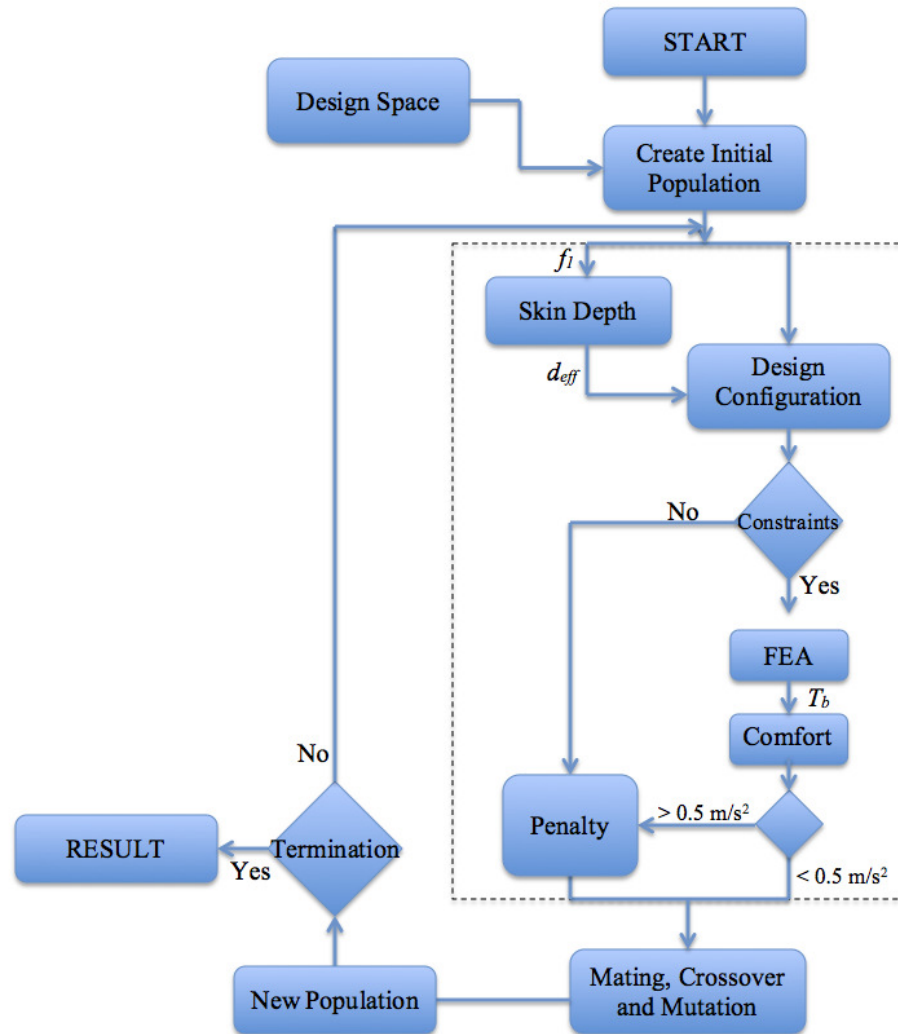


Figure 4-3. Flowchart of the optimization procedure

Thus, in order to increase the accuracy, the optimization algorithm was run multiple times for every case. The results that are shown in Table 4-2 are the optimum values for each design variable obtained after carrying out the optimization several times.

Table 4-2. Optimum ECB Configurations

Design Variables (<i>d</i>)	Optimum Values							
	Sinusoidal				Triangular			
	1 PPA	2 PPA	3 PPA	4 PPA	1 PPA	2 PPA	3 PPA	4 PPA
Radius of the disk, R (m)	0.12	0.12	0.12	0.12	0.12	0.12	0.12	0.12
Thickness of the disk, d (m)	0.01	0.01	0.01	0.098	0.01	0.01	0.01	0.01
PPA width, a (m)	0.05	0.05	0.05	0.05	0.05	0.05	0.05	0.05
PPA height, b (m)	0.05	0.05	0.05	0.05	0.05	0.05	0.05	0.05
Pole location distance, r (m)	0.088	0.081	0.08	0.08	0.088	0.081	0.081	0.081
Position of PPAs, α_n (rad)	-	0.756	0.783, 0.952	0.717, 0.781, 1.7718	-	0.8145	0.7765, 0.9097	0.709, 0.902, 0.786
Carrier Frequency, f_1 (Hz)	31	100	226.65	300.2	34	209.4	241.4	214
Modulation Frequency, f_2 (Hz)	31	100	226.65	300	34	209.4	241	214
Frequency Deviation, Δf (Hz)	30	99	225	299	33	208	240	213
Phase angle between fields at PPAs, β_n (rad)	-	0.858	1.005, 2.404	0.923, 1.2212, 2.569	-	1.054	1.068, 2.564	1.180, 3.536, 2.357

4.4.2 Optimization Results

As mentioned earlier, the optimization was carried out for four different configurations, corresponding to 1, 2, 3 or 4 PPAs, and for both sinusoidal and triangular field applications for each case. The braking torques generated by the optimum brake configurations are presented in Table 4-3. In addition to the braking torques, the comfort levels obtained for each optimum configuration are also given in the same table. Note that in order to obtain these optimization results, the rotational velocity of the conductive braking disk is kept at 100 rpm. In Figure 4-4, the optimum ECB design with 4 PPA's is shown.

Table 4-3. Optimum braking torque values for cases studied

<i>Cases</i>	<i>Sinusoidal</i>		<i>Triangular</i>	
	<i>Braking Torque, Nm (RMS)</i>	<i>Comfort level, m/s² (RMS)</i>	<i>Braking Torque, Nm (RMS)</i>	<i>Comfort level, m/s² (RMS)</i>
1 PPA configuration	33.62	0.2454	34.77	0.4984
2 PPA configuration	260.21	0.4993	285.22	0.4726
3 PPA configuration	480.15	0.497	509.4	0.4792
4 PPA configuration	738.5	0.495	878.8	0.4959

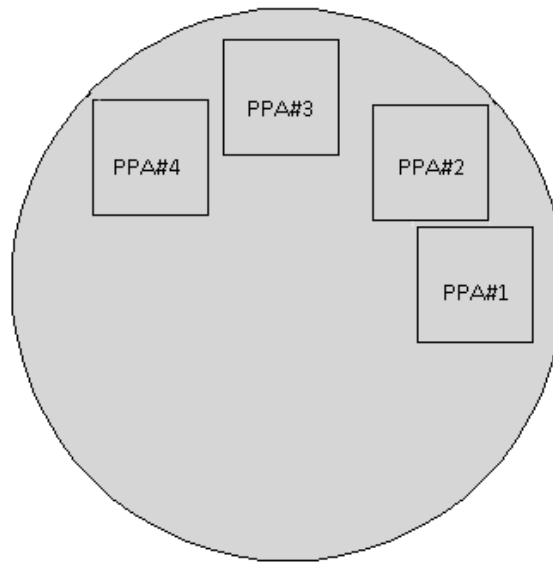


Figure 4-4. Optimum 4-PPA configuration

One significant conclusion that can be made from the table above is that the braking torque significantly increases with the introduction of the second PPA. An optimum configuration with 1 PPA can generate up to around 35 Nm with the application of triangular flux density. However, with the second PPA is added, the braking torque significantly increases, i.e. about 8 times the braking torque generated with 1 PPA ECB configuration. This behaviour can be explained by the interaction between the eddy currents generated under the adjacent PPAs. If the PPAs are positioned as far away from each other as possible (e.g., 180° apart), the interaction will be minimum and the braking torque will be roughly doubled with the introduction of the second PPA. However, as the two PPAs get closer to each other, the interaction between the eddy currents increases the

amount of braking torque generation. Note that the interaction is also strongly dependent on the phase angle of the applied flux densities on the adjacent PPAs. With different phase angles, the interaction may cause reduction in the braking torque when the PPAs are placed close to each other. In terms of the spacing between the PPAs, it is ideal to have them close to each other on the surface of the conductor disk. Thus, the phase angles have to be selected correctly so that the interaction results in an overall increase in the total braking torque.

Although it was not shown in Table 4-3, another interesting result that was observed is that at specific phase angles defined between the flux densities applied onto the PPAs, the braking torque becomes a positive value instead of a negative value. This means that instead of decelerating, the particular ECB configuration will accelerate the rotation of the wheel. This phenomenon is also due to the interaction between the eddy currents generated by adjacent PPAs. This phenomenon is called electromagnetic propulsion and it is currently used for accelerating levitated trains in a linear manner. The phase angles can be adjusted in such a manner that the poles of the PPAs are attractive to each other, which will accelerate the rotating disk. However, as our interest lies in a brake actuator, the above optimization algorithm searches for the phase angles that will generate a negative braking torque that acts to slow down the rotation of the wheel.

Finally, a last comment that can be made is that there is still room for additional PPAs on the ECB configuration presented in Figure 4-4. This will lead to a further increase in the braking torque, which is discussed further in the next section, at the expense of higher complexity, increased weight, power requirement and cost.

4.4 Discussions

Although ECBs have a number of performance advantages over CHBs, their braking torque generation capacity at the low vehicular speeds is considerably limited. In this paper, in order to improve the braking performance of the ECB, the braking torque generation of the ECB with multiple PPAs is optimized, with the consideration of comfort and skin effects, as well as geometric and field dependent factors.

In previous study [32], results showed that the braking torque increases with the application of time varying fields. In addition, among various waveforms, triangular field

resulted in the best braking torque generation. Further analysis also proved that the braking torque can be significantly increased with the application of frequency modulated signal. In this paper, the ECB was optimized with the application of frequency modulated sinusoidal and triangular external fields. In addition to the improvements resulted from the external fields, the performance can be improved by reducing the induction effects and in order to do so, it is assumed that laminated cores are used to generate the external magnetic fields.

The results of the optimization are given in Table 4-2 and Table 4-3, which show that the braking torque significantly increases with the introduction of additional PPAs. In this section, for discussion purposes, the configuration with the maximum braking torque output is selected for further investigation. As mentioned earlier, the peak magnitude of the applied flux density was selected to be 1.225 T that is comparable to the same configuration with 0.707 T DC field application in terms of the energy input to the systems. Thus, here both systems are compared in terms of the braking torque generation capacity across various rotational velocities of the conductor disk. Figure 4-5 shows the variation of the braking torque generation with respect to the rotational velocities for the optimum 4-PPA-configuration.

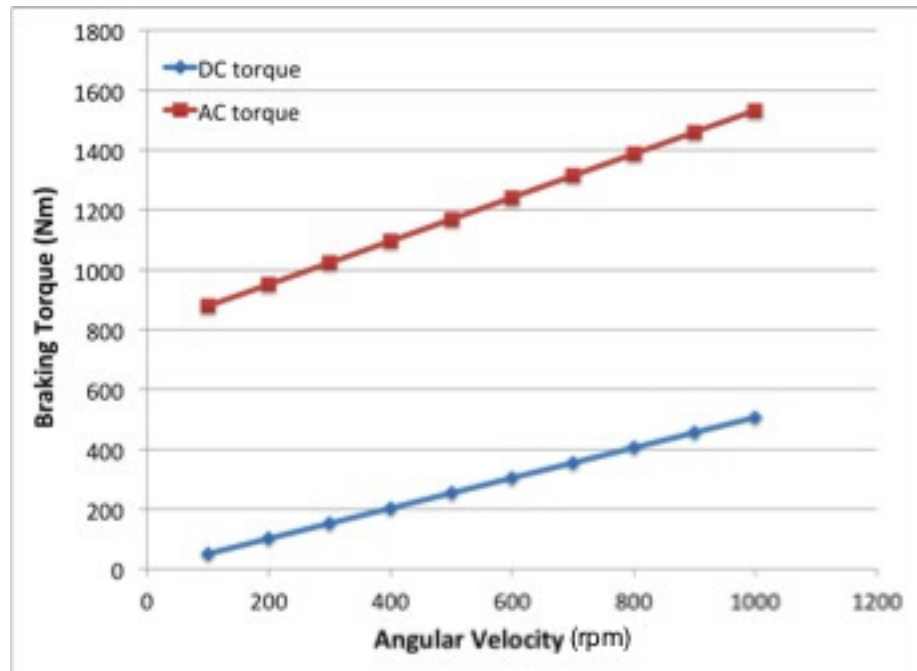


Figure 4-5. Braking torque generation at various angular velocities

The results show that the braking torque increases drastically with the application of the frequency modulated triangular field at both high and low speeds. According to the results, the braking torque generated with the AC field application at low rotational velocities around 100 rad/s reaches as high as 17 times that of the DC field application. On the other hand, at higher velocities around 1000 rad/s, the increase is not as dramatic; the braking torque with the AC field application is 3 times that of the DC field application. Note that the AC field generated braking torques in Figure 4-5 are RMS values.

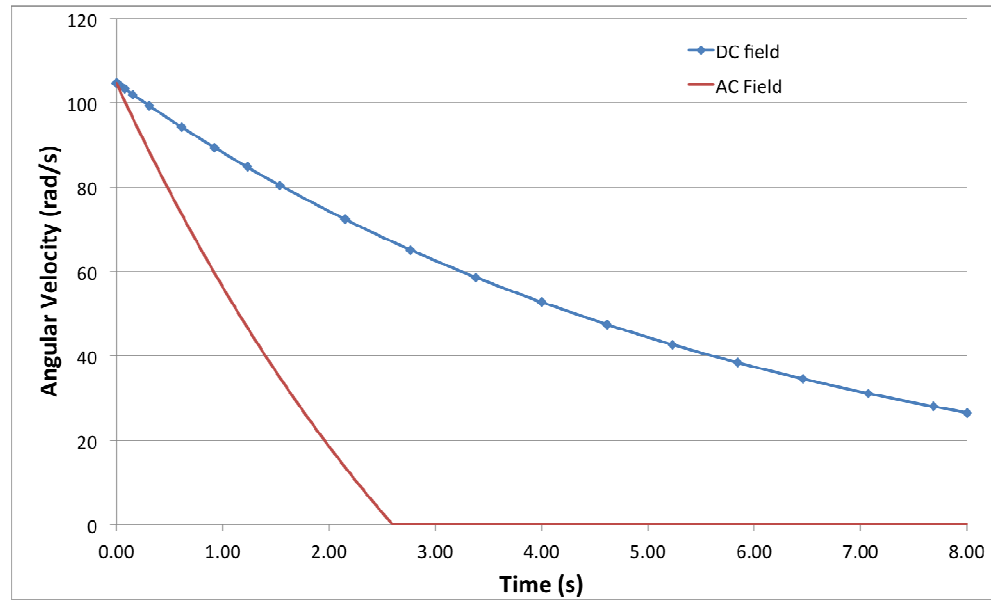


Figure 4-6. Deceleration curve

As the next step, the corresponding deceleration curve is presented in Figure 4-6. For these simulations, it is assumed that the optimum 4-PPA-configuration ECB is installed on each wheel of a 13-inch wheel vehicle, fully loaded at 1300 kg. Initially, it is assumed that the wheels are rotating at a speed of 104 rad/s (1000 rpm). Note that this rotational speed corresponds to about 120 km/h for a vehicle with the 13-inch wheels. Simulations are carried out for 8 seconds. The curve with the diamond data points in Figure 4-6 represents the deceleration with the DC field application and the smooth curve represents the deceleration with the AC field application. When only the DC field is applied, the rotational velocity of each wheel decreases down to 25 rad/s after 8 seconds. However,

with the application of the AC field, the vehicle stops after only about 2.7 seconds. It is evident that the deceleration performance of the vehicle with the AC-based ECBs is significantly better than that of the vehicle with the DC-based ECBs.

If the figure is investigated closely, unlike the smooth DC field deceleration curve, AC field deceleration curve oscillates due to the alternating nature of the braking torque generated. But since the comfort level was a part of the optimization procedure, the deceleration should not be uncomfortable for the passengers.

From the deceleration curves of the AC and DC based ECB configuration, the corresponding linear deceleration value can be obtained for the vehicles themselves. Since the vehicle equipped with the AC-based ECBs is brought to a full stop from 120 km/h in 2.7 seconds, this corresponds to a linear deceleration of about 12 m/s^2 , which is three times more than the linear deceleration that can be achieved with the vehicle equipped with the DC-based ECBs. This deceleration corresponds to about 1.2 g's. For comparison, most passenger vehicles have rated decelerations of around 0.8 to 1 g's and some fast sport cars can achieve decelerations varying from 1 g to 5-6 g's, with the use of carbon ceramic friction brakes [55].

The amount of the braking torque generated by the AC-based ECBs is enough for slowing down regular passenger vehicles. However, for heavier vehicles such as trucks, the required amount braking torque is significantly higher. In order to meet these higher braking torque requirements, the ECB configuration has to be further improved. The configuration that was studied employs up to 4 PPAs; however, as mentioned in the previous section, there is room to add more PPAs. In Table 4-2, the summation of α_n 's is less than 180° and this implies that all 4 PPAs are located within the one half of the conductive braking disk as it is depicted in Figure 4-4. Introducing addition PPAs will drastically increase the braking torque in a similar trend as shown in Table 4-3. In addition to introducing more PPAs, the ECB can be further optimized specifically for the heavy vehicle application. The wheel dimensions will be bigger for a truck than for a passenger vehicle. This will result in utilizing conductive disks with bigger diameters compared to those for passenger vehicles. Having a bigger radius will result in higher braking torques due to the increase in the moment arm and also there will be more room to introduce new PPAs on the surface of the conductive braking disks. Looking at the

results presented in Figure 4-5 and Figure 4-6, it can be concluded that the braking torque requirements for heavy vehicles can also be achieved with the increased size of the conductive disks and the introduction of additional PPAs.

In terms of the simulations, here genetic algorithm, a stochastic search optimization algorithm, is used to optimize the braking torque generation of the AC ECB. For a highly nonlinear problem, search algorithms offer higher possibility to converge the global optimum. However, the simulations are generally computationally heavy and time consuming compared to gradient-based algorithms. Another limitation in this work is the accuracy of the mathematical model of the triangular waveform studied here. In order to model the waveform, here first 10 harmonics of the field is used. Since the problem is dependent on the first and the second time derivative of the field (see Eq. (3.8)), the accuracy of the derivatives decreases with increasing order of derivatives.

4.5 Conclusion

In previous work, the use of AC fields in order to improve the braking torque generation of ECBs is investigated with the help a finite element model and results showed that the braking torque is higher when the field has a varying frequency instead of fixed frequency and when it is applied in triangular waveform compared to sinusoidal, square and sawtooth waveforms. In this work, ECB was optimized for higher braking torque. In addition to the geometric and field dependent factors, skin effects due to alternating currents generated on the surface of the conductor and the comfort level of the passengers due to the vibration during braking are accounted for in the optimization problem. Genetic Algorithm was then used to find the optimum ECB configuration. Finally, the results showed that the braking torque significantly increases with the application of AC fields on a multiple PPA ECB configuration. Also the deceleration curves showed that the AC field application on the optimum configuration shown in Table 4-2 with 4 PPAs resulted in about 12 m/s^2 , which is more than 20-25 % of the accelerations that can be achieved with CHBs on average passenger vehicles.

5. CONTROL

5.1 Introduction

In previous chapters, the ECB was modeled analytically and numerically, and then its braking torque generation capacity was optimized using Genetic Algorithm. It was shown that an ECB configuration with the time varying field application has the potential to generate braking torques comparable to that of the conventional brake actuators. In this chapter, a model based predictive controller is designed for improved braking performance.

The main objective of this chapter is to design a closed-loop controller that can maintain a desired ECB performance. Although there are a number of candidate control methods that can be used for the ECB problem, herein model predictive controllers are chosen for the ECB problem due to the availability of the analytical and FE models.

Model predictive control (MPC) is a control method that employs an explicit process model to estimate the future response of a system. At every interval, MPC determines a sequence of variable adjustments that optimize future response of the system. Once the sequence is determined, then the first optimum input is sent to the system and the same procedure is carried out for every control interval. The method was originally introduced for power plant and petroleum refinery control applications.

MPC has successfully been used in numerous applications ranging from chemical, food processing, automotive, aerospace, metallurgy to pulp and paper industries [56,57], due to three important factors. Firstly, MPC uses an explicit plant model. Therefore, it directly includes any significant process dynamics. Secondly, it determines the response over a future horizon. This helps the controller to remove any feed-forward and feedback disturbances, thus allowing the controller to follow a closer future trajectory. Finally, MPC includes the input, state and output constraints directly in the controller calculations. Therefore, it ensures operation within certain physical limits.

In general, MPC is used with linear models; however, due to the nonlinearity in many real-world applications, nonlinear MPC (NMPC) was introduced. In NMPC, a linear model is used to estimate the future response of the plant. When the system is nonlinear, two

common approaches are used. In the first approach, MPC is linearized at multiple process points where the model is linearized individually and a switching algorithm is used to make the selection between these controllers depending on the process states. In the second approach, MPC uses a nonlinear model to determine the response. The approach that is selected strictly depends on the physics of the plant. For an accurate nonlinear model, the second approach results in an accurate trajectory [58].

Although it has a number of advantages, NMPS has a fundamental difficulty, as it requires an optimum solution of the input over a future horizon for optimum response at each control action. Therefore, for real-time control, a result must be determined within the time step specified for the controller. Having simplified physics or simple linear models results in faster convergence to the optimum input values. In the literature, there are a number of studies where MPC was successfully implemented in real-time using linear models [58, 59, 60, 61]. Also, there are a number of applications where the dynamics were considerably slow. In [62], an NMPC was designed for flood prevention of a river system and in [63], it is used to normalize the glucose levels in blood for critically ill patients. In both cases, the sample time was set to be 5 minutes.

On the other hand, in [64], NMPC was applied to an ore-milling problem in mining and a successful controller was designed with a sample time of 10 seconds. In [65], an unmanned rotorcraft was designed and NMPC was used to avoid any terrain in the path. Due to the complex nature of the model, sample rate for this application was selected to be 20 ms. As the problem gets complex, the sampling time goes even smaller due to the sudden changes in the physics of the problem. In [66], the sampling rate was selected to be 1 ms for a robotic hand and eye coordination system.

In terms of the time varying field application in ECB, the problem is significantly complicated considering the physics presented in Chapter 2. In addition, looking at the optimum results obtained in Chapter 4, it can be concluded that for an accurate system the sampling rate has to be kept significantly small (e.g., if ~ 300 Hz sinusoidal signal is applied as the external field).

Herein, for the current ECB problem, with the help of analytical and FE models, a dynamic model is obtained using model identification tools. Once the braking torque generation is calculated for the optimum configuration selected, a quarter vehicle model is

used in conjunction with the ECB model to calculate the dynamics of the vehicle during braking. Since NMPC requires a discrete time nonlinear model, the ECB model is then converted into a discrete time model and the state variables (velocities and accelerations of the wheel and the vehicle) are defined at every time step. Once the model is ready, an objective function with adequate constraints is defined to drive the system to a desired steady state. At every time step, an optimum future response of ECB is calculated over a horizon of length 50. The first value of the input is then applied to the plant at the specific time step and the procedure is repeated until the last time step. Similar to [67], to solve the optimization problem, particle swarm optimization algorithm (PSO), a non-gradient based algorithm, is used in this work. Simulations are carried out and the closed-loop control results of the proposed ECB controller are presented later in this chapter.

This chapter is organized as follows. The ECB configuration that is used to design the controller is introduced in Sec. 5.2. Since the models introduced in Chapter 2 and 3 are highly nonlinear and complex, a simplified dynamic ECB model is created using the knowledge gained in both the analytical model and FEM. In Sec. 5.3, the quarter vehicle model is introduced and this model is used to calculate the dynamics of the vehicle during braking. In the following section, Sec. 5.4, the proposed NMPC algorithm is introduced and a controller is designed for the ECB problem. In Sec. 5.5, the simulation results are presented. Finally, in Sec. 5.6, a brief conclusion is given to summarize the work carried out in this chapter.

5.2 Dynamic ECB Model

The optimization results of Chapter 4 showed that the braking torque significantly increases with the additional PPAs, with the capacity to exceed that of a conventional hydraulic brake. For control design purposes, the braking torque generation model of the optimum ECB configuration is needed. In Chapter 2, an analytical model was presented; however, this model does not account for the use of multiple PPAs. Therefore, it cannot be directly used to model the braking torque generation for the optimum ECB configuration. In Chapter 3, an accurate FEM was introduced; however, due the complexity and nonlinearity of the problem, this model is unsuitable for design of a real-time controller for the ECB.

Therefore, in this section, a simplified dynamic model for the braking torque generation of the optimum ECB configuration with 4 PPAs is derived with the help of both the analytical and FE models and nonlinear model identification tools.

The FEM introduced in Chapter 3 was used to solve the braking torque generation under frequency modulated sinusoidal field application on an optimum ECB configuration with 4 PPAs at various rotational speeds. The results data is then used to create a dynamic model of the specific ECB with the help of the analytical model. Although the analytical model does not account for the frequency modulated field application nor the multiple PPA configurations, it can give important insight information about the correlation between the externally applied field, rotational speed of the conductor brake disk and generated braking torque.

The generated braking torque model for a 1-PPA configuration was given in Eq. (2.48). From this equation, it is clear that the braking torque is comprised of a geometric function (G_f), a time function (T_{time}) and a coefficient (C). The geometric function is simply a function of the dimensions of the conductor disk and PPA as well as the location of their boundaries. On the other hand, the coefficient C is comprised of material properties such as conductivity (σ), permittivity (ε) and magnetic permeability (μ) as well as the field magnitude (B_{in}) and rotational speed of the disk (w). Finally, the time term is resulted from the alternating field application. The braking torque in Eq. (2.48) can then be rewritten in terms of generic geometric and time functions and the coefficient term as follows:

$$T_b = C(B_{in}, \mu, \sigma, \varepsilon, w) \cdot T_{time} \cdot G_f(d, a, b, R, r) \quad (5.1)$$

where d , a , b , R , and r are the thickness of the disk, width and the height of the PPA, radius of the disk and the distance pole location distance, respectively.

For a given configuration, the material properties and the geometric function will be constant and the magnitude of the applied field (B_{in}), the rotational velocity of the brake disk (w) and the time function (T_{time}) will be changing depending on the braking requirements. Therefore, for the ECB problem, B_{in} and w are the inputs to the brake system and the output will be the braking torque (T_b). Note that it is assumed that the time

function is constant for the configuration and the controller alters the braking torque by varying the magnitude of the applied field.

In order to come up with a real-time dynamical model for the ECB, initially the proportionality between the inputs and the output is defined. From the equations in Chapter 2 and the results presented in the same chapter, it can be concluded that the braking torque is proportional with the square of the magnitude of the applied field and the rotational velocity. Note that this makes the system nonlinear. In addition, in Figure 4-5, the braking torque generation was plotted for an optimum configuration under the constant magnitude time varying field application. Using the analytical model and the results obtained in Chapter 4, the coefficient value in Eq. (5.1) can be rewritten as:

$$C = B_{in}^2 \cdot (w \cdot c(\mu, \sigma, \varepsilon) + c_1) \quad (5.2)$$

where c is a coefficient that is calculated using the material properties of the conductor ECB disk and c_1 is an arbitrary constant.

As the next step, the time function can be estimated using the time variation term inherited from the externally applied field. Since the torque is proportional with the square of the externally applied field, the proportionality will be similar between the torque and the sinusoidal time function that defines the applied field as well. Since the time term is a part of the externally applied field, for a sinusoidal field with frequency modulation, the time function will be as follows:

$$T_{time} = \left[\sin \left(2\pi f_1 t - \frac{\Delta f}{f_2} \cos(2\pi f_2 t) \right) \right]^2 \quad (5.3)$$

where f_1 is the carrier frequency, f_2 is modulation frequency and Δf is the frequency deviation. Using Eq. (5.2) and Eq. (5.3), Eq. (5.1) can be rewritten in terms of the applied field and the rotational velocities, i.e.

$$T_b = (B_{in}^2 \cdot (w \cdot c(\mu, \sigma, \varepsilon) + c_1)) \cdot \left[\sin \left(2\pi f_1 t - \frac{\Delta f}{f_2} \cos(2\pi f_2 t) \right) \right]^2 \cdot c_2 \quad (5.4)$$

where c_2 is the constant value of the geometric function for the selected ECB configuration. Note that for the 4-PPA configuration, phase differences were introduced between the applied fields of each PPA. In order to account for the phase differences, the braking torque equation can be redefined as:

$$T_b = c_2(B_{in})^2(w c(\mu, \sigma, \varepsilon) + c_1) \left[\sin \left(2\pi f_1 t + p - \frac{\Delta f}{f_2} \cos(2\pi f_2 t + p) \right) \right]^2 \quad (5.5)$$

where p is the phase difference of the applied field at the PPA compared to a reference field. Once the correlation is defined, the dynamic ECB model can be obtained using the results of the FEM by estimating the coefficients in Eq. (5.5) using model identification methods. Note that the frequencies for the optimum braking torque generation under the sinusoidal field application are known (see Table 4-2), and these values are used in Eq. (5.5) to estimate the braking torque. Also, the above equation is defined only for one PPA. Since the optimum configuration contains 4 PPAs, 4 different braking torque values must be defined and be summed up to estimate the total braking torque.

$$T_{b,n} = c_2(B_{in})^2(w c(\mu, \sigma, \varepsilon) + c_1) \left[\sin \left(2\pi f_1 t + p_n - \frac{\Delta f}{f_2} \cos(2\pi f_2 t + p_n) \right) \right]^2 \quad (5.6)$$

$$T_{b,total} = T_{b,1} + T_{b,2} + T_{b,3} + T_{b,4} \quad (5.7)$$

where p_n is the phase difference and $T_{b,n}$ is the braking torque generated at the n^{th} PPA, and $T_{b,total}$ is the total braking torque generated by the optimum 4-PPA ECB configuration. Note that the applied field to the first PPA is assumed to be the reference field so the phase differences of the other PPAs are calculated in comparison to this field. Therefore p_1 is equal to zero.

In Figure 5-1, the FEM results (blue solid line) and the estimated dynamic model (black solid line) are compared. The simulation is carried out for a sinusoidal variation at 100 Hz in the magnitude of the applied field, B_{in} (T), and decreasing rotational velocities, w (rpm).

$$B_{in} = 0.5 + 0.5 \cdot \sin(2\pi 100t) \quad (5.8)$$

$$w = 1000 - 1000 \cdot t/0.5 \quad (5.9)$$

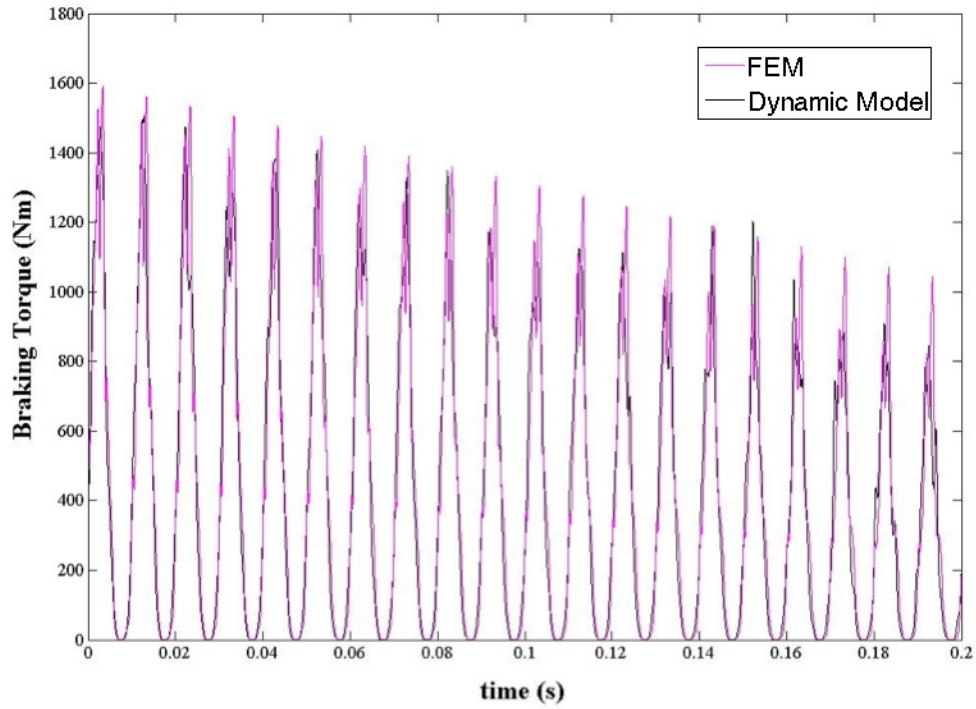


Figure 5-1. Comparison between the estimated model and the FEM results

The simulation results show a good agreement between the two models. Therefore, the estimated dynamic model is used in the subsequent sections to estimate the braking torque generation of the optimum 4-PPA ECB configurations for control design purposes.

5.3 Dynamic model of the vehicle

In this section, the vehicle dynamics are studied in order to calculate the deceleration values using the braking torque generated by 4 ECB actuators of the 4-PPA configuration. The motion of a vehicle can be described using the quarter vehicle model [68]. This model uses the assumption that the weight of the vehicle is distributed equally between the four wheels so that the calculations can be carried out by defining the dynamics of only one wheel. Since the system is a reduction from the whole vehicle, the weight of the reduced system is assumed to be the $1/4^{\text{th}}$ of the total weight of the vehicle. In addition,

the total inertia of the system is also approximated to a total value using inertias of wheel, engine and the brake disks. The approximated values and the calculations are presented in detail in Appendix A.

After defining all the forces acting on the wheel, the Newtonian equations of motion for the wheel can be solved for deceleration values (see Eq. (A.7) and Eq. (A.8)).

$$\ddot{x} = \frac{-\mu_f g}{1 - \frac{\mu_f m_v h_{cg}}{l_{base} m_t}} \quad (5.10)$$

$$\ddot{\theta} = (-T_{b,total} + \mu_f R_w F_n - R_w F_r) / I \quad (5.11)$$

where $\ddot{\theta}$ is the deceleration, $T_{b,total}$ is the total braking torque generated by the ECB (see Eq. (5.7)), μ_f is the friction coefficient, R_w is the radius of the wheel, F_n and F_r are the normal and the rolling resistance forces applied on the wheel and I is the total mass moment of inertia of the vehicle. (For further details on the equations and the free body diagram of the wheel, see Appendix A.)

5.4 Design of a model based nonlinear predictive controller

5.3.1 Nonlinear model predictive control algorithm

In Figure 5-2, a block diagram of the proposed nonlinear model predictive controller is presented. As mentioned previously, NMPC utilizes an explicit dynamic model of the plant in order to determine the optimum response in taking the system to a desired steady state. In this section, the proposed NMPC algorithm is briefly explained using a plant, which is defined in state space.

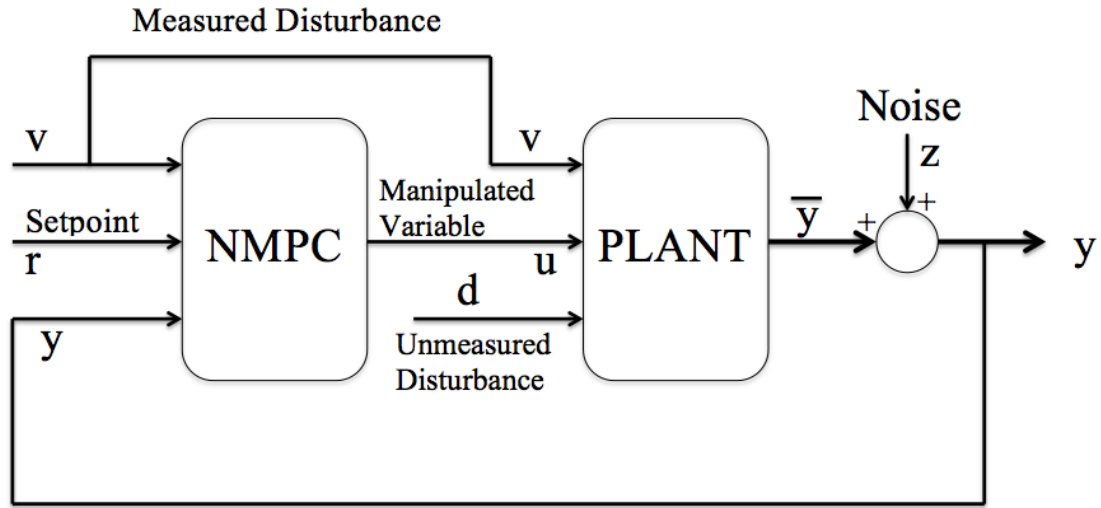


Figure 5-2. Nonlinear model predictive control block diagram

For the NMPC controller, a discrete time model of the plant is necessary for optimum trajectory determination. Assume that the nonlinear plant can be described in state space, e.g.,

$$\mathbf{x}_{k+1} = \mathbf{f}(\mathbf{x}_k, \mathbf{u}_k, \mathbf{v}_k, \mathbf{d}_k) \quad (5.12)$$

$$\mathbf{y}_k = \mathbf{g}(\mathbf{x}_k) + \mathbf{z}_k \quad (5.13)$$

where $\mathbf{u}_k \in \mathcal{R}^{n_u}$ is a vector of n_u plant inputs (or manipulated variables (MVs)), $\mathbf{y}_k \in \mathcal{R}^{n_y}$ is a vector of n_y plant outputs (or controlled variables (CVs)), $\mathbf{x}_k \in \mathcal{R}^{n_x}$ is a vector of n_x system state variables, $\mathbf{v}_k \in \mathcal{R}^{n_v}$ is a vector of n_v measured disturbance variables (DVs), $\mathbf{d}_k \in \mathcal{R}^{n_d}$ is a vector of n_d unmeasured DVs and $\mathbf{z}_k \in \mathcal{R}^{n_z}$ is a vector of measurement noise.

The control algorithm determines a sequence of inputs (\mathbf{u}_{k+j}) that will drive the system from the plant's current state (\mathbf{x}_k) to a desired steady state (\mathbf{x}_s) according to an economic objective. The algorithm carries out a local steady state optimization in order to find the desired state. In addition to the system variables, the measured and unmeasured DVs are included in the \mathbf{f} function defined in Eq. (5.12) and the measurement noise (\mathbf{z}_k) is included in the output as a bias term, which compares the current output values (\mathbf{y}_k) to the

measured output (\mathbf{y}_k^m). Also note that it is assumed that the bias term is constant for any given time.

Once the plant is defined, as the next step, an optimization problem is created for the plant according to the desired behaviour of the system. A simple nonlinear objective function that is commonly used for NMPC applications is shown below [57]:

$$\min J(\mathbf{u}^M) = \sum_{j=1}^P \|\mathbf{e}_{k+j}^y\|_{\mathbf{Q}_j}^q + \|\mathbf{s}_j\|_{\mathbf{T}_j}^q + \sum_{j=0}^{M-1} \|\mathbf{e}_{k+j}^q\|_{\mathbf{R}_j}^q + \|\Delta \mathbf{u}_{k+j}\|_{\mathbf{S}_j}^q \quad (5.14)$$

The equality and inequality constraints are defined for a tighter control at the optimal constrained steady state of the process [58]:

$$\mathbf{x}_{k+j} = \mathbf{f}(\mathbf{x}_{k+j-1}, \mathbf{u}_{k+j-1}) \quad \forall j = 1, P \quad (5.15)$$

$$\mathbf{x}_{k+j} = \mathbf{g}(\mathbf{x}_{k+j}) + \mathbf{b}_k \quad \forall j = 1, P \quad (5.16)$$

$$\underline{\mathbf{y}}_j - \mathbf{s}_j \leq \mathbf{y}_{k+j} \leq \bar{\mathbf{y}}_j + \mathbf{s}_j \quad \forall j = 1, P \quad (5.17)$$

$$\underline{\mathbf{u}} \leq \mathbf{u}_{k+j} \leq \bar{\mathbf{u}} \quad \forall j = 0, M-1 \quad (5.18)$$

$$\Delta \underline{\mathbf{u}} \leq \Delta \mathbf{u}_{k+j} \leq \Delta \bar{\mathbf{u}} \quad \forall j = 0, M-1 \quad (5.19)$$

$$\mathbf{s} \geq 0 \quad (5.20)$$

In Eq. (5.14), there are 4 main terms to be defined for the optimum control problem. The first term (\mathbf{e}_{k+j}^y) is the deviation of the calculated output (\mathbf{y}_{k+j}) from the desired steady state output (\mathbf{y}_{ss}) over a horizon of length P , i.e.

$$\mathbf{e}_{k+j}^y = \mathbf{y}_{k+j} - \mathbf{y}_{ss} \quad (5.21)$$

Also, a positive definite weight matrix, (\mathbf{Q}_j) is defined to account for the relative importance between these 4 terms defined. The second term in this equation (\mathbf{s}_j) is the slack variable that penalizes the output constraint violations (see Eq. (5.17)). This term also has a weight matrix (\mathbf{T}_j) to define its relative importance. The third term (\mathbf{e}_{k+j}^q) is the deviation of the calculated input term (\mathbf{u}_{k+j}) from the desired steady state input (\mathbf{u}_{ss}), i.e.

$$\mathbf{e}_{k+j}^u = \mathbf{u}_{k+j} - \mathbf{u}_{ss} \quad (5.22)$$

The weight matrix defined for the input deviation term is \mathbf{R}_j . Finally, the last term in this equation penalizes the rapid input changes and the weight matrix is specified as \mathbf{S}_j . Note that all these deviation and constraint violation terms are defined as norms of vectors (either L_1 or L_2 norms ($q = 1, 2$)). For the specific ECB problem, q is set to be 2 and the terms in Eq. (5.14) are defined as follows:

$$\|\mathbf{e}_{k+j}^y\|_{\mathbf{Q}_j} = (\mathbf{e}_{k+j}^{yT} \cdot \mathbf{Q}_j \cdot \mathbf{e}_{k+j}^y)^{0.5} \quad (5.23)$$

$$\|\mathbf{s}_j\|_{\mathbf{T}_j} = (\mathbf{s}_j^T \cdot \mathbf{T}_j \cdot \mathbf{s}_j)^{0.5} \quad (5.24)$$

$$\|\mathbf{e}_{k+j}^u\|_{\mathbf{R}_j} = (\mathbf{e}_{k+j}^{uT} \cdot \mathbf{R}_j \cdot \mathbf{e}_{k+j}^u)^{0.5} \quad (5.25)$$

$$\|\Delta \mathbf{u}_{k+j}\|_{\mathbf{S}_j} = (\Delta \mathbf{u}_{k+j}^T \cdot \mathbf{S}_j \cdot \Delta \mathbf{u}_{k+j})^{0.5} \quad (5.26)$$

In the above, the derivations were shown for a generic NMPC algorithm [57]. Figure 5.3 shows the flowchart of the algorithm. The reader can find a more in-depth description of the algorithm in [56] and [58].

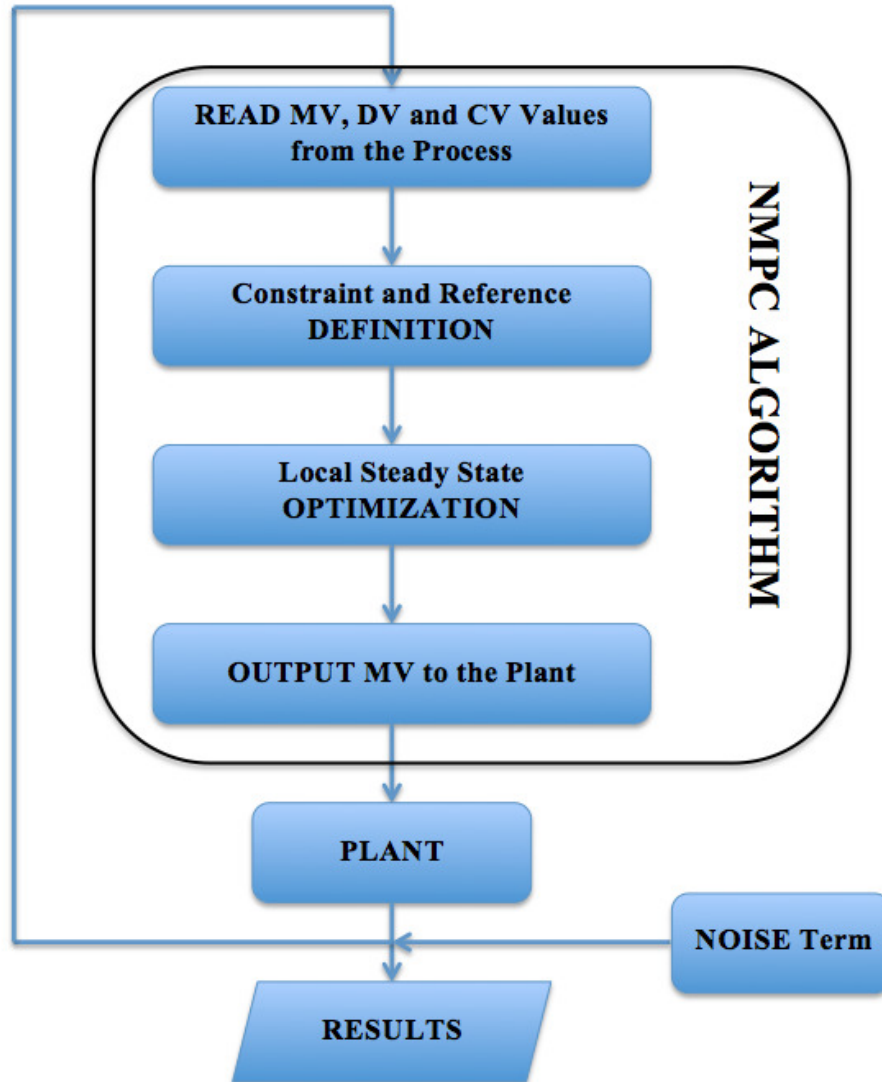


Figure 5-3. NMPC Flowchart (MV - manipulated variables, DV - disturbance variables and CV - controlled variables)

5.3.2 NMPC applied to ECB problem

The ECB model defined in the previous section is a continuous one and, in order to be able to design a NMPC controller, this model has to be converted into a discrete time model. Note that for the ECB problem, all the disturbance terms are ignored ($\mathbf{v}_k, \mathbf{d}_k = 0$ in Eq. (5.12)) and all variables (velocity and acceleration terms for both the wheel and the vehicle) are defined as MVs. In addition, the measurement noise is assumed to be zero

($\mathbf{z}_k = 0$ in Eq. (5.13)). The output from the system is defined to be the deceleration of the vehicle.

In terms of the ECB, braking torque generation can be converted into a discrete model using the relationship below. Note that the torque is a function of the angular velocity of the wheel and the magnitude of the applied field.

$$T_{b,total_k} = h(B_{in_k}, \dot{\theta}_k, t_k) \quad (5.27)$$

where h is the dynamic model identified in Sec. 5.3.1 and t_k is the time. Note that the notation in the quarter vehicle is adapted for w (i.e. the angular velocity, $\dot{\theta}_k$) in this section. As the next step, the dynamic vehicle model is converted into discrete equations using the relationships below. Refer to Appendix A for the full continuous set of equations used here. Also, the variables and the constant that are selected for the vehicle model used for the analysis is shown in Table 5-1.

$$F_{r_k} = f_0 + 3.24f_s(K_v\dot{x}_k)^{2.5} \quad (5.28)$$

$$F_{n_k} = m_t g + \frac{m_v h_{CE}}{l_{base}} \ddot{x}_k \quad (5.29)$$

$$s_{r_k} = \frac{\dot{x}_k - R_w \dot{\theta}_k}{\dot{x}_k} \quad (5.30)$$

$$\mu_{f_k} = \begin{cases} s_{r_k}/0.175 & 0.175 \geq s_{r_k} \geq 0 \\ 1 - \frac{0.2(s_{r_k}-0.175)}{0.825} s_{r_k} & s_{r_k} > 0.175 \end{cases} \quad (5.31)$$

$$F_{f_k} = \mu_{f_k} F_{n_k} \quad (5.32)$$

Note that the friction coefficient is obtained from an empirical plot between the slip ration and the friction coefficient between the tire and the road (see Figure A-2). For the purposes of current control design, it is assumed that the vehicle is moving on a dry surface.

Table 5-1. Specifications of the vehicle and road conditions

Wheel Radius	R_w	0.326 m
Wheel Base	l_{base}	2.5 m
Center of Gravity Height	h_{cg}	0.5 m
Wheel Mass	m_w	40 kg
1/4 of the Vehicle Mass	$m_v/4$	415 kg
Total Moment of Inertia of wheel and engine	I_t	1.75 kg.m ²
Basic Coefficient	f_o	10e-2
Speed Effect Coefficient	f_s	0.005
Scaling Constant	K_v	2.237

Considering that the state vector contains the speed and acceleration terms for the wheel and the vehicle, the state in the next time step can be calculated using the dynamic equations and approximate integration equations as shown below. Eq. (5.33) and Eq. (5.34) are obtained using the equations of motion and using these two relationships, angular acceleration of the wheel and the acceleration of the vehicle are found (For ECB applications, accelerations are negative). Note that these terms not equal due to the slip between the road and the wheels.

$$\ddot{x}_{k+1} = -\mu_{f_k} g + \mu_{f_k} \frac{m_v h_{CE}}{l_{base} m_t} \ddot{x}_k \quad (5.33)$$

$$\ddot{\theta}_{k+1} = \frac{(-T_{b,total_k} + R_w F_{n_k} - R_w F_{r_k})}{I} \quad (5.34)$$

$$\dot{x}_{k+1} = \frac{\ddot{x}_{k+1} + \ddot{x}_k}{2} \Delta t + \dot{x}_k \quad (5.35)$$

$$\dot{\theta}_{k+1} = \frac{\ddot{\theta}_{k+1} + \ddot{\theta}_k}{2} \Delta t + \dot{\theta}_k \quad (5.36)$$

The velocity terms are then calculated using direct integration. Eq. (5.35) and Eq. (5.36) are obtained using the trapezoidal rule. This approach is not ideal for cases where the noise is significant. However, since it is assumed that the noise to the system is negligible, the approach selected to calculate the velocity terms are deemed accurate. Using the above equations, the state at the next step can be calculated.

As the next step, an objective function with adequate constraints for the ECB NMPC design. An objective function similar to Eq. (5.14) is defined, i.e.

$$\min J(\mathbf{u}^M) = \sum_{j=1}^P \|\mathbf{e}_{k+j}^y\|_{\mathbf{Q}_j} + \|\mathbf{s}_j^u\|_{\mathbf{T}_j} + \|\Delta \mathbf{u}_{k+j}\|_{\mathbf{S}_j} \quad (5.37)$$

Deviation of the vehicle deceleration from a specified reference value is set to be the first penalizing factor in the objective function for the ECB. Here, it is assumed that for comfortable braking, the deceleration reference value of the vehicle is set to be 6 m/s^2 ($=\ddot{x}_{ss}$). The second term is the slack term. Unlike the general form, here it is defined for the input, B_{in} . This slack factor ensures that the control signal, magnitude of the externally applied field, is bounded as shown in Eq. (5.38). Finally, the last term is the penalty for rapid input changes in the system. In addition, weight factors are assigned for each penalty term.

$$0 \leq \mathbf{u}_{k+j} \leq 1.5 \quad \forall j = 1, P \quad (5.38)$$

Note that for the subsequent simulation analysis, the time step is selected to be 0.1 ms in order to account for the explicit dynamics of the system, considering that the time varying field application is at 300 Hz. While having a longer horizon will result in better accuracy, since the time step is significantly low, the length of the horizon for the ECB control problem is set to be 50.

5.5 Simulation results

In order to carry out the controller simulations, an optimization algorithm must be selected. There are a vast number of optimization algorithms readily available in the literature. These algorithms can be classified into two main categories; gradient based and non-gradient base. Gradient-based systems are not successful when there are local minima. Gradient-based techniques utilize an initial guess and the gradient data to estimate the direction towards the minimum. If the system is highly nonlinear, the result

of such an algorithm may converge to a local minimum instead of a global minimum. In terms of controller design, such results may cause stability issues in the system.

For the ECB problem herein a non-gradient based search algorithm, Particle Swarm Optimization (PSO), is used to find the global minimum. Among gradient free algorithms, PSO is a recently introduced global optimization technique that has been used with great success in the area of computational intelligence. It is a direct search algorithms that is used to find the global optimum in a given search space. Due to its simple formulation, it is easy to implement, apply, extend and hybridize the algorithm. The algorithm is modeled on swarm intelligence, which is based on the social-psychological principles exist within large groups of organisms. Communication or social network is critical for this algorithm, through which individual solutions passes the location of the best neighbouring solution by means of a fitness value. PSO was first introduced by Kennedy and Eberhart [69] and their study was inspired by the social behaviour of birds. In order to find food, each bird flies with a velocity and a direction, and these are determined by experience and the interaction of the bird with other birds in the flock. Every bird, particle, will be assigned with a direction and a velocity and it will then search for the optimum in the search space and its position represents a potential solution.

The simulations are carried out and the results obtained are presented in Figure 5-4. For the specific simulation, the brakes are applied for a 5 second duration to slow the vehicle down from about 120 km/h. The first plot shows the variation in the control variable, B_{in} , during the simulation. As it was bounded in the optimization problem, the input did not exceed the 1.5 T limit specified. Also, the values are increasing as time progresses. Since the braking torque decreases with decreasing velocities, B_{in} is increased to account for the decrease in the braking torque. Another constraint in the problem was the reference value defined for the deceleration of the vehicle. The variation of the deceleration is shown in the 4th plot in the same figure. It can be seen that the deceleration converges rapidly to -6 m/s^2 within 0.1 s and the controller makes sure the system stays at this desired steady state for the rest of the time during braking. The last constraint that was penalized in the objective function was the amount of input changes. This prohibits a significant jump in the magnitude of the applied field intensity, as shown in the first plot.

The same figure also shows the variation of the angular velocity of the wheel (2nd plot) and the linear velocity of the vehicle (3rd plot) and the displacement of the vehicle during braking (5th plot). The displacement is calculated using trapezoidal rule similar to Eq. (5.35) and Eq. (5.36).

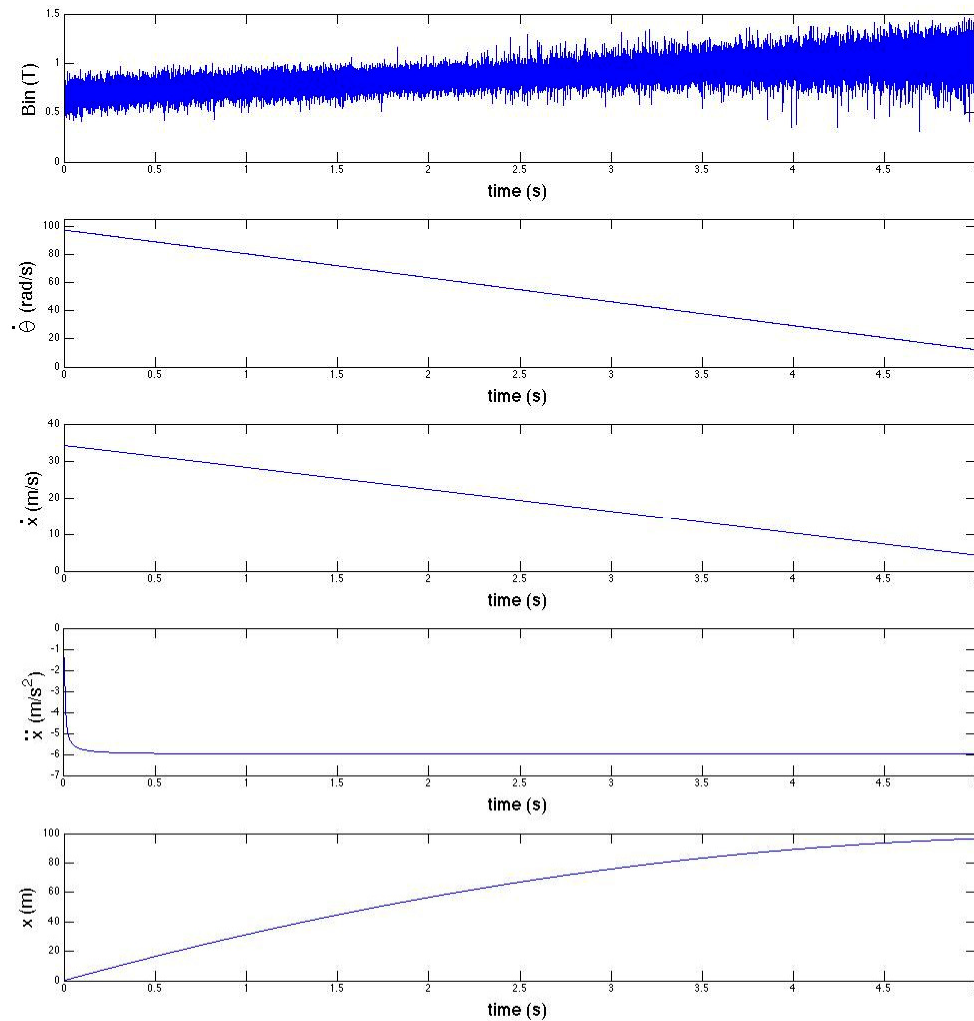


Figure 5-4. ECB performance with NMPC

The controller performance can be improved by adjusting the optimization problem and by introducing additional penalty terms depending on needs. In terms of the simulations, the accuracy of the controller will increase as the time step decreases and as the length of

the horizon is increased. However, as these modifications are made, the optimization will require longer time to determine the response over the horizon defined and it will be harder to implement the controller real-time.

Compared to a no control scenario, having such a controller will result in a number of performance improvements in power consumption and in brake parameter tuning for different braking scenarios. Power storage and consumption are critical issues for electric cars. In terms of braking, the controller optimizes the power input to the brakes through adjusting the magnitude of the applied magnetic field and this will ensure that the braking objectives, which are user-based or environmental-based, are going to be achieved with minimum power input to the system.

In terms of tuning, the objective function can be defined for various braking conditions. For the specific case presented in Figure 5-4, a reference value is set for the deceleration and the brakes generate enough braking torque to converge to the set reference value. The system can be modified easily by properly defining the objective function according to needs. This makes it possible to generate optimum braking performance for different braking conditions, i.e. braking on a slippery surface, emergency braking, controlled braking, etc. For emergency braking, reference value can be removed and the inputs that are going to result in highest braking torque at all times can be calculated. For controlled braking, the reference value of the deceleration can be adjusted according to the pressure on the brake pedal applied by the driver. For slippery surfaces, an objective function that is defined using the relative velocities of the wheel and the vehicle can be used. Once the function is properly defined, this will result in no-slip braking. For real road braking simulations, all these conditions can be implemented in the controller and an adaptive or switching control algorithm can be employed to define the appropriate braking parameters for the system.

Although it is an advantageous algorithm, the main limitation of the above control system is the computational cost in obtaining accurate future trajectories using optimization. The computational cost significantly depends on the nonlinearity of the problem and it directly affects the real-time performance of the controller. In order to improve the real-time performance, the model can be linearized around the operating point or a faster search algorithm can be used.

5.6 Conclusion

In this chapter, a controller is designed for an optimum configuration presented in Chapter 4. Initially, a dynamic model of the system is obtained for the ECB and the vehicle to determine the state variables (speeds and acceleration terms of the wheel and the vehicle.). Since the analytical and FE model are previously studied in this thesis, the application is suitable for model predictive control. Here a NMPC is designed for the system by defining an objective function along with constraints that will drive the plant to a desired steady state. The simulations are carried out for a scenario where the vehicle is slowed down from 120 km/h to 10 km/h in 5 seconds. The results show that the system reaches the steady state within 0.1 s and NMPC makes sure the system is behaving as requested for the rest of the time during braking.

6. EXPERIMENTAL STUDIES

6.1 Introduction

The design of the ECB does not include any complexity since it is essentially composed of a conductive disk attached to the wheel shaft and the source of the applied magnetic field. Therefore, apart from all the advantages mentioned earlier, this type of brake is very easy to prototype. Considering applications where DC field is applied on the conductive disk, the source of the field can be a simple high-intensity permanent magnet. Thus, it is very easy to assemble a brake actuator using off the shelf components.

Such configurations are used to slow trains before the stations when they start slowing down for a full stop at the station. Having permanent magnets laid on the railway realizes a simple ECB configuration (the metal tires of the train are the conductive disks of the ECB configuration presented Figure 1-3. in Chapter 1). In previous chapters, it has been shown that the AC field application improves the braking torque generation significantly. However, in order to be able to introduce the time variation in the applied field, electromagnets must be used and they become the main complexity of the design for a configuration where AC field is applied.

For experimentation, the most important component is to design an electromagnet that supplies the required field with minimum losses. There are two major losses on an AC electromagnet [70,71], one of them is eddy current loss and the other one is the hysteresis loss. Although eddy currents are favourable in this study for braking torque generation, in terms of electromagnets, when there are eddy currents present, an opposing field will be created within the magnet core and this opposing field will reduce the applied field significantly. Therefore, in practice, specific materials with high permeability and low conductivity are used to eliminate the possibility of eddy current generation on the magnet core. Ferrite cores are a good example to such materials. Ferrite has high magnetic permeability and they are considered non-conductive. In addition, they are readily available and cheap. However, the saturation flux density of the ferrite is significantly low compared to other options (about 0.5 T [72]).

Also, laminated steel is another popular alternative for AC electromagnet cores. High magnetically permeable and high conductive materials are stacked on each other with a layer of nonconductive bonding in between. This will prevent the flow of eddy currents from one strip to other, thus making the core nonconductive with a high magnetic permeability. They are preferable for applications where higher magnetic flux densities are required for the application due to their high saturation flux density levels. However they are not readily available and in general, they are stacked according to the requirements of the specific problem. Therefore they are a lot more expensive than ferrite cores.

The other loss, hysteresis loss, is caused by the switching direction of the applied field on the core. Due to the coercivity of the magnetic core selected for the application, some of the energy will be lost at every change of direction. Coercivity can be expressed as the resistance of the material to changes in magnetisation. The energy lost is proportional to the area between enclosed by the hysteresis curve of the material. In power transformers, in order to be able to reduce this loss, soft coercive materials, such as silicon steel or soft ferrite, are used.

Here in this chapter, the experimental studies that are carried out for the ECB and the setup that is designed for the experiments are explained in detail. In the first section, the experimental setup that was used to measure the braking torque is presented and the equipment is introduced. In the following two sections, DC and AC field experiments are presented. Note that the experimental studies are only carried out for the DC case but the setup and ECB prototype are prepared for the AC field experiments which will be carried out in future (see Chapter 7 for a list of future works).

6.2 Experimental setup

In order to be able to measure the braking torques generated, an experimental setup is designed. A servomotor from CMC Inc. with a continuous torque of 5.13Nm and with rotational speed of 5445 rpm is used to generate the continuous torque. Since the torque generation capacity of the servomotor is relatively low, an ALPHA 0755-MC1-7 gear reducer (7:1) is used. The servomotor is then connected to a FUTEK torque sensor

(TRS605), which is a shaft-to-shaft rotary torque sensor with a torque measuring capacity up to 1000 Nm. The other end of the torque sensor is connected to the ECB prototype. An Inertia Dynamics magnetic clutch is installed between the torque sensor and the servomotor in order to release the load on the servomotor generated by the brake. In order to connect the various components, flexible couplings are used. Below in Figure 6-1, the components of the experimental setup are shown and at the right end of the figure, in the metal casing, there is the ECB configuration selected for the DC field application experiments.

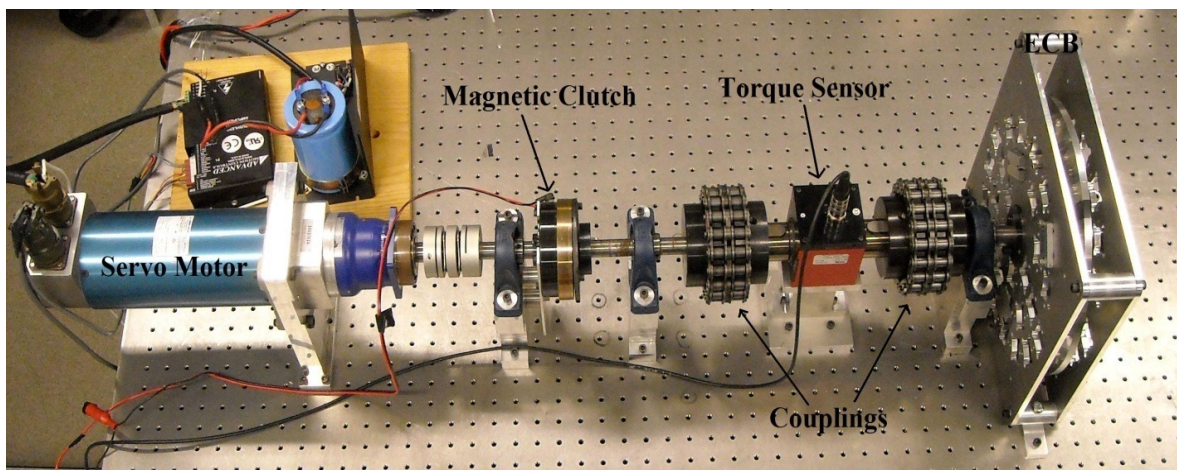


Figure 6-1. Experimental setup

The servomotor is controlled with a proportional-integral-derivative (PID) controller and the rotational speed of the brake is verified using the encoder embedded in the torque sensor. All input and output signals are connected to a dSPACE control board (DS1104). The control signal from the dSPACE board to the servo is amplified using an Advanced Motion Control Brushless PWM servo amplifier. In addition, a low-pass filter circuit is implemented into the setup in order to reduce the high frequency noise in the torque sensor readings.

During the experiments, the rotational speed is kept constant at various values. Whenever the brake is actuated, since the system is at steady state, the relative torque measured between the shafts on each side of the torque sensor is recorded as the braking

torque generated by the brake prototype. After the braking torque data is obtained, the magnetic clutch was turned on in order to release the torque load on the servomotor.

6.3 DC field application

In order to verify the DC FEM, an ECB prototype was built and the braking torque generation at various angular velocities was recorded. During the experiments, a custom conductor disk was used along with permanent magnets positioned on each side of the disk. Figure 6-1 shows the experimental setup used. It consists of a servomotor (on the left), magnetic clutch, couplings, torque sensor and the brake actuator (on the right). The conductor disk is mounted in between two static fixtures where the magnets are hold in place. Figure 6-2 shows a close-up image of the ECB. The permanent magnets can easily be seen on both sides of the rotating disk.

The specifications for the setup are given in Table 6-1. Figure 6-3 shows the comparison between the FE simulation and experimental results. The nonlinear behaviour of the experimental system is evident in the figure, compared to that of the FE simulation results. The more linear behaviour of the FE simulation is probably due to the initial assumption that the DC field does not change with respect to the spatial coordinates and un-modeled dynamic effects such as variations in the magnetic property with respect to temperature. Note that since permanent magnets (instead of electromagnets) are used here the induction effect can be ignored.

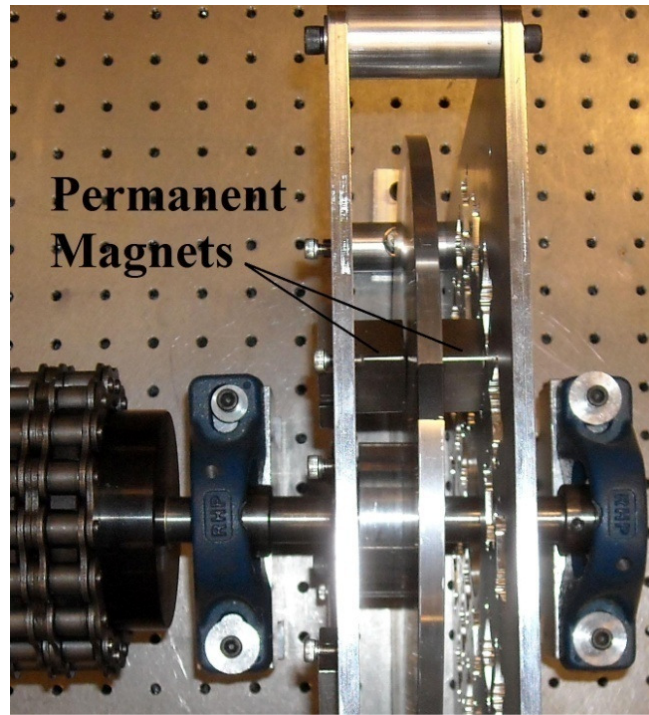


Figure 6-2. Eddy current brake (ECB) prototype with permanent magnets

Table 6-1. Experimental setup specifications

Radius of the disk (m)	0.1524
Width of PPA (m)	0.0254
Height of PPA (m)	0.0254
Center of PPA (m)	0.0762
Thickness (m)	0.00714
Material	Aluminum Alloy 6061
Conductivity (S/m)	5.79E+07
Magnet	Permanent Magnets (no induction effect)
Field	0.749 T (Peak) and 0.475 T(min)

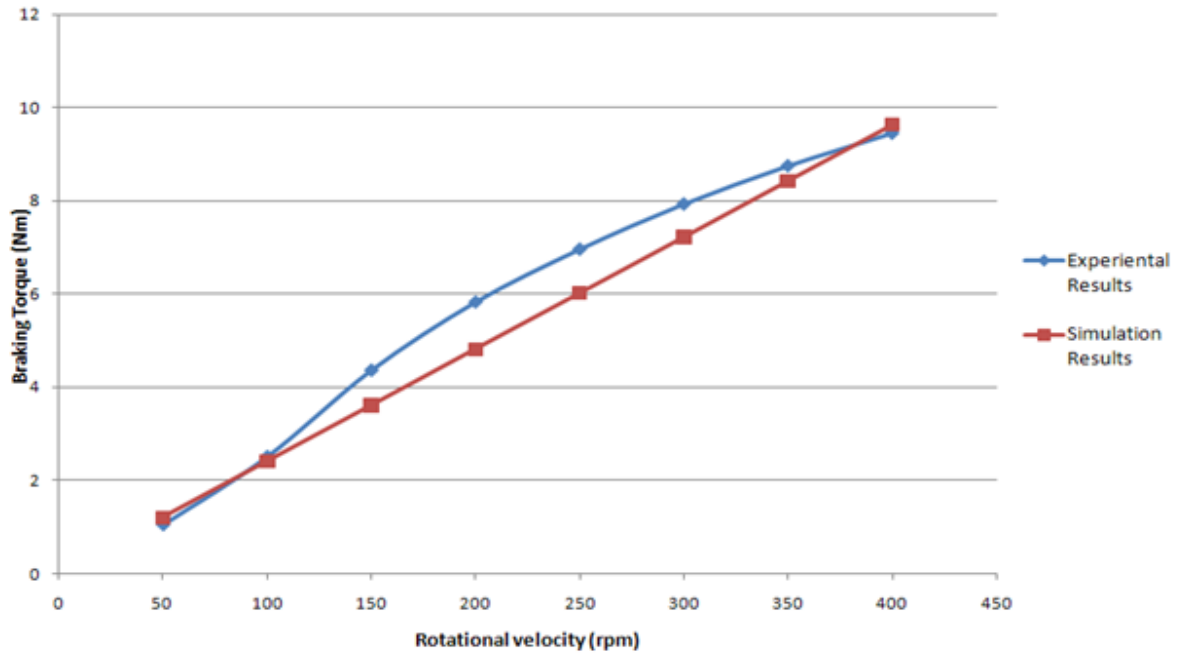


Figure 6-3. Comparison between the FE simulation and experimental results for the prototyped configuration

In this experiment, permanent magnets were used in the ECB instead of electromagnets for quick preliminary testing. The simulation and experimental results are in a good agreement. There are a number of important conclusions that can be made from Figure 6-3. First conclusion is that the braking torque vs. disk velocity is a nonlinear behaviour. The fact that the FE simulation showed a more linear relationship is due to the fact that the FEM assumed a uniformly distributed applied magnetic field over the PPA on the ECB's disk. This implies that the applied field does not have a spatial dependence. Due to this assumption, the last term on the right hand side of Eq. (6.1), i.e.

$$\nabla \times \mathbf{E} + \nabla \times (\mathbf{v} \times \mathbf{B}) + \nabla \times (\mathbf{v} \times \mathbf{B}_0) = \frac{1}{\mu_0 \sigma d} \nabla \times (\nabla \times \mathbf{B}) + \frac{1}{\mu_0 \sigma d} \nabla \times (\nabla \times \mathbf{B}_0) \quad (6.1)$$

becomes negligible. However, in reality, the distribution of the field on the PPA is not uniform. When the magnetic flux leaves the core of the magnet, it bulges out of the straight linear path and curves back into the opposing pole. Because of this bulging effect, the field distribution in the air gap is different from that of in the core. These non-uniform

fields are called the fringing fields, and they result in a spatially varying field distribution in the PPA (i.e. maximum field intensity in the center of the PPA and decaying field intensity towards the edges). Another source of nonlinearity is the stray flux (fringing fields are considered to be a subset of the stray flux, but for the sake of discussion, herein they assumed to be separate). Herein, the stray fields are defined as fields that leave the electromagnet from the core surface, not the pole face, and enter the opposing pole through the core surface, again not through the pole face. These fields create a PPA that is larger than the area of the pole face, where the FEM assumes that the PPA and the area of pole face are equal. Figure 6-4 shows the flux density distribution between two permanent magnets in a streamline plot and stray flux can easily be seen between the magnets.

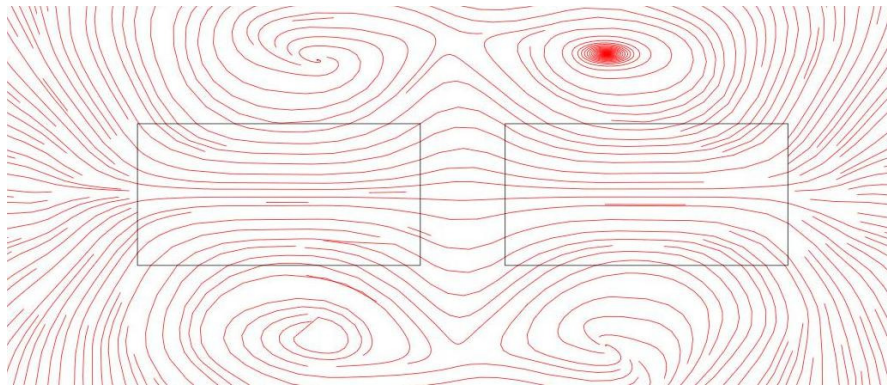


Figure 6-4. Flux density distribution between two permanent magnets

In addition to the FEM assumption of uniformly distributed field, environmental and measurement noise in the readings as well as the material property change due to the increasing temperatures cause the nonlinearity in the experimental results presented in Figure 6-3.

Another important conclusion that can be drawn from the experimental results is that the amount of braking torque generated still seems to be quite lower than what is required for a passenger vehicle, even at high velocities (see Appendix B for requirements for various vehicles). Some solutions to this problem have already been addressed earlier in Section 3.4.

6.4 AC field application

Unlike the previous DC field application case, here for AC field application, electromagnets are required. In addition to the setup described earlier, a power source will be supplying the current to the electromagnet, which is the source of the applied field for the experiments. Since the field is alternating, the power source should be able to supply alternating current to the coil of the electromagnet. For this specific purpose, a power supply (Agilent 6813B with a power rating of 1750 VA) is used. This power supply is capable of supplying currents up to 13 A, and also this specific power supply is equipped with arbitrary waveform generator which will be useful to apply fields in numerous waveforms.

From the results presented in Chapter 4, it can be said that an optimum configuration can generate over 800 Nm with 4 PPA, although the torque sensor can measure torques up to 1000Nm, the servomotor would not be able to withstand such a high torque. As was mentioned earlier, the braking torque is calculated at steady state, when the brake and the servomotor are activated at the same time. With the gearbox used, the setup can generate slightly over 35 Nm. Therefore, for experimentation, a configuration which can generate braking torques less than the limiting torque the motor can supply is selected.

The dimensions of the PPA are another limiting factor for prototyping as well. For the specific experiments, ferrite cores are obtained from Magnetics, Inc. (#0P49920UC). They are standard C shaped cores (specifications of the core is given in Appendix C) with one end grinded down (3.5 mm down), so that in order to complete an electromagnet, 2 cores are attached together and the clearance accounts for the air gap (7 mm in total) where the conductive disk will be placed. The diagram below shows the core of the AC electromagnet that is designed for the AC field-testing of ECB. Note that the upper part, where the cores join, are attached to each other using a thin layer of adhesive and they are joined right after the coil bobbin is placed in position.

As was mentioned earlier, ferrite has low coercivity and high permeability and in addition it is consider a non-conductive material. Thus it is a very good candidate for AC electromagnets. They are cheap and readily available. However, the biggest problem with the material is the saturation flux density. Once the core reaches the saturation, the relative permeability goes down to 1, making it a non-magnetic material; therefore the

flux will be forced to find another path with high permeability (less reluctance) [72]. Ferrite saturates around 0.5 T thus it is not a good candidate for applications where high magnetic flux densities are required.

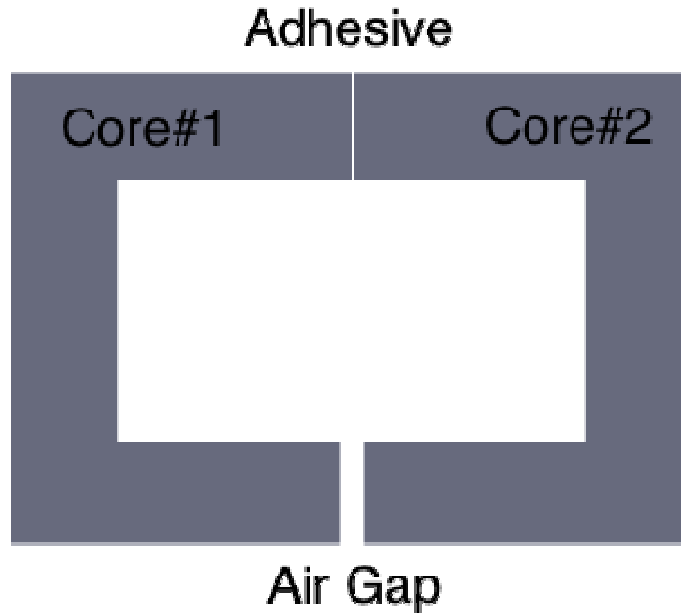


Figure 6-5. AC electromagnet core configuration

As the next step, the coil needs to be designed as the source of the applied magnetic field. Looking at the dimensions presented in Appendix C and the configuration shown in Figure 6-5, the dimensions of the coil bobbin that can be placed on the electromagnet core can be easily calculated. For the specific problem, AWG 21 is selected since more current density can be applied through this size of wire compared to other sizes [73].

Considering all the dimensions of the selected magnet cores, an ECB configuration is created and the specifications of the ECB are given in the table below. Also note that in Table 4-3, the braking torque generation for optimum configurations with different numbers of PPAs were given. Considering the limits on the supplied torque by the servomotor, a one PPA configuration with sinusoidal or triangular field application is selected.

Table 6-2. Specifications of the optimum one PPA configuration from Table 4-3

Radius of the disk (m)	0.12
Width of PPA (m)	0.028
Height of PPA (m)	0.02
Center of PPA (m)	0.0762
Thickness (m)	0.005
Material	Aluminum Alloy 6061
Conductivity (S/m)	5.79E+07
Magnet	Ferrite core – AC electromagnet
Magnet Permeability (relative)	1500 [74]
Bobbin inner dimensions (m)	0.028 x 0.02 (Core cross section)
Bobbin outer diameter (m)	0.025
Coil wire gauge	AWG 21
Number of turns	~2500
Applied current (A)	< 2
Estimated applied flux amplitude (T)	0.5 T (peak)
Estimated DC torque	~13 Nm (No induction)
Estimated AC torque	~7 Nm (~12 Nm peak - No induction)
AC field	Sinusoidal

Table 6-2 shows the specifications of the selected configuration as well as estimated applied external field magnitude and the braking torque generated. In order to be able to keep the applied flux high, the bobbin dimensions are kept at their max and according to the estimates; the bobbin can accommodate around 2500 turns on itself. This coil will be enough to apply necessary field to generate flux densities that are close to the saturation flux density of the ferrite core, which is around 0.5 T [74].

Since the applied flux density and the dimensions of the conductive disk and the PPA are known, the FEM model introduced in Chapter 3 can be used to estimate the amount of braking torque generated under the specified circumstances. Figure 6-6 shows the ECB configuration that is implemented into the FEM and according to the results, with DC and AC field applications, braking torque generated reaches about 13 Nm and 8 Nm (RMS) respectively. For the AC case, the peak value reaches about 12 Nm. Note that AC braking torque is less than DC torque, because for AC field application, the peak magnitude cannot be over 0.5 T, which results in a field that has an RMS flux density of 0.35 T.

Therefore the energy input for DC and AC cases are not identical. DC case takes more energy in and results in higher braking torques.

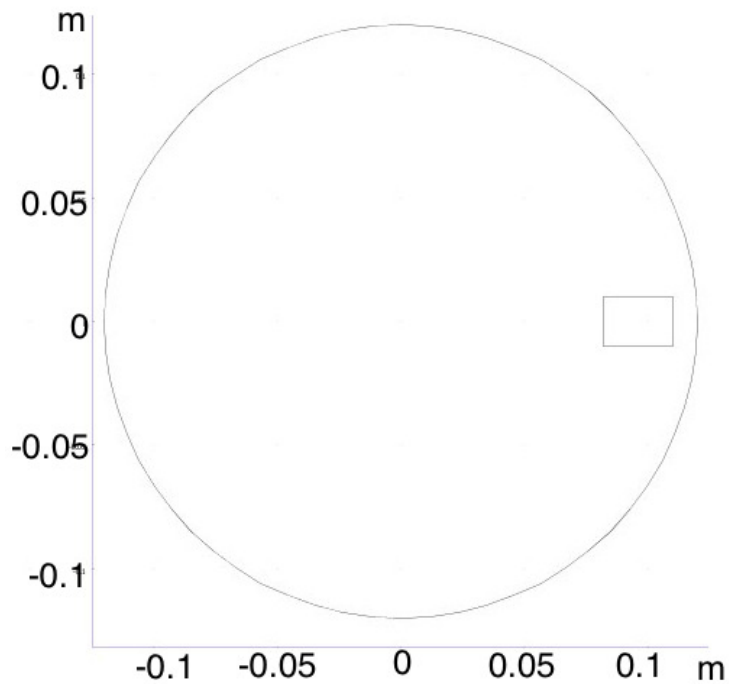


Figure 6-6. Selected ECB configuration for experimentations

As it was mentioned earlier, the AC field experiments are not carried out in this study, due to time constraints and the availability of equipment and material supplies. AC field experiments are one of the future works that is going to be addressed in the following section.

6.5 Summary

In this chapter, an experimental setup that was designed for AC and DC field experiments was introduced. The setup consists of a servomotor as the source of the rotation and a torque sensor and an encoder to measure the speed of the rotation. In terms of the ECB prototype, for DC field application, a simple design with permanent magnets was selected. The experiment results showed the nonlinear nature of the variation in the braking torque and this nature was related to non-modeled physics and magnetic

phenomena such as stray flux and the assumptions made for numerical and analytical models.

Unlike the DC field experiments, for the AC field application case, the experiments were not carried out; however the ECB configuration and the electromagnet were selected and prototyped for experimentation. The main constraint in the design is the material properties of the ferrite core. Due to its low saturation flux density, the electromagnet won't be able to generate more than 0.5 T (peak) field. Using the specifications ECB, the braking torque generation was estimated by the FEM introduced in Chapter 3. According to the results, the brake will generate torques around 8 Nm RMS, when an AC field is applied. The experiments comprise the future work on the ECB research.

7. CONCLUSIONS AND FUTURE WORK

7.1 Conclusions

This thesis focuses on the improvements of automotive brakes with the use of electromechanical ECBs. ECBs have numerous advantages over conventional brakes and these potential advantages make ECB an attractive substitute to current brakes. However, the braking torque generation of the ECB is strictly dependent on the rotational speeds of the conductive disk and at low speeds, braking torque decreases significantly. Thus in order to be able to realize a stand-alone ECB actuator, this problem was addressed in this thesis.

An application of alternating fields to increase the amount of eddy currents generated is proposed and the effects of AC field application were extensively studied. In Chapter 2, an analytical model was developed using modified Maxwell's equations in potential form and the model was validated using a preliminary FEM. In Chapter 3, an accurate FEM that can account for phenomena like induction and skin effects was developed and the model was then validated using analytical models for AC and DC field applications individually. Then using this model, the application of various time varying fields in different waveforms with or without frequency modulation was investigated. Moreover, in Chapter 4, ECB was optimized using the model created previously. ECB problem was defined along with geometric constraints as well as driver/passenger comfort constraints. Here, the methodology of quantifying the subjective comfort was described in detail. The results show that a configuration with four PPA using triangular field waveforms can result in braking torques higher than the torque achieved by conventional hydraulic systems. In Chapter 5, a model predictive adaptive controller was designed and for the control purposes, a dynamical model was created using the analytical model and FEM mentioned in previous chapters. The results show improvements in braking for various scenarios. Finally in Chapter 6, the experimental studies that were carried out to validate the ECB braking performance are presented. In this chapter, experimental results for DC field application on a custom configuration were shown. The main focus of this chapter is

on the design of a test bed for testing the braking performance of ECB with AC field application for validation purposes.

7.1.1 Summary of Chapter 2

The effects of time varying field application on the braking torque generation of ECB are studied. In order to be able to calculate the braking torque, an analytical model is introduced and presented and then this model was validated using an accurate FEM. It is concluded here that although there is an error calculated about 10% between the results of the analytical model and the FEM, they are in good agreement. In addition, the reasoning behind this error along with the nature of the variations of the braking torque with frequency and angular velocity was discussed in detail. Finally, from the preliminary results, it is concluded that with the application of the time varying field, the braking torque generation of the ECB increases.

7.1.2 Summary of Chapter 3

In this chapter, Eddy Current Brakes (ECBs) are proposed as possible substitutes for the conventional hydraulic brakes (CHBs) in automotive applications due to its unique potential for performance advantages (e.g., non-contact and fast response). As a potential solution for the limited braking torque of typical ECBs at low speeds, the application of time varying fields (i.e. AC) is proposed. A finite element model (FEM) that accounts for the effects of time varying fields on the performance of the ECB was developed, which was then validated using an existing analytical model for the DC field. It was shown that improved braking performance can be obtained when AC fields are used at both low and high velocities. Time varying fields in different waveforms (i.e. sinusoidal, square, sawtooth and triangular waves) were applied and triangular wave field application resulted in the highest braking torque. The numerical results also showed that the braking torque decreases with increasing braking torque due to induction effects when the time varying fields are applied. In order to increase the braking torque generation, the induction effects were eliminated and braking torque generation was maximized for sinusoidal and triangular field applications on a generic ECB configuration for automotive applications. A further improvement was subsequently proposed by application of frequency modulated (FM) AC fields. The results showed that a 60% increase in the braking torque can be

achieved with the FM compared to the DC field braking. Further improvements in braking torque generation of the ECB can be achieved by means of increasing the magnitude of applied field, the number of PPAs and the rotational speed of the conductor disk using gears.

7.1.3 *Summary of Chapter 4*

The use of AC fields in order to improve the braking torque generation of ECBs is investigated with the help a finite element model that is validated with existing analytical models. Preliminary studies showed that the braking torque is higher when the field has a varying frequency instead of fixed frequency and when it is applied in triangular waveform compared to sinusoidal, square and sawtooth waveforms. After the preliminary study, ECB was optimized for higher braking torque. In addition to the geometric and field dependent factors, skin effects due to alternating currents generated on the surface of the conductor and the comfort of the passengers due to the vibration during braking are accounted for in the optimization problem. Genetic algorithm was then used to find the optimum configuration. The results showed that the braking torque significantly increases with the application of AC fields, i.e. the increase is 1600 % compared to the DC braking torque at low speeds and 200% at high speeds. Also the deceleration curves showed that the AC field application on the optimum configuration resulted in about 12 m/s^2 , which is more than 20-25% more than the accelerations that can be achieved with average passenger vehicles.

7.1.4 *Summary of Chapter 5*

In A controller was designed for an optimum configuration presented in Chapter 4. Initially, a dynamic model of the system is obtained for the ECB and the vehicle to determine the state variables (speeds and acceleration terms of the wheel and the vehicle.). Since the analytical and FE model are previously studied in this thesis, the application is suitable for model predictive control. Here a NMPC is designed for the system by defining an objective function along with constraints that will drive the plant to a desired steady state. The simulations are carried out for a scenario where the vehicle is slowed down from 120 km/h to 10 km/h in 5 seconds. The results show that the system

reaches the steady state within 0.1 s and NMPC makes sure the system is behaving as requested for the rest of the time during braking.

7.1.5 *Summary of Chapter 6*

An experimental setup was designed for AC and DC field experiments. The setup consists of a servomotor as the source of the rotation and a torque sensor and an encoder to measure the speed of the rotation. In terms of the ECB prototype, for DC field application, a simple design with permanent magnets was selected. The experiment results showed the nonlinear nature of the variation in the braking torque and this nature was related to non-modeled physics and magnetic phenomena such as stray flux and the assumptions made for numerical and analytical models.

Unlike the DC field experiments, for the AC field application case, the experiments were not carried out; however the ECB configuration and the electromagnet were selected and prototyped for experimentation. The main constraint in the design is the material properties of the ferrite core. Due to its low saturation flux density, the electromagnet will not be able to generate more than 0.5 T (peak) field. Using the specifications of the ECB, the braking torque generation was estimated using the FEM introduced in Chapter 3. According to the results, the brake generates torques around 8 Nm RMS, when an AC field is applied. These experiments are proposed to be complete as future work.

7.2 **Future works**

In order to finalize the ECB research, the work presented here in this thesis needs to be carried out further in order to further validate and evaluate the models presented and the results obtained. The future work can be divided into four themes.

In Chapter 6, an ECB prototype is designed and the test bed developed for AC field and DC field experiments is presented. As the next step, a simple ECB configuration with time varying field application needs to be adapted and the brake actuator will be designed and prototyped. The design will be strictly constrained by the capacity and properties of the existing test bed (see Chapter 6 for details). The AC field performance of the ECB will be tested using this setup. In addition, the same configuration will then be tested with DC field application for comparison purposes. Later, the empirical results will be used to validate the numerical and analytical models presented in the first two chapters of this

thesis. In addition, the controller designed in Chapter 5 needs to be implemented to improve the braking performance of the ECB.

The experimental work will complete the ECB research; however there are three additional steps that will be taken in order to further investigate the feasibility and the performance of the ECB studied. One of these steps will be to design a prototype that can be mounted on a vehicle and then to carry out road performance of the brake and the controller on the dynamometer. For the tests, it is proposed to use the Quarter Car Shaker (See Figure 7-1) available at the Simon Fraser University in Surrey, BC. This equipment is used to test suspension modules but it will be modified so that an ECB can be mounted on along with the necessary transducers such as encoders, torque sensor, load cells and thermocouples. Also along with the design and prototyping, the power optimization for the ECB brake will be included as well in the proposed study.



Figure 7-1. Quarter vehicle shaker for testing real world performance of ECB (equipment is available at SFU, BC)

The second step will be to have an in-depth understanding of the ECB in terms of the performance of the brake when there are various types of signals applied with varying magnitude and frequency. Note that the Helmholtz equation that was solved is a linear equation and it can be solved using Fourier series. With the use of Fourier series, the results can be obtained as a series sum. This will help us study the performance of the brake under time varying fields in any waveform, not just the ones that have simple mathematical expressions.

The third step will be the last item to be investigated. ECB is a magnetic brake and the kinetic energy is dissipated as heat by means of eddy currents on the conductive disk. In theory, such a brake has the potential to be used as a regenerative brake. These eddy currents generated can be redirected and complete a circuit that charges the battery of the vehicle. Thus, more work needs to be carried out to investigate the regenerative braking capability and methods of harvesting the currents on a rotating disk. This third step itself will also result in further possibilities of researching into design, implementation, control and testing of the possible regenerative system.

Note that in this study, power input to the system is not studied since the main objective is to realize a stand-alone ECB that generates comparable braking torques as CHB. The power can be calculated using the current and voltage applied to the coil of the electromagnet. For the ECB analysis, magnetic flux densities are used as inputs and the electromagnet design that is necessary to generate such flux densities is not investigated. Since the resistance of the coils are significantly low, the voltage and current requirement for the ECB will be low as well (i.e. 42 ohms per km for AWG 21). The requirements depend on the electromagnet design, and coil and core properties, but the estimated requirement for the four-PPA ECB will be between 250 W and 400 W and for 4 brake actuators, it will be between 1 kW and 1.2 kW.

In order to calculate the required power input to the system, an electromagnet that applies fluxes up to 1.5 T is needed. Note that as a part of the design of real vehicle ECB model, the electromagnets will be designed and optimized for the requirements. After the detailed design, the power input to the system can be calculated for the ECB configuration.

7.3 Recommendations

- Use of Fourier series will result in in-depth analytical understanding of the ECB braking torque generation using various types of periodic AC fields,
- Analytical model does not account for any temperature change, thus in order to account for the temperature effect, the simulations can be carried using property values at different temperature values,
- The objective is to design a stand-alone ECB in this study, for complete analysis, not only the braking torque, but the power input, temperature change and weight of the brake need to be included in the analysis,
- In addition to designing for higher braking torque, the economics, safety, reliability, and lifetime need to be considered for the ECB design,
- The focus application is selected to be automotive, however the system can be designed for various applications,
- A more complete adaptive nonlinear predictive controller can be designed for real braking scenarios for a road vehicle,
- Experimental setup can be altered for a multi PPA configuration for validating the optimization results and for increased flux density application; a laminated core needs to be selected for the experimental studies.

Bibliography

- [1] Forensic Engineering Technical Services, Brakes, Portland, OR, 2007. Available: <http://www.e-z.net/ts/>.
- [2] Delphi Co., Delphi Brake Modules - Electric Caliper, Troy, MI, 2005.
- [3] Automotive Systems Division of Continental AG, Continental Electronic Brake Systems, Auburn Hills, MI, 2007.
- [4] E. Richter, C. Ferreira, Performance evaluation of a 250 kW switched reluctance starter generator, Proc. of 30th IEEE Indus. Appl. Soc. Annual Meeting, 1 (1995) 434-440.
- [5] A.G. Jack, B.C. Mecrow, J. Haylock, A comparative study of PM and SR motors for high performance fault tolerant applications, IEEE Transactions on Indus. Appl., 32(4) (1996).
- [6] T.J.E. Miller, Switched reluctance motors and their control, Magna Physics Publishing and Oxford Science Publications, 1993.
- [7] J.D. Carlson, D.F. LeRoy, J.C. Holzheimer, D.R. Prindle, R.H. Marjoram, Controllable brake, US Patent 5.842.547, 1998.
- [8] K. Karakoc, Edward J. Park, Afzal Suleman, Design considerations for an automotive magnetorheological brake, Mechatronics, 18(8) (2008) 434-447.
- [9] R.W. Phillips, Engineering Applications of Fluids with a Variable Yield Stress, Ph.D. Dissertation, University of California, Berkeley, CA (1969).
- [10] S. Genc, P.P. Phule, Rheological properties of magnetorheological fluids, Smart Materials and Structures, 11 (2002) 140-146.
- [11] J. Song, Performance Evaluation of a Hybrid Electric Brake System with a Sliding Mode Controller, Mechatronics, 15 (2005) 339-358.
- [12] S.M. Jang, S.H. Lee, S.S. Jeong, Characteristic analysis of eddy current brake system using the linear Halbach array, IEEE Transactions on Magnetics, 38(5)(2002) 2994-2996.
- [13] P.J. Wang, S.J. Chiueh, Analysis of eddy current brakes for high speed railway, IEEE Transactions on Magnetics, 34(4) (1998) 1237-1239.

- [14] W.M. Saslow, Maxwell's theory of eddy currents in thin conducting sheets and applications to electromagnetic shielding and MAGLEV, *American Journal of Physics*, 60(8) (1992) 693-711.
- [15] S.M. Jang, S.S. Jeong, S.D. Cha, The application of linear Halbach array to eddy current rail brake system, *IEEE Transactions on Magnetism*, 37(4) (2001) 2627–2629.
- [16] S.M. Jang, J. K. Kwon, S. H. Lee, B.S. Kim, H.J. Cho, Characteristic analysis of linear eddy current brakes, *Proc. of 6th International Conference on Electrical Machines and Systems*, 1 (2003) 177-179.
- [17] W.R. Symthe, On eddy currents in a rotating disk, *Transactions on AIEE*, 61 (1942) 681-684.
- [18] D. Schieber, Unipolar induction braking of thin metal sheets, *Proc. Inst. Elec. Eng.*, 119 (1972) 1499–1503.
- [19] D. Schieber, Braking torque on rotating sheet in stationary magnetic field, *Proc. Inst. Elec. Eng.*, 121(1974) 117–122.
- [20] H. D. Wiederick, N. Gauthier, D. A. Campbell, P. Rochon, Magnetic braking: Simple theory and experiment, *Amer. J. Phys.*, 55 (1987) 500–503.
- [21] M. A. Heald, Magnetic braking: Improved theory, *Amer. J. Phys.*, 56 (1988) 521–522.
- [22] J. H. Wouterse, Critical torque and speed of eddy current brake with widely separated soft iron poles, *Inst. Elec. Eng. Proc. B.*, 138(4) (1991) 153–158.
- [23] E. Simeu, D. Georges, Modeling and control of an eddy current brake, *Control Eng. Practice*, 4(1)(1996) 19–26.
- [24] L. Barnes, J. Hardin, C.A. Gross, D. Wasson, An eddy current braking system, *Proc. of SSST: 25th Southeastern Symposium on System Theory*, (1993) 58-62.
- [25] N. Burais, A. Foggia, A. Nicolas, J. Pascal, J. Sabonnadiere, Numerical solution of eddy currents problems including moving conducting parts, *IEEE Transactions on Magnetism*, 20(5)(1984) 1995- 1997.
- [26] W. Peterson, Numerical solution of eddy current problems in ferromagnetic bodies travelling in a transverse magnetic field, *International Journal for Numerical Methods in Engineering*, 58(12) (2003) 1749-1764.

- [27] H.J. Conraths, Eddy current and temperature simulation in thin moving metal strips, *International Journal for Numerical Methods in Engineering*, 39(1)(1998) 141–163.
- [28] K. Lee, K. Park, J.N. Kang, S.M. Wang, Torque analysis and optimization of an eddy current brake system, *Proc. of IMCSD 99*, San Jose, California, USA, (1999) 137-141.
- [29] K. Lee, K. Park, Modeling Eddy currents with boundary conditions by using coulomb's law and the method of images, *IEEE Transaction on Magnetics*, 38(2) (2002) 1333-1340.
- [30] K. Lee, K. Park, Modeling of the eddy currents with the consideration of the induced magnetic flux, *TENCON, Proc. of IEEE International Conference on Electrical and Electronic Technology*, 2(2001) 762–768.
- [31] K. Lee, K. Park, Eddy currents modeling with the consideration of the magnetic Reynolds number, *Proc. of ISIE 2001: IEEE International Symposium on Industrial Electronics*, 1 (2001) 678-683.
- [32] K. Karakoc, E. J. Park, A. Suleman, Improved braking torque generation capacity of an eddy current brake with time varying magnetic fields: A numerical study ,*Finite Elements in Analysis and Design* 59 (2012) 66–75.
- [33] P. P. Yannopoulos-Lascaratos, J. A. Tegopoulos, Eddy-current distribution in cylindrical structures caused by rotating magnetic fields, *IEE Proceedings B Electric Power Applications*, 129(2) (1982): 64.
- [34] U. B. Sathuvalli, Y. Beyazitoglu, The Lorentz Force on an electrically conducting sphere in an alternating magnetic field, *IEEE Transactions on Magnetics*, 32(2) (1996): 386-399.
- [35] N. J. Siakavellas, Two simple models for analytical calculation of eddy currents in thin conducting plates, *IEEE Transactions on Magnetics*, 33(3) (1997):2247-2257.
- [36] G. Lohofer, An electrically conducting sphere in a three-dimensional, alternating magnetic field, *IMA Journal of Applied Mathematics*, 68(1) (2003): 1-21.
- [37] G. Sinha, S. S. Prabhu, Analytical model for estimation of eddy current and power loss in conducting plate and its application, *Physical Review Special Topics – Accelerators and Beams*, 14(6) (2011).

- [38] A. D. Polyanin, Handbook of linear partial differential equations for engineers and scientists, Boca Raton, FL, Chapman & Hall, 2000.
- [39] P. Lorrain, D. R. Corson, Electromagnetic fields and waves, 2nd ed. San Francisco, CA, Freeman, 1970.
- [40] G.R. Liu. A G space theory and a weakened weak (W2) form for a unified formulation of compatible and incompatible methods: Part I theory and Part II applications to solid mechanics problems. International Journal for Numerical Methods in Engineering, 81 (2010) 1093-1126.
- [41] A. Lesobre, A. Ahmedl, and D. Drecq, An analytical dynamic model of eddy-current brakes, Electric Machines and Drives Conference, 2001 IEEE International, (2001): 122-125.
- [42] Isuzu Motors Ltd., Eddy current braking system, US Patent 4,398,111, 1993.
- [43] Magnetar Technologies, Ltd., “Eddy current brake, US Patent 6,659,237 B1, 2003.
- [44] G. Ala, E. Francomano, A. Tortorici, E. Toscano, F. Viola, A smoothed particle interpolation scheme for transient electromagnetic simulation, IEEE Transactions on Magnetics, 42(4) (2006) 647-650.
- [45] H. Nguyen-Xuan, T. Rabczuk, S. Bordas, J. F. Debongnie, A smoothed finite element method for plate analysis, Computer Methods in Applied Mechanics and Engineering, 197 (2008) 1184-1203.
- [46] H. Nguyen-Xuan, G.R. Liu, T. Nguyen-Thoi, C. Nguyen Tran, An edge-based smoothed finite element method (ES-FEM) for analysis of two-dimensional piezoelectric structures, Journal of Smart Material and Structures, 18(6)(2009) 065015.
- [47] H. Nguyen-Xuan, G.R. Liu, C. Thai-Hoang, T. Nguyen-Thoi, An edge-based smoothed finite element method (ES-FEM) with stabilized discrete shear gap technique for analysis of Reissner-Mindlin plates, Computer Methods in Applied Mechanics and Engineering, 199 (9-12) (2010) 471-489.
- [48] T. Hughes, J. Cottrell, Y. Bazilevs, Isogeometric analysis: CAD, finite elements, NURBS, exact geometry and mesh refinement, Comput. Methods Appl. Mech. Engrg. 194 (2005) 4135-4195.

- [49] A. Buffa, G. Sangalli, R. Vazquez, Isogeometric analysis in electromagnetics: B-splines approximation. *Comput. Methods Appl. Mech. Engrg.* 199 (2010) 1143-1152.
- [50] N. Nguyen-Thanh, J. Kiendl, H. Nguyen-Xuan, R. Wüchner, K.U. Bletzinger, Y. Bazilevs, T. Rabczuk, Rotation free isogeometric thin shell analysis using PHT-splines, *Computer Methods in Applied Mechanics and Engineering*, 200(47-48) (2011) 3410-3424.
- [51] K. Parsons, M. Griffin, Whole-body vibration perception thresholds, *Journal of Sound and Vibration*, 121(2), (1988) 237–258.
- [52] M. J. Griffin, *Handbook of human vibration*. Academic Press, (1996). ISBN-10: 0123030412
- [53] M. A. Bellmann, *Perception of whole-body vibrations: from basic experiments to effects of seat and steering-wheel vibrations on the passenger's comfort inside vehicles (Berichte Aus Der Physik)*, Shaker Verlag GmbH, Germany, (2002).
- [54] T.-L. Teng, F.-A. Chang, C.-P. Peng, Analysis of human body response to vibration using multi-body dynamics method, *P I MechEng K-J Mul*, 220(3), (2006) 191–202.
- [55] D. Vangi, A. Virga, Evaluation of emergency braking deceleration for accident reconstruction, *Vehicle System Dynamics: International Journal of Vehicle Mechanics and Mobility*, 45(10), (2007).
- [56] S. J. Qin, T. A. Badgwell, An overview of industrial model predictive control technology, *Fifth International Conference on Chemical Process Control*, AIChE and CACHE, (1997) 232-256.
- [57] S. J. Qin, T. A. Badgwell, An overview of nonlinear model predictive control applications, *Nonlinear Model Predictive Control*, Birkhauser, Verlag, (2000) 369-392.
- [58] D. Q. Mayne, J. B. Rawlings, C. V. Rao, P. O. M. Scokaert, Constrained model predictive control: stability and optimality, *Automatica*, 36 (2000) 789-814.
- [59] C. V. Rao, S. J. Wright, J. B. Rawlings, Application of interior-point methods to model predictive control, *J. Optim Theory Appl.*, 99 (1998) 723-757.

- [60] J. Richalet, A. Rault, J. L. Testud, J. Papon, Model predictive heuristic control: applications to industrial processes, *Automatica*, 14 (1978) 413-428.
- [61] D. M. Prett, R. D. Gillette, Optimization and constrained multi-variable control of a catalytic cracking unit, *Proc. Of Joint Automatic Control Conference*, (1980).
- [62] T. B. Blanco, P. Willems, B. D. Moor, J. Berlamont, Flooding prevention of the demer river using model predictive control, *Proc. of the 17th World Congress The International Federation of Automatic Control*, (2008).
- [63] N. Haverbeke, T. V. Herpe, M. Diehl, G. V. den Berghe, B. D. □Moor, Nonlinear model predictive control with moving horizon state and disturbance estimation - application to the normalization of blood glucose in the critically ill, *Proc. of the 17th World Congress The International Federation of Automatic Control*, (2008).
- [64] L. Coetzee, I. Craig, E. Kerrigan, Nonlinear model predictive control of a run-of-mine ore milling circuit, *Proc. of the 17th World Congress The International Federation of Automatic Control*, (2008).
- [65] B. Guerreiro, C. Silvestre, R. Cunha, Terrain avoidance model predictive control for autonomous rotorcraft, *Proc. of the 17th World Congress The International Federation of Automatic Control*, (2008).
- [66] T. Murao, H. Kawai, M. Fujita, Predictive visual feedback control with eye-in/to-hand configuration via stabilizing receding horizon approach, *Proc. of the 17th World Congress The International Federation of Automatic Control*, (2008).
- [67] T. T. Nguyen, K. A. Kyoung, A hysteresis functional link artificial neural network for identification and model predictive control of SMA actuator, *Journal of Process Control*, 22(4) (2012) 766-777.
- [68] T. Gillespie, *Fundamentals of vehicle dynamics*, SAE, Warrendale, PA, 1992.
- [69] J. Kennedy, R. Eberhart, Particle swarm optimization, in *Proc. of the IEEE Int. Conf. on Neural Networks*, Piscataway, NJ, (1995) 1942–1948.
- [70] S. P. Thompson, *The electromagnet and electromagnetic mechanism*, Cambridge University Press, 2011.
- [71] A. N. Mansfield, *Electromagnets – their design and construction*, Rough Draft Printing, 2007.

- [72] ASTM International, Annual Book of ASTM Standards, 4(3), Magnetic Properties, 2005.
- [73] K. Karakoc, Design optimization of a magnetorheological brake system based on magnetic circuit design, MAsc Dissertation, University of Victoria, BC, 2007.
- [74] Magnetics, Inc., online: <http://www.mag-inc.com>, July 2012.
- [75] D. Cole, Elementary vehicle dynamics, Course Notes in the Mechanical Engineering, The University of Michigan, Ann Arbor, MI, 1972.
- [76] C. Lee, K. Hedrick, K. Yi, Real-Time slip-based estimation of maximum tire-road friction coefficient, Mechatronics, IEEE/ASME Transactions on, 9(2), June 2004.
- [77] E.J. Park, D. Stoikov, L. Falcao da Luz, A. Suleman, A performance evaluation of an automotive magnetorheological brake design with a sliding mode controller, Mechatronics, 16(2006) 405-416.
- [78] A. B. Will, S. Hui, S. Zak, Sliding mode wheel slip controller for an antilock braking system, Int. J. of Vehicle Design, 19(4) (1998) 523-539.

Appendix

Appendix A. Vehicle dynamics

Here, the vehicle dynamics are studied in order to calculate the required amount of braking torque in order to stop a vehicle. Then, in the following section (Appendix B) required braking torque for several vehicles were calculated using the dynamic vehicle model.

The motion of a vehicle is described using the quarter vehicle model [68]. This model allows us to model the vehicle in order to calculate the required braking torque that a brake should provide. The basic assumption of this model is that the mass of the vehicle is divided equally between four wheels. This is not the exact case. Front wheels carry much weight than the rear wheels. Usually 0.55:0.45 of the total mass is carried by the front wheels and rear wheels respectively.

As a result of the assumption, the dynamic model of a wheel is enough to determine the braking torque required to stop the rotation of the wheels. In Figure A-1, free body diagram of a wheel is shown:

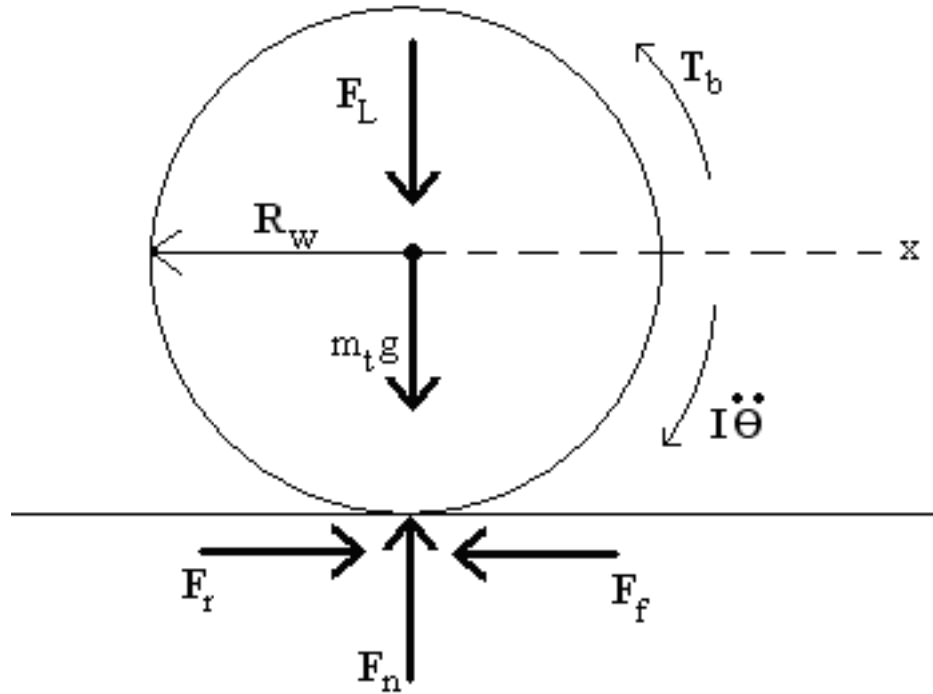


Figure A-1. Free body diagram of a wheel

During braking, a torque is applied by the brake, T_b , and due to the deceleration of the vehicle, there would be an additional torque occurs on the wheel, $I\ddot{\theta}$, where I is the moment of inertia and $\ddot{\theta}$ is the angular acceleration. The radius of the wheel is R_w , x is the distance traveled by the vehicle and F_r , F_f , F_n , and F_L are the rolling resistance force, the friction force, normal force and the transfer of weight caused by braking of the vehicle.

According to the quarter vehicle model, the mass that the wheel carries can be calculated as:

$$m_t = \frac{1}{4} m_v + m_w \quad (\text{A.1})$$

where m_v is the total mass of the vehicle and m_w is the mass of the wheel. After defining the mass on the wheel, the effective mass moment of inertia must be defined as:

$$I = I_w + \frac{1}{2} \tau^2 I_e + I_y \quad (\text{A.2})$$

where I is the total mass moment of inertia, I_w is the wheel's inertia, I_e is the engine inertial, τ is the gear ratio and I_y is the inertia of the brake disks. The inertia of the engine and the gear ratios must be considered together with a ratio of 0.5 in the effective mass moment of inertia. This 0.5 factor is added into the equation because of the distribution of the inertia of the engine to each of the driving wheels.

The rolling resistance force against the motion of the wheel is defined in [68] as:

$$F_r = f_0 + 3.24 f_s (K_v \dot{x})^{2.5} \quad (\text{A.3})$$

where K_v is a conversion factor that is used for converting the speed value from m/s to mph, f_s and f_0 are basic coefficient and the speed effect coefficient. This equation was developed by The Institute of Tech. in Stuttgart for rolling on a concrete surface [75].

The friction force acting on the wheel is defined in terms of the normal force and the friction coefficient between the tire and the surface.

$$F_f = \mu_f F_n \quad (\text{A.4})$$

$$F_n = m_t g - \frac{m_v h_{cg}}{l_{base}} \ddot{x} = m_t g - F_L \quad (\text{A.5})$$

where l_{base} is the wheel base and h_{cg} is the height of the center of gravity and the friction coefficient, μ_f , is a function of the slip ratio, s_r , which is the relative proportion of the rolling to slipping, i.e.

$$s_r = \frac{\dot{x} - R_w \dot{\theta}}{\dot{x}} \quad (\text{A.6})$$

where $\dot{\theta}$ is the angular velocity of the wheel.

The correlation between the slip ratio and the coefficient of friction is illustrated in Figure A-2. The relation is also shown for several types of surfaces.

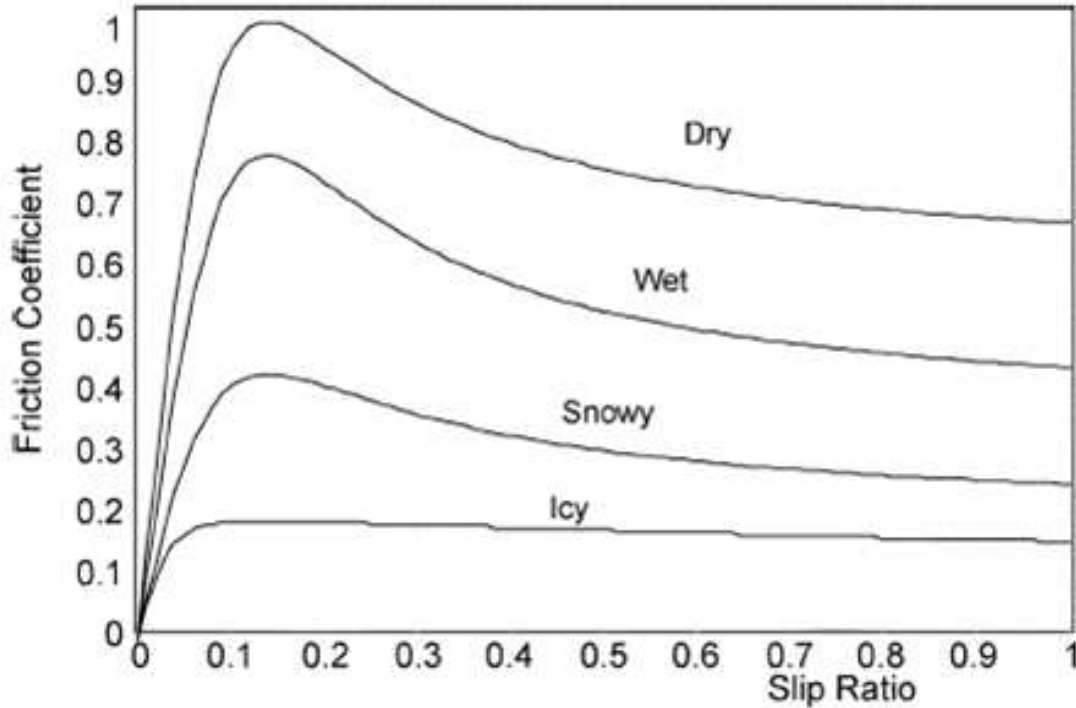


Figure A-2. Friction coefficient versus slip ratio for several surfaces [76]

After defining all the forces that are shown in the free body diagram, the Newtonian equations of motion for the wheel can be written as:

$$m_t \ddot{x} = -F_f = -\mu_f m_t g + \mu_f \frac{m_v h_{cg}}{l_{base}} \ddot{x} \quad (A.7)$$

$$I \ddot{\theta} = -T_b + R_w F_f - R_w F_r = -T_b + \mu_f R_w F_n - R_w F_r \quad (A.8)$$

The first equation is the force equilibrium in the direction of motion and the second equation is the moment equilibrium around the axis that is perpendicular to the wheel surface. These two equations are the governing equations of this type of motion. And the required braking torque, which stops the car, can be found by using these two equations.

Appendix B. Braking torque requirements

Here in this section, required braking torque values for various vehicles were calculated using the dynamic model introduced previously in Appendix A. However, in order to calculate the braking torque, there are several properties that have to be known. As in [77], these parameters for a loaded car were taken from the previous works of Will AB, Hui S and Zak Sh [78] and are listed in Table A-1;

Table A-1. Parameters for the quarter vehicle model

Wheel Radius	R_w	0.326 m
Wheel Base	l_{base}	2.5 m
Center of Gravity Height	h_{cg}	0.5 m
Wheel Mass	m_w	40 kg
1/4 of the Vehicle Mass	$m_v/4$	415 kg
Total Moment of Inertia of wheel and engine	I_t	1.75 kg.m ²
Basic Coefficient	f_o	10e-2
Speed Effect Coefficient	f_s	0.005
Scaling Constant	K_v	2.237

The required braking torque values for a sport motorbike and a scooter were also calculated, however since the lack of detailed properties (i.e. f_o , f_s , and K_v), the braking torque requirement for these vehicles were calculated assuming that the whole kinetic energy of the vehicle is dissipated in the brake actuators. With such an assumption, the effects of rolling friction and the friction between the tire and the road were omitted. In Table A-2, the assumptions made for the calculations and the data used in the calculations are shown.

Table A-2. Required braking torque values for several vehicles

Properties	Passenger Vehicle	Sport Motorbike	Scooter
Mass (Total-loaded) (kg)	1820 ($m_w = 40$)	370	250
Wheel Size (inch)	13	17	12
Wheel Radius (m)	0.3226	0.305	0.237
Number of Brake Actuators	4	2	2
Assumptions:			
Road Surface	Dry, smooth concrete		
Initial Speed	60 mph (26.82 m/s)		
Deceleration (m/s^2)	5.8 m/s^2		
Braking Torque (Nm)	560	321	171

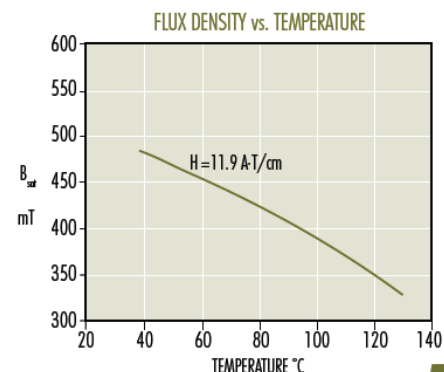
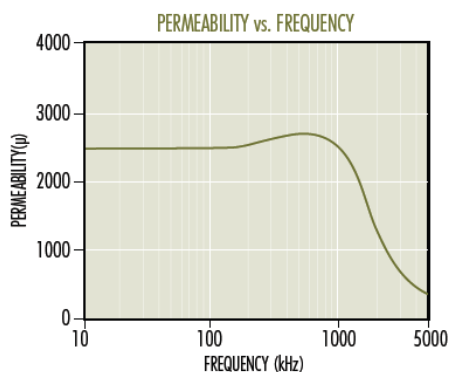
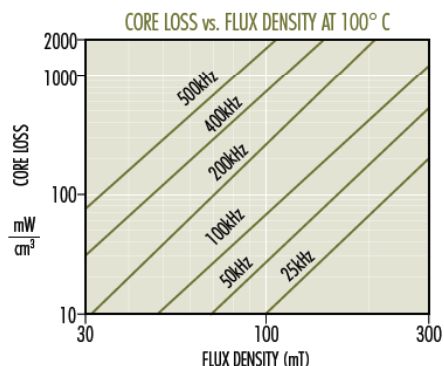
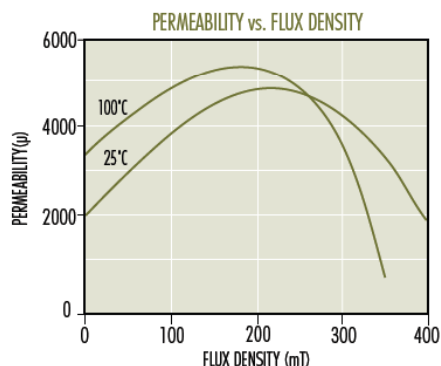
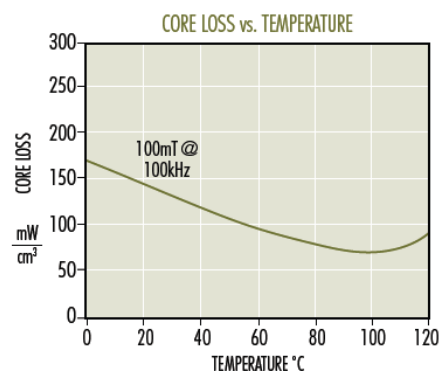
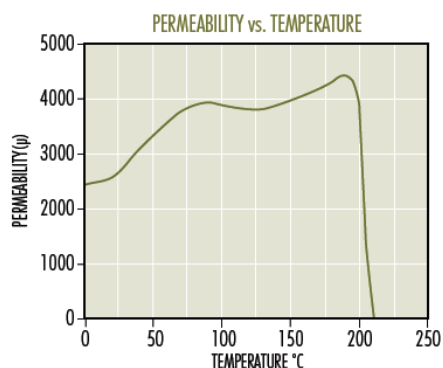
This study was made in order relate the requirements with the capacity of an EMB. Table A-2 gives an idea about how much braking torque must be generated by an ECB. Therefore in terms of the feasibility of such a brake system, the main goal must be to generate braking torques as much as the requirements.

Appendix C. Ferrite material properties and core specs for AC field experiments [74]

P Material

A low-medium frequency general-purpose power converter material. Engineered for lowest losses at 95°C. Available in almost all core sizes and shapes.

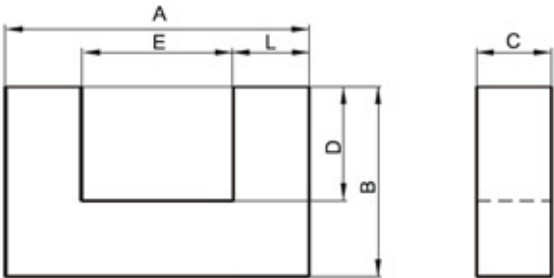
Initial Perm (10kHz) $2,500 \pm 25\%$
 Saturation Flux Density (4,700 G at 15 Oe, 25°C) 470 mT, 11.9 A-T/cm
 Curie Temperature 210°C



Specification for:

0P49920UC

DIMENSIONS



(mm)	Nominal:	Tol. min.:	Tol. max.:
A	126.0	-4.0	+ 4.0
B	91.0	-1.0	+ 1.0
C	20.0	-0.6	+ 0.6
D	63.0	-2.0	+ 2.0
E	70.0	-2.0	+ 2.0
L	28.0 Ref.		
Eff. Parameters			
Ae mm ²	Amin mm ²	le mm	Ve mm ³
560.0	560.0	480.0	268800

INDUCTANCE

AL value (nH)	Test conditions
Nom: 3572 Min.: 2679	10 kHz, < 0.5 mT, 25 °C

MARKING

0P49920UC PXXXXX

CORE LOSSES

P _i max	Test conditions
201 mW/cm ³ (54 W/set)	100 kHz, 100 mT, 100 °C